



저작자표시-비영리-변경금지 2.0 대한민국

이용자는 아래의 조건을 따르는 경우에 한하여 자유롭게

- 이 저작물을 복제, 배포, 전송, 전시, 공연 및 방송할 수 있습니다.

다음과 같은 조건을 따라야 합니다:



저작자표시. 귀하는 원저작자를 표시하여야 합니다.



비영리. 귀하는 이 저작물을 영리 목적으로 이용할 수 없습니다.



변경금지. 귀하는 이 저작물을 개작, 변형 또는 가공할 수 없습니다.

- 귀하는, 이 저작물의 재이용이나 배포의 경우, 이 저작물에 적용된 이용허락조건을 명확하게 나타내어야 합니다.
- 저작권자로부터 별도의 허가를 받으면 이러한 조건들은 적용되지 않습니다.

저작권법에 따른 이용자의 권리는 위의 내용에 의하여 영향을 받지 않습니다.

이것은 [이용허락규약\(Legal Code\)](#)을 이해하기 쉽게 요약한 것입니다.

[Disclaimer](#)

석 . 박사 학위논문 등표지

	<p style="text-align: center;"><b>Graphene Flakes and Graphene Composites: Synthesis, Processing and Employment for Printed Electronics Devices</b></p> <p style="text-align: right;"><b>Adnan Ali</b>      <b>2014</b></p>
--	---

**A THESIS  
FOR THE DEGREE OF DOCTOR OF PHILOSOPHY**

**Graphene Flakes and Graphene Composites: Synthesis,  
Processing and Employment for Printed Electronics  
Devices**

**Adnan Ali**

Department of Mechatronics Engineering  
GRADUATE SCHOOL

JEJU NATIONAL UNIVERSITY

2014. 02

# Graphene Flakes and Graphene Composites: Synthesis, Processing and Employment for Printed Electronics Devices

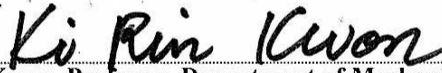
Adnan Ali

(Supervised by Professor Kyung Hyun Choi)

A thesis submitted in partial fulfillment of the requirement for  
the degree of Doctor of Philosophy

2014. 02

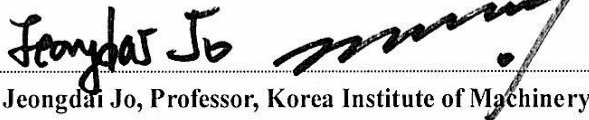
The thesis has been examined and approved.



Thesis Director, Ki Rin Kwon, Professor, Department of Mechanical Engineering



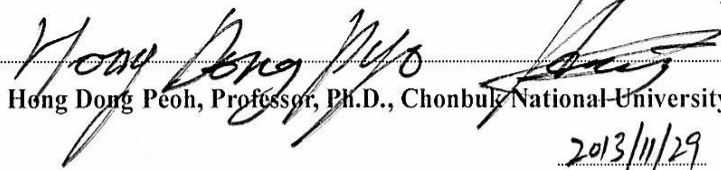
Yang-Hoi Doh, Professor, Department of Electronic Engineering



Jeongda Jo, Professor, Korea Institute of Machinery and Materials



Kyung-Hyun Choi, Professor, Department of Mechatronics Engineering



Hong Dong Peoh, Professor, Ph.D., Chonbuk National University

2013/11/29

Date

Department of Mechatronics Engineering  
GRADUATE SCHOOL  
JEJU NATIONAL UNIVERSITY

## Acknowledgements

Start with the name of Almighty Allah, the most merciful, the most beneficent. First of all I would present my humble gratitude in front of Allah Who enabled me to accomplish the dignified cause of education and learning and I would pray to Him that He would make me able to utilize my knowledge and edification for the betterment of humanity and its development. At this vital occasion when I am going to get the highest educational degree, I acknowledge and salute the vision of my grandfather and support of my father and other family members. The prayers of my mother and her confidence in me have always been a source of courage during the course of my entire life.

I am heartily thankful to my supervisor, Prof. Kyung Hyun Choi, whose encouragement, guidance and support from the initial to the final level enabled me to surpass all the obstacles in the completion of this research work. He encouraged me to not only grow as an experimentalist but also as an instructor and an independent thinker. The way he identified the best in me and made me to use it during these five years (since my MS, 2008) speaks of itself of his man management skills, his persona and his thorough professionalism. His thought-provoking seminars and discussions and a never-ending appetite for excellence I will admire and cherish forever. His encouragement and guidance during my high time and support and kindness during the down times have all been a source of motivation towards learning more and more.

I am also thankful to Prof. Ki Rin Kwon, Prof. Yang Hoi Doh, Professor Jeongdai Jo and Professor Hong Dong Peoh for being my thesis advisors. Their help and support in my thesis completion is highly appreciative. I would also like to thank Prof. Gyoujin Cho, and Prof. Hyun Myung Taek for their extreme support.

During my stay I had many mentors who helped a lot in making me more organized, disciplined and efficient. Dr. Maria, Dr. Nauman, Dr. Navaneethan, Dr. Naeem, Dr. Khalid, Dr. Anil Kumar and Dr. Rongli Wang are a few of those whose friendship, help and support I would always admire. Friends are a blessing and I couldn't imagine spending long years in Jeju without friendly company. I am especially thankful to Kamran and Zubair for his sustenance and respect they have given to me. I would also like to mention about my other

lab friends Shahid Aziz, Junaid, Ali Shawkat, Ghayas and Syed Murtaza Mehdi, who has played their role in making me. Rashid Ahmad, Safdar Ali, Sohail, Hyun-Woo, Sodhi, Ganesh, Farrukh, Jeong-beom, Hyung Chan, Go-beom, Karthik, Anand, Sarwan are a few names whose support were always there for me. I am thankful to Jae Hee Park, Jo Hanna and Ji-yeon for their always helping presence around me. I am also thankful to my Chinese friends Dr. Jin Long Park, Lu Zhang, Lu Shanshan, Erxu, Jaibei and Chen Soo for their kind support and encouragement. I would like to mention here about my Vietnamese friends Ngoc Thuy Bui, Viet Vam Vo, Thai Doan Luong and Thao Tran whose company made my stay more nice and joyful here. Also, I would like to mention my very best friend Irfan Ud Din who always remains supportive and helping me all the time.

I am deeply indebted my elder brothers Shahenshah Gauhar, Ali Askar and Moazzam Ali who have always encouraged me and remained a source of guidance throughout my academic life and always kept me away from family burdens. I would also like to thank my uncles who encouraged me throughout my studies and provided me the necessary moral support. I would like to pay my heartiest gratitude to little ones of my family Umama Gul, Gul-e-lala, Maaz Ali Khan, Ali Sher Khan, Ali Afzal Khan and Nangyal Ali Khan. I would also like to pay my heartiest gratitude to my both sister in laws who took care of me.

# Table of Contents

<b>1</b>	<b>Introduction</b>	<b>1</b>
1.1	Graphene	1
1.2	Electrohydrodynamic Atomization (EHDA) Deposition and its Applications	3
1.3	Motivation and Introduction of this Thesis	5
<b>2.</b>	<b>Background and Literature Survey</b>	<b>7</b>
2.1	Graphene	7
2.1.1	Crystal Structure	8
2.1.2	Morphology and Structure	8
2.2.	Graphene Properties	9
2.2.1	Optical Properties	9
2.2.2	Raman Spectroscopy of Graphene	10
2.2.3	Thermal Properties	12
2.2.4	Mechanical properties	12
2.2.5	Electrical Properties of Graphene	13
2.3	Synthesis Methods of Graphene and Resulting Material Properties	14
2.3.1	Mechanical Exfoliation	14
2.3.2	Chemical Exfoliation	15
2.3.3	Some Other Novel Routes of Graphene Synthesis	16
2.3.4	Chemical Synthesis: Graphene from Reduced Graphene Oxide	16
2.3.5	Electrochemical Synthesis	17
2.3.6	Direct Chemical Synthesis: Pyrolysis of Sodium Ethoxide	19
2.3.7	Unzipping of Nanotubes	19
2.3.8	Thermal Chemical Vapor Deposition Process	20
2.3.9	Thermal Chemical Vapor Deposition	21
2.3.10	Plasma-Enhanced Chemical Vapor Deposition	23
2.3.11	Epitaxial Growth of Graphene on SiC Surface	24
2.4	Graphene Growth Mechanisms	25
2.5	Large-Area Production of Graphene Thin Films and Transfer Methods	25
2.5.1	Large-Area Graphene Synthesis	26
2.5.2	Transfer Mechanisms	27
2.5.3	Large-Area Graphene Transfer Methods	29
<b>3.</b>	<b>Electrohydrodynamic Atomization (EHDA) Deposition Technique</b>	<b>32</b>
3.1	Electrohydrodynamic Atomization Modes	32
3.1.1	Dripping mode	33
3.1.2	Micro-dripping mode	33
3.1.3	Spindle mode	34
3.1.4	Unstable cone-jet mode	34
3.1.5	Cone-jet mode	34
3.1.6	Multi-jet mode	35
3.2	Parameters Affecting the Cone-jet	36
3.2.1	Flow-rate	36
3.2.2	Electric field (Applied voltage)	37
3.2.3	Nozzle diameter	37
3.2.4	Conductivity	38
3.2.5	Surface Tension	38

3.2.6	Viscosity .....	38
3.3	ESD Experimental Setup .....	38
3.3.1	Metallic nozzle (Harvard Apparatus) .....	38
3.3.2	Syringe Pump (Harvard Apparatus, PHD 2000 Infusion).....	39
3.3.3	Power Source (NanoNC).....	39
3.3.4	Camera (MotionPro X).....	39
3.3.5	Miscellaneous Equipment .....	40
<b>4.</b>	<b>Deposition of Graphene flakes and its composites by using EHDA Technique .....</b>	<b>41</b>
4.1	Graphene Flakes Deposition .....	41
4.1.1	Synthesis of Graphene Dispersion .....	42
4.1.2	Graphene Flakes Film Deposition.....	42
4.1.3	Taylor cone and Atomization modes .....	43
4.1.4	Optical Microscopy .....	44
4.1.5	SEM Analysis .....	45
4.1.6	3D Nanomap .....	45
4.1.7	X-ray Diffraction Analysis .....	46
4.1.8	Raman Spectra Analysis.....	47
4.1.9	UV/Vis/NIR Analysis .....	48
4.1.10	Electrical Behavior Analysis .....	49
4.2	Graphene/Zinc Oxide Composite Deposition .....	51
4.2.1	Decoration of Graphene Flakes with Zinc Oxide nanoparticles .....	52
4.2.2	Experiment for Graphene Flakes film Decoration with ZnO.....	52
4.2.3	Morphological Analysis .....	54
4.2.4	Structural Analysis .....	55
4.2.5	3D Nano-mapping for Surface roughness.....	56
4.2.6	Raman Spectroscopy Analysis .....	56
4.2.7	Optical Properties .....	57
4.2.8	Electrical Behavior .....	58
4.3	Direct Fabrication of Graphene/Zinc Oxide Composite Film.....	61
4.3.1	Materials and Synthesis of Dispersion .....	61
4.3.2	Experiment for Deposition of Composite Thin Film .....	61
4.3.3	Morphological Analysis .....	63
4.3.4	3D Nanomapping for surface roughness .....	64
4.3.5	Raman Spectra of Graphene/ZnO .....	64
4.3.6	Optical Properties .....	65
4.3.7	Electrical Behavior .....	66
4.4	Direct Deposition of Graphene/ZnO Composite Film by Semi-blended Approach.....	68
4.4.1	Graphene Flakes and ZnO Deposition from dispersion .....	68
4.4.2	Morphological Analysis .....	68
4.4.3	Raman spectra .....	69
4.4.4	Optical Analysis .....	70
4.4.5	Electrical Analysis.....	71
4.5	Fabrication of Dielectric Poly (4-Vinylphenol) Thin Film .....	73
4.5.1	PVP Ink Synthesis .....	73
4.5.2	Film Fabrication .....	74
4.5.3	Results and Discussions .....	74
4.6	Different Approaches to Fabricate PVP/Graphene composite film using Electrohydrodynamic Atomization Technique .....	79



4.6.1	Graphene/PVP Ink Synthesis for Blended fabrication Approach .....	79
4.6.2	Film Fabrication .....	79
4.6.3	Characterizations and Discussion.....	80
<b>5.</b>	<b>Conclusion and Future Outlook .....</b>	<b>84</b>
5.1.	Conclusions .....	84
5.2.	Future Look .....	85

## List of Figures

Figure 1-1. Graphene Applications in different fields .....	2
Figure 1-2. Body-force diagram of the Taylor-cone. ....	4
Figure 2-1. Depictions of graphene, graphite, carbon nanotubes and buckyballs .....	7
Figure 2-2. (a) Triangular sublattices of graphene, each atom in sublattice “A” have 3 nearest neighbors in sublattice “B” and vice versa and (b) First Brillion Zone of graphene reciprocal lattice.....	8
Figure 2-3. (a) Photograph of a 50- $\mu$ m aperture partially covered by graphene and its bilayer. The line scan profile shows the intensity of transmitted white light along the yellow line. Inset shows the sample design: a 20- $\mu$ m thick metal support structure has apertures 20, 30, and 50 $\mu$ m in diameter with graphene flakes deposited over them; (b) Optical image of graphene flakes with one, two, three, and four layers on a 285-nm thick SiO <sub>2</sub> -on-Si substrate. ....	10
Figure 2-4. (a) Comparison of Raman spectra at 514 nm for bulk graphite and graphene. They are scaled to have similar height of the 2D peak at 2700 cm <sup>-1</sup> ; (b) Evolution of the spectra at 514 nm with the number of layers; (c) Evolution of the Raman spectra at 633 nm with the number of layers. ....	11
Figure 2-5. Fermi surface showing Dirac Cones and the zero-gap nature of graphene.....	13
Figure 2-6. Schematic Representation of the different graphene synthesis methods .....	14
Figure 2-7. (a) and (b): Scanning electron micrographs of mechanically exfoliated thin graphite layers from highly oriented pyrolytic graphite (HOPG) by AFM tip. ....	15
Figure 2-8. (a) Schematic illustrating the chemical exfoliation process, (b) transmission electron micrograph (TEM) of chemically exfoliated graphitic nanosheet, (c) SEM picture of thin graphite nanosheets after the exfoliation process, showing approximately a 10-nm thickness of ~30 layers of single graphite sheet .....	15
Figure 2-9. The process flow chart of graphene synthesis derived from graphite oxide.....	16
Figure 2-10. Mechanism proposed by Stankovich et al. on isocyanate-treated GO where organic isocyanates react with the hydroxyl (left oval) and carboxyl groups (right oval) of graphene oxide sheets to form carbamate and amide functionalities, respectively. (b) Representative FT-IR spectra of GO and phenyl isocyanate-functionalized GO. ....	17
Figure 2-11. Left: experimental schematics; middle: exfoliation of chemically modified	

graphene sheets from the graphite anode; right: TEM image of resulting graphene material with width of 500 nm, length 700 nm and thickness of ~1,1 nm). .....	18
Figure 2-12. Left: Experimental setup for electrochemical production of graphene. Right: The product obtained after filtration of the electrolyte solution. ....	18
Figure 2-13. A process flow chart of graphene nanoribbon fabrication from a carbon nanotubes by the plasma etching process. ....	20
Figure 2-14. Schematic of (a) thermal CVD and (b) plasma-enhanced CVD (PECVD). .....	21
Figure 2-15. Scanning electron micrograph of graphene syntheses on Ni (111) by the DC discharge method. ....	22
Figure 2-16. (a) HRTEM of graphene precipitated on Ni, (b) Raman spectra confirming the effect of cooling rate on graphene formation, and (c) schematic representing the mechanism of carbon segregation on Ni. ....	22
Figure 2-17. (a) Large-scale CVD of graphene on Cu foil; and (b) HRTEM images demonstrating the growth of single-layer, two-layer, and three-layer graphene on Cu. ....	23
Figure 2-18. Schematic illustration of the CVD graphene formation mechanism on a direct dielectric substrate. ....	23
Figure 2-19. Solubility curve of C in Ni. ....	25
Figure 2-20. Graphene film synthesized on a nickel catalyst layer using the CVD method. (a) SEM image of graphene film grown on nickel layer. (b) Thickness and interlayer distance of graphene film estimated by HRTEM. (c) Optical microscope image of transferred graphene film on SiO <sub>2</sub> 300-nm layer. (d) Confocal scanning Raman image corresponding to (c). (e) Raman spectroscopy of each point indicating different number of layers. ....	27
Figure 2-21. (See color insert.) Graphene film synthesized on a copper catalyst layer using the CVD method. (a) SEM image of graphene film grown on copper foil. (b) Morphological image of graphene film flowing copper surface conditions (inset denotes the monolayer and bilayer graphene estimated by TEM). (c) Optical microscope image of the graphene film transferred on SiO <sub>2</sub> layer showing different color indicating different number of layers. (d) Raman spectroscopy for each number of graphene layers on SiO <sub>2</sub> 300-nm layer. ....	28
Figure 2-22. Schematic illustration of large-area graphene transfer process. Transfer process of both neat graphene film and patterned graphene film onto target substrate in a wafer scale through dry transfer printing with a polymer support layer. ....	29
Figure 2-23. (a) Processes for transfer of graphene films. The two insets on the right are the optical micrographs of graphene transferred on SiO <sub>2</sub> /Si wafers (285-nm-thick SiO <sub>2</sub> layer)	

with “bad” (top) and “good” (bottom) transfer, respectively (b) Schematic illustration of the steps for transferring graphene grown on a SiC wafer to another substrate (SiO <sub>2</sub> /Si in this case).	30
Figure 2-24. Schematic illustration of large-area graphene transfer process. Roll-to-roll transfer of graphene grown on copper foil with thermal release tape.	31
Figure 3-1. Real time photograph of the spray, emanating from the nozzle. A wide spray stream is clearly visible at the tip of the nozzle.	36
Figure 3-2. Effect of flow rate on the cone-jet transition. The jet diameter increases with increase in flow-rate. The red arrow indicates the jet break-up point.	37
Figure 3-3. Effect of the applied voltage on shape of the cone-jet at constant flow rate (200µl/hr).	37
Figure 3-4. Schematic diagram of the system deposition system.	39
Figure 3-5. Real-time photograph of the deposition system.	40
Figure 4-1. Schematic diagram of the experimental setup.	43
Figure 4-2. Electrohydrodynamic modes of graphene ink observed during the deposition process, a) Stable meniscus b) dripping, c) micro-dripping, d) pulsating unstable cone-jet, e) stable cone-jet, f) Multi-jet.	43
Figure 4-3. Operating envelop for different EHDA zones. The stable cone jet region is shaded to emphasize upon the possible flow rate and voltage combinations for optimized atomization conditions (stand-off= 10mm).	44
Figure 4-4. Optical Microscopic images of the deposited graphene flakes film (Scale bar is 50 µm).	45
Figure 4-5. (a-c) Low magnification SEM surface view of the deposited films of graphene using deposition speed 5 mm/sec. (d-e) High magnification SEM micrographs showing surface characteristics and very high magnification showing grain size.	45
Figure 4-6. (a) 3D surface profile, (b) 2D surface profile and (c) X- profile of the graphene film deposited on Si substrate.	46
Figure 4-7. Schematic depiction of the graphene fragments in dispersed form and after deposition on substrate.	46
Figure 4-8. XRD patterns of the Graphene flakes film.	47
Figure 4-9. Raman spectra of the deposited graphene flakes film.	47
Figure 4-10. (a) UV-vis spectrum of the graphene flakes film (b) $(ahv)^2$ vs. $hv$ plot for bandgap estimation of graphene flakes film.	48

Figure 4-11. I-V characteristics of ITO/PEDOT-PSS/F8BT/Graphene diode .....	49
Figure 4-12. logI - logV characteristics of ITO/PEDOT-PSS/F8BT/Graphene .....	50
Figure 4-13. Schematic diagram of the system used for the experiment.....	53
Figure 4-14. Electrohydrodynamic Atomization modes of graphene dispersion observed during the deposition process. a) Meniscus, b) dripping mode, c) micro-dripping, d) unstable cone-jet mode, e) stable cone-jet mode and f) multi-jet mode. ....	53
Figure 4-15. Operating envelop representation for different electrospray modes for graphene dispersion. The stable cone jet region is shaded to emphasize upon the possible flow-rate and voltage combination for optimized atomization conditions.....	54
Figure 4.16. Low magnification FE-SEM surface view of the deposited films of Graphene/ZnO using deposition speed 3 mm/sec and 6mm/sec for graphene dispersion and ZnO dispersion, respectively. High magnification SEM micrographs showing graphene decorated with ZnO nano-particles and its agglomeration. ....	55
Figure 4.17. X-ray diffraction pattern of Graphene/ZnO film.....	55
Figure 4-18. (a) 3D surface profile, (b) 2D surface profile and (c) X- profile of the graphene film decorated with ZnO, deposited on Si substrate. ....	56
Figure 4-19. Laser Raman spectrum of graphene/ZnO composite.....	57
Figure 4-20. (a) & (b) Representing absorption and transmittance spectra of graphene/ZnO, respectively. ....	58
Figure 4-21. J-V characteristics of ITO/PEDOT-PSS/F8BT/(Graphene/ZnO) diode. ....	59
Figure 4-22. Double logarithmic current voltage characteristics (log I-log V) of ITO/PEDOT: PSS/F8BT/ (Graphene/ZnO) diode.....	60
Figure 4-23. Schematic depiction of EHDA experimental setup.....	62
Figure 4-24. Electrohydrodynamic modes of Graphene/ZnO ink observed during the deposition process, a) Stable meniscus b) dripping, c) micro-dripping, d) pulsating unstable cone-jet, e) stable cone-jet, f) Multi-jet. ....	62
Figure 4-25. Operating envelop representation for different electrospray regimes. The stable cone jet region is shaded to emphasize upon the possible flow rate and voltage combinations for optimized atomization conditions (stand-off $\approx$ 15mm).....	63
Figure 4-26. (a-d) Low magnification FE-SEM surface view of the deposited films of Graphene/ZnO using deposition speed 3 mm/sec. High magnification SEM micrographs showing ZnO nano-particles and its agglomeration on graphene flakes. ....	63
Figure 4-27. (a) 2D surface profile, (b) X- direction profile and (c) 3D surface profile of the	

graphene/ZnO film deposited on Si substrate.....	64
Figure 4-28. Laser Raman spectrum of graphene/ZnO film.....	65
Figure 4-29. (a) UV-vis spectrum of graphene/ZnO (b) $(\alpha h\nu)^2$ vs. $h\nu$ plot for bandgap estimation of graphene/ZnO film.....	65
Figure 4-30. I-V characteristics of ITO/PEDOT-PSS/F8BT/(Graphene-ZnO) diode device. .	66
Figure 4-31. logI - logV characteristics of ITO/PEDOT-PSS/F8BT/(Graphene-ZnO) diode device. ....	67
Figure 4-32. Schematic diagram of EHDA experimental setup .....	68
Figure 4-33. Low magnification FE-SEM surface view of the deposited films of Graphene/ZnO using deposition speed 3 mm/sec and 6mm/sec for graphene dispersion and ZnO dispersion, respectively. High magnification SEM micrographs showing graphene decorated with ZnO nano-particles and its agglomeration. ....	69
Figure 4-34. Laser Raman spectrum of graphene/ZnO composite. ....	70
Figure 4-35. (a) Transmittance spectra of graphene/ZnO film (b) $(\alpha h\nu)^2$ vs. $h\nu$ plot for bandgap estimation of graphene/ZnO film. ....	71
Figure 4-36. I-V characteristics of ITO/PEDOT-PSS/F8BT/(Graphene/ZnO) diode.....	72
Figure 4-37. logI - logV characteristics of ITO/PEDOT-PSS/F8BT/(Graphene/ZnO). ....	72
Figure 4-38. Schematic diagram of the experimental setup. ....	74
Figure 4-39. Modes of electrostatic atomization of PVP ink: dripping, microdripping, pulsating unstable cone jet, stable cone jet and multi-jet.....	75
Figure 4-40. Operating envelope of PVP ink.....	75
Figure 4-41. (a) – (e) SEM surface morphology of a PVP dielectric thin film from low to high magnification. ....	76
Figure 4-42. XPS analysis representation of a deposited PVP layer. C and O peaks are marked. ....	77
Figure 4-43. UV-vis spectra of PVP thin films showing the transmittance. ....	77
Figure 4-44. I-V curve for a PVP thin film.....	78
Figure 4-45. Graphene/PVP ink operating envelop .....	80
Figure 4-46.(a-d low to high magnification) shows the FE-SEM images of graphene/PVP composite thin film .....	80
Figure 4-47. 3D-Nano Mapping of Graphene/PVP composite film .....	81
Figure 4-48. (a) Transmittance spectra of graphene/PVP film (b) $(\alpha h\nu)^2$ vs. $h\nu$ plot for bandgap estimation of graphene/PVP film. ....	81

Figure 4-49. Capacitance–voltage analysis of capacitor at 1 kHz when dielectric thin film is (a) PVP, (b) Graphene/PVP (Blended Approach) and (c) Graphene/PVP (LBL approach), respectively. ....82

Figure 4-50. Capacitance–voltage analysis of capacitor at higher frequencies when dielectric thin film is (a) PVP, (b) Graphene/PVP (Blended Approach) and (c) Graphene/PVP (LBL approach), respectively. ....83

Figure 5-1. 2D Crystals Based Heterostructures.....85

## List of Tables

Table 4-1. PVP Ink Properties.....	74
------------------------------------	----



## ABSTRACT

There has been a significant stimulation in graphene research since the famous discovery in 2004 by isolating a monolayer of graphene with the help of scotch tape. Graphene, just a single layer of carbon atoms, is progressively making inroads into a wide range of applications, from ballistic electronics to biosensors to flexible/transparent displays. Graphene is a unique material that is strong, light, transparent, and an excellent conductor of heat and electricity. On the other hand, zinc oxide (ZnO) is a wide band semiconductor that demonstrates excellent electrical, optical, catalytic and sensing properties and has numerous applications in various fields. ZnO is a natural n-type semiconductor due to the presence of intrinsic defects such as Zn interstitials and O vacancies that also contribute strongly to optical emissions in the visible region. The amalgamation of the exceptional properties of graphene with good semiconducting properties of ZnO can pave the way towards the realization of future devices.

In this thesis, randomly oriented graphene flakes thin film has been successfully fabricated by using Electrohydrodynamic Atomization (EHDA). Further graphene flakes and zinc oxide (ZnO) nanoparticles have been successfully deposited on substrates (silicon, glass ITO coated) through different approaches like layer by layer, blended and semi-blended approaches. Each fabricated film is directly deposited as cathode electrode in diode to check its performance. It has been observed that a superior performance as cathode has been observed for the decorated graphene flakes film fabricated through layer by layer i.e. decoration of graphene flakes film approach by exhibiting the best current density. Also, for graphene/polymer nano thin composite film, Poly (4-Vinylphenol) dissolved in propylene glycol methyl ether acetate (PGMEA) is deposited by using EHDA technique and has then

been combined with graphene flakes to be used in capacitor. In this case too, it is observed that is giving the behavior of stable capacitor. These composite thin films could be employed in nano and optoelectronic devices, including field effect transistors (FETs), light emitting diodes (LEDs), UV detectors and biosensors.

The fabricated films reported in this thesis compete with the ones made by different intricate and expensive conventional systems. The main advantage is that Electrohydrodynamic process rule outs the use of high vacuum systems therefore making the process cheap and simple. Also material wastage is very low, and inks used in the process are completely inert to the environment thereby making the process clean and user friendly.

# 1. Introduction

2D materials have proven as eye-catching materials in research field nano-electronic devices. After discovery of first 2D crystal material grapheme, lot of attention has been paid to research on such materials. It was an unexpected discovery as theory prohibits existence of 2D crystals but interesting properties and nature of graphene found another way around. Many synthesis routes have been explored for large and small area production. After production transfer mechanisms to functional substrates are investigated.

## 1.1 Graphene

Graphene, a two-dimensional atomically thick carbon atom arranged in a honeycomb lattice, was isolated by repeatedly peeling highly oriented pyrolytic graphite (HOPG) using sticky tape.[ K. S. Novoselov et al. 2004] Since then, outstanding physical properties predicted and measured for graphene have been explored for practical applications (figure 1.1) such as field-effect transistors,[ K. S. Novoselov et al. 2004, V. C. Tung et al. 2009,] chemical sensors[T. O. Wehling et al. 2008,] and composite reinforcement.[A. K. Geim et al. 2009] Monolayer graphene possesses high crystallographic quality and ballistic electron transport on the micrometer scale with only 2.3 % of light absorption.[ R. R. Nair et al. 2008,] Moreover, the combination of its high chemical and thermal stability,[P. Blake et al. 2008] high stretchability,[D. I. Son et al. 2010,] and low contact resistance with organic materials,[S. P. Pang et al. 2009] offers tremendous advantages for using graphene as a promising transparent conductor in organic electronic devices, e.g. solar cells,[ L. G. De Arco et al. 2010] organic light emitting diodes (OLEDs),[P. Matyba et al. 2010] liquid crystal displays (LCDs),[ P. Blake et al. 2008] touch screens,[S. Bae et al. 2010] field effect transistors (FETs),[W. Liu et al. 2010] photodetectors[Y. Cao et al. 2010] and spectroelectrochemistry investigation.[C. M. Weber et al. 2010]

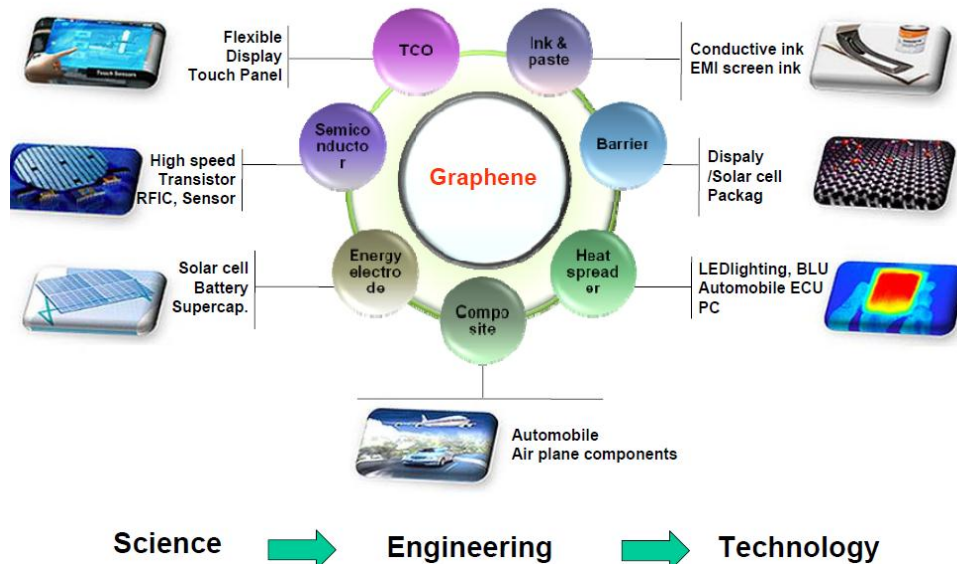


Figure 1-1 Graphene Applications in different fields.

In the view of the contact behavior of the electrodes and the semiconductor layer, graphene is still an ideal electrode for organic electronics. The two dimensional (2D) carbon nanostructure has the excellent compatibility with the organic semiconductors, resulting in a low contact resistance. [Y. Cao et al. 2010] Especially for the flexible organic electronics, the good compatibility is also beneficial for the long-time operation.

The experimental discovery of graphene brought a new alternative to commercially available electrodes. Although research is still at its early stages, graphene already offers several potential advantages over traditional transparent electrodes. [H. A. Becerril et al. 2008, G. Eda et al. 2008, S. Bae et al. 2010] Many groups have already demonstrated the resilience of graphene-based organic photoelectrical devices. The excellent performance of various graphene-based electronic devices gives graphene a realistic chance of being competitive in transparent and bendable technologies.

Recently, graphene-based thin films have attracted considerable attention as they are chemically robust, exhibit high electrical conductivity and good optical transparency in the visible and near-infrared region [A.K. Geim et al. 2007]. This renders these films interesting as electrodes for various applications, e.g., in organic electronic devices [X. Wang et al. 2008] or for spectroelectrochemical studies. Other transparent and conductive thin film materials, such as indium tin oxide or fluorine tin oxide, however, are problematic for several

applications [X. Wang et al. 2008]. Graphene films fabricated from exfoliated graphite oxide, followed by thermal reduction, appear as interesting candidates for electrode applications because of their high conductivity (up to 550 S/cm have been demonstrated) and transmission of 70% in the wavelength range of 1000–3000 nm [X. Wang et al. 2008]. The existence of graphene sheets in such thin films has been evidenced by high-resolution transmission electron microscopy, and bulk Raman spectra revealed the similarity of reduced graphene-oxide with carbon nanotubes or graphite with defects [X. Wang et al. 2008]. It can thus be expected that such graphene films have electronic properties similar to various other  $sp^2$  hybridized carbon-based materials, such as nanotubes or graphite. However, rather little is known about the surface electronic properties of such graphene based films and the surface orientation of graphene sheets over extended areas.

Semiconducting behavior has yet to be demonstrated in graphene-based composites. The compatibility of graphene with polymers and ceramics opens up a route toward realization of semiconducting composite materials from electrically passive host materials.

### ***1.2 Electrohydrodynamic Atomization (EHDA) Deposition and its Applications***

In electrohydrodynamic atomization technique is the thin film deposition phenomenon in which atomization is achieved through electrostatic forces. In fact it is an imbalance between the surface forces arising because of the surface tension of the liquid to be sprayed and Maxwell stresses which are induced because of the electric field, that pull the liquid downwards from the capillary orifice into a stable jet which further disintegrates into smaller droplets because of coulomb forces and hence a cloud of charged, mono-dispersed and extremely diminutive (sometimes up to nanometers) droplets is achieved. A typical electrohydrodynamic Atomization deposition phenomenon consists of following sequence [J. Makela 2010]:

1. Spray formation at the Taylor-cone tip
2. Droplet transport from nozzle to substrate with evaporation of solvent and disruption of droplets at the mid of spray stream
3. Preferential landing on the substrate/ground, and
4. Droplet spreading, penetration and partial drying

An important aspect of EHDA is that droplet agglomeration does not exist at all as the charged droplets are self-dispersing in the space due to mutual Coulomb repulsion. The charge and size of the droplets can be controlled to some extent by adjusting the liquid flow rate and the voltage applied to the nozzle.

Before the spray actually happens, a stable Taylor cone [Chen & Schoonman 2004] is to be achieved which ultimately ejects the spray. A stable, uniform and symmetric Taylor cone at the onset of capillary exit is the guarantee of a smooth and stable EHDA. Important parameters related to Taylor cone formation are the critical onset voltage and liquid flow rate along with liquid physical properties and stand-off distance. A complete description on this aspect of electrohydrodynamics can be found in the next chapter 3.

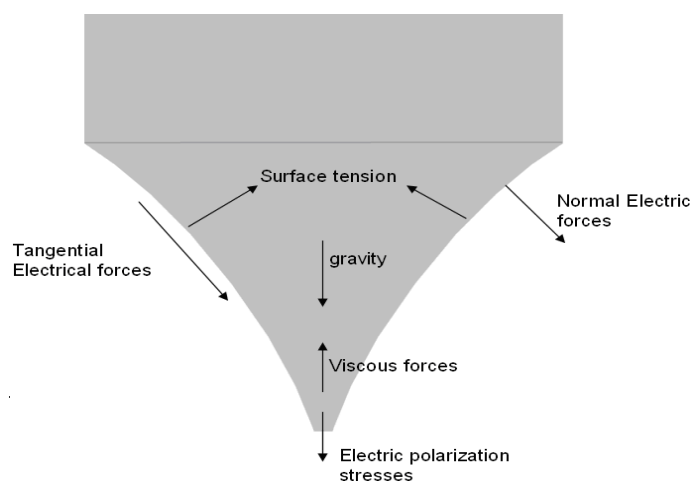


Figure 1-2 Body-force diagram of the Taylor-cone.

If a body force diagram for the fluid in a capillary problem, as shown in Figure 1.2, is looked closely at, three main contributing forces will be witnessed. First is the surface tension force,  $P_s$  which will oppose the generation of meniscus and hence the jet formation. Secondly the hydrostatic pressure,  $P_h$ , which will pull the meniscus downwards and lately, the electrostatic pressure  $P_e$ , is the deciding force which acts tangentially at the meniscus and the amalgam of these forces finally forms the required jet. When put in the equation form, we get

$$P_h + P_s + P_e = 0 \quad (1-1)$$

where

$$P_h = \rho_l g \Delta H \quad (1-2)$$

$$P_e = E_{ds}^2 / 2\varepsilon_r \quad (1-3)$$

$\Delta H$  is the liquid level difference between the container and the free end of the nozzle and  $\varepsilon_r$  is the relative permittivity of the liquid to vacuum permittivity [Chen & Schoonman 2004]. The flow rate is required to compensate fluid in the meniscus, which is directly proportional to the backflow of fluid due to the electrical stress. Thus, the governing force for the ejection of the droplet is electrostatic force since the flow rate is provided to maintain the steady level of ink at the orifice outlet, whereas the gravitational force has little contribution due to the high fluidic resistance in the micro-channel as the capillary diameter is very small and the surface tension of the liquid will add to the fluidic resistance.

EHDA finds its applications almost everywhere, where the competing technologies are applicable. From printed electronics to powder production, from nuclear instruments to solar cells, from Li batteries to fuel cells and bio-applications, EHDA has been in the limelight since its inception. A very comprehensive account mentioning the applications of EHDA has been written by Jaworek [Jaworek 2007] and should be consulted for details.

### ***1.3 Motivation and Introduction of this Thesis***

The motivation of this thesis is to introduce and elucidate that graphene flakes thin film and graphene based composites thin film fabrication through electrohydrodynamic atomization (EHDA) is quite possible. Also, it is showed and proven by using this technique that graphene flakes and graphene based composites thin films can directly be deposited on functional substrates or other preceding thin film in electronic devices. Depositing graphene flakes and graphene based composites directly on substrates by using EHDA technique is first time taken into account. Therefore, it is very necessary that EHDA should be given further attention for its successful use in the fabrication of graphene flakes and graphene based thin film composites which can be used in different microelectronic and optoelectronic devices.

In this work graphene flakes, blended graphene/Zinc Oxide, Semi-blended graphene/Zinc Oxide, decoration of graphene flakes film with ZnO nano particles, PVP and Graphene/PVP blended functional thin films are fabricated using EHDA technique. Graphene, graphene based composite films are employed as cathode electrode in diode device and PVP and graphene/PVP films are employed in metal/insulator/semiconductor device for capacitance

measurement. The thin films mentioned in this thesis are fully characterized and hence this demonstration can act as a breakthrough in the field of printed electronic industry struggling for large area deposition of graphene flakes and graphene based composites thin films.

The remaining part of this thesis has been divided into 4 chapters where the next chapters give a brief introduction of graphene. While a complete account on EHDA technique is given in chapter three. Chapter four is consisted of full graphene flakes and graphene based composites films fabrication from solution while using EHDA technique and their employment to electronic devices and characterizations. In the end a chapter is dedicated to the Summary of the thesis.



## 2. Background and Literature Survey

### 2.1 Graphene

Graphene is a name given to a flat/2D monolayer of  $sp^2$  bonded carbon atoms closely packed into a honeycomb lattice with a nearest neighbor distance of 0.14 nm. Graphene can be considered as the mother structure of all the carbon based materials. It has been generally used in the approximation of the crystal structure and properties of graphite, carbon nanotubes and Bucky-balls. For instance, graphite is made up of loosely stacked (ABAB type) graphene layers with an interlayer distance of 0.34 nm. This large interlayer separation, compared to the in-plane nearest neighbor distance, makes graphite a quasi 2D system.

Carbon nanotubes are usually considered as graphene layers rolled into hollow seamless cylinders and a  $C_{60}$  buckyball can be considered as a graphene sheet, where some hexagons are replaced by pentagons, which cause a crumpling of the sheet into a final formation of a graphene sphere or a graphene football, in figure 2.1 a clear depiction is sketched. Andre Geim and Konstantin Novoselov won the 2010 Nobel Prize in Physics for this trailblazing discovery. This graphene gold rush has begun for good reasons, primarily owing to its several exceptional properties which are described in this section of the chapter.

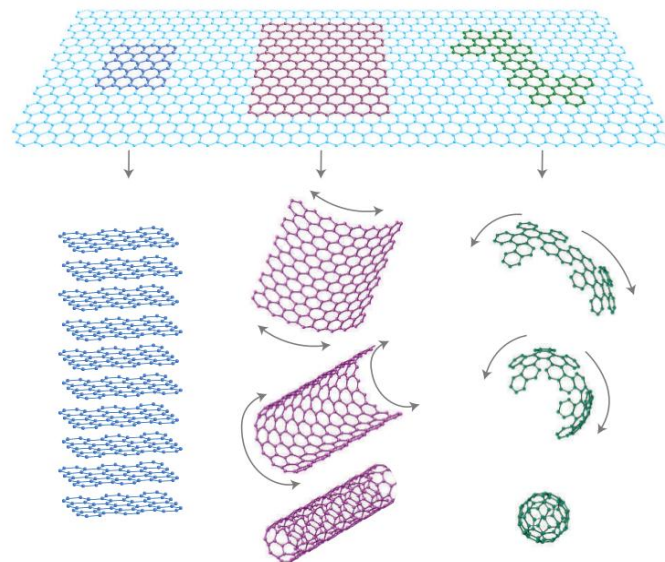


Figure 2-1 Depictions of graphene, graphite, carbon nanotubes and buckyballs.

### 2.1.1 Crystal Structure

The crystalline structure of graphene consists of 2D hexagonal lattice with a primitive cell containing two atoms (A and B), as shown in figure 2.2. Each carbon atom is covalently bonded to three other atoms in the plate and the angle between two successive bonds is  $120^\circ$ . The outermost electron shell of a carbon atom has four valence electrons, three of which are used by the covalent bonds. The fourth valence electron does not take part in covalent bonds and may be mobilized from the electron shell by means of an electric field to give rise to conductivity. The graphene layers are bonded to each other by weak Van der Waals forces within graphite. This weakly bonded layered structure of graphite allows for the separation of individual graphene sheet.

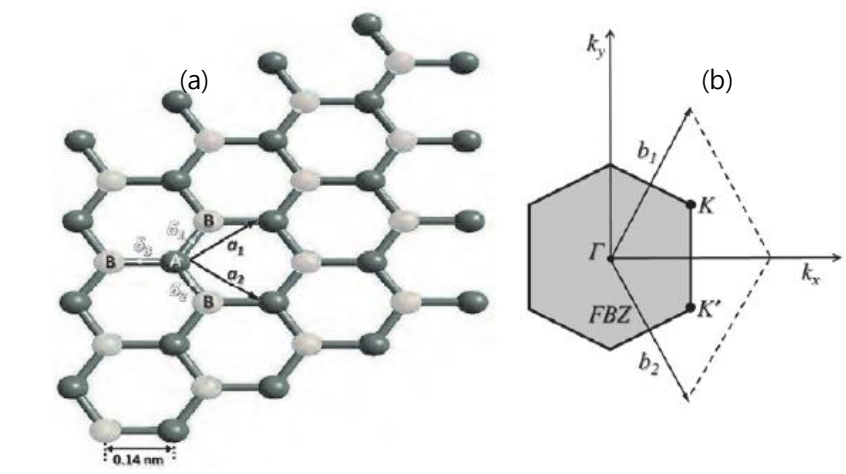


Figure 2-2 (a) Triangular sublattices of graphene, each atom in sublattice “A” has 3 nearest neighbors in sublattice “B” and vice versa and (b) First Brillouin Zone of graphene reciprocal lattice.

### 2.1.2 Morphology and Structure

The graphene honeycomb lattice is composed of two equivalent sub-lattices of carbon atoms bonded together with  $\sigma$  bonds. Each carbon atom in the lattice has a  $\pi$  orbital that contributes to a delocalized network of electrons. Whether freely suspended graphene has ‘intrinsic’ ripples or not has been addressed by Monte Carlo simulation [A. Fasolino et al. 2007] and transmission electron microscopy (TEM) studies [J.C. Meyer et al. 2007]. The microscopic corrugations were estimated to have a lateral dimension of about 8 to 10 nm and a height displacement of about 0.7 to 1 nm. Sub-nanometer fluctuations in height for graphene platelets deposited on  $\text{SiO}_2$ -on-Si substrate were studied by scanning tunneling microscopy (STM) [E. Stolyarova et al. 2007].

Apart from ‘intrinsic’ corrugations, graphene in real 3D space can have other ‘defects,’

including topological defects (e.g., pentagons, heptagons, or their combination), vacancies, adatoms, edges/cracks, adsorbed impurities, and so on. Individual adatoms on graphene, and carbon chains and vacancies, generated by knock-on by the electron beam in TEM (working at 100 kV) could be investigated dynamically, providing insights into generation of defects and their evolution [J.C. Meyer et al. 2008].

## **2.2. Graphene Properties**

### **2.2.1 Optical Properties**

The high-frequency conductivity for Dirac fermions in graphene has been stated to be a constant equal to  $\pi e^2/2h$ , from the infrared through the visible range of the spectrum [N.M R. Peres et al. 2006 & V. P. Gusynin et al. 2006]. The optical transmittance  $T$  and reflectance  $R$  are then  $T = (1 + 1/2\pi\alpha)^{-2}$  and  $R = 1/4\pi^2\alpha^2 T$  for normal incidence light (where  $\alpha = 2\pi e^2/hc \approx 1/137$ ,  $e$  is the electron charge,  $c$  the light speed, and  $h$  Planck's constant); the opacity is  $(1-T) \approx \pi\alpha \approx 2.3\%$ . The expression of  $T$  and  $R$  in terms of fundamental constants that do not directly involve material parameters is stated to be a result of the structure and electronic properties of graphene [N. M. R. Peres et al. 2009]. As shown in Figure 2.3, this constant transparency ( $\approx 97.7\%$ ) has been experimentally observed for graphene in the visible range and the transmittance linearly decreases with the number of layers for n-layer graphene [R.R. Nair et al. 2008]. A deviation from this 'universal behavior' has been found for incident photons with energy lower than 0.5 eV, which was attributed to the finite temperature and a doping-induced chemical potential shift of the charge-neutrality (Dirac) point [K.F. Mak et al. 2008]. Inter-band optical transitions in graphene have been probed by infrared spectroscopy, and gate-dependent optical transitions have been reported [F.Wang et al. 2008]. Due to the low density of states near the Dirac point in graphene, a shift of the Fermi level due to the gate causes a significant variation of charge density, leading to a significant change in transmission. The relaxation and recombination of photo-generated electron-hole pairs in graphene occurs on a timescale of tens of picoseconds, depending on the carrier concentration of graphene [P.A. George et al. 2008, F. Rana et al. 2009]. Given the high carrier transport velocity even under a moderate electrical field, an ultrafast (up to 40 GHz) and efficient (6–16% internal quantum efficiency) photo response has been observed for graphene field effect transistors (FET), [F. Xia et al. 2009] suggesting graphene-based high speed optoelectronic devices for communications, detection, sensing, and so on.

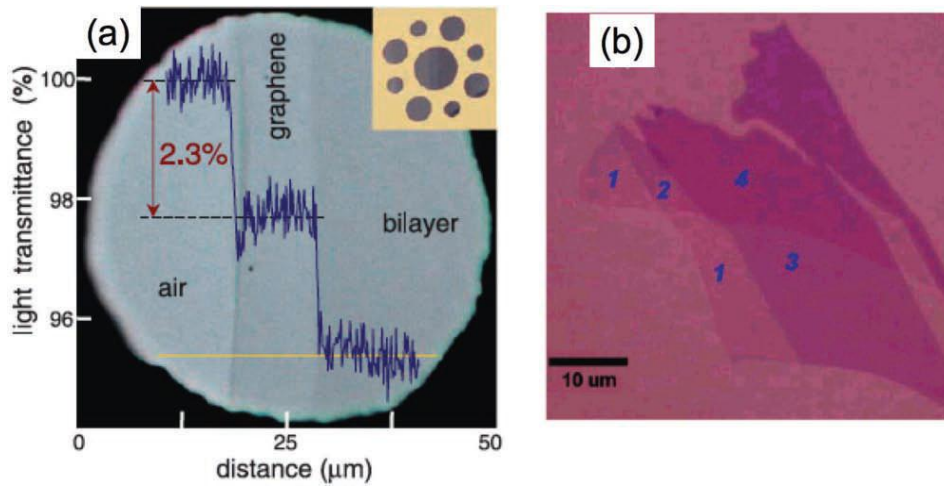


Figure 2-3 (a) Photograph of a 50-  $\mu$  m aperture partially covered by graphene and its bilayer. The line scan profile shows the intensity of transmitted white light along the yellow line. Inset shows the sample design: a 20-  $\mu$  m thick metal support structure has apertures 20, 30, and 50  $\mu$  m in diameter with graphene flakes deposited over them; (b) Optical image of graphene flakes with one, two, three, and four layers on a 285-nm thick SiO<sub>2</sub> - on-Si substrate.

### 2.2.2 Raman Spectroscopy of Graphene

Raman spectroscopy has been used to characterize graphene and several review articles have been published discussing the optical phonon spectrum and Raman spectrum of graphene [A.C. Ferrari et al. 2007]. The Raman spectra of graphene includes the G peak located at  $1580\text{ cm}^{-1}$  and 2D peak at  $2700\text{ cm}^{-1}$ , caused by the in-plane optical vibration (degenerate zone center  $E_{2g}$  mode) and second-order zone boundary phonons, respectively. The D peak, located at  $1350\text{ cm}^{-1}$  due to first-order zone boundary phonons, is absent from defect-free graphene, but exists in defected graphene. It was proposed that Raman could be used to distinguish the ‘quality’ of graphene and to determine the number of layers for n-layer graphene (for n up to 5) by the shape, width, and position of the 2D peak [A.C. Ferrari et al. 2009]. As shown in Figure 2.4, the 2D peak shifts to higher wave number values and becomes broader for an increasing number of layers.

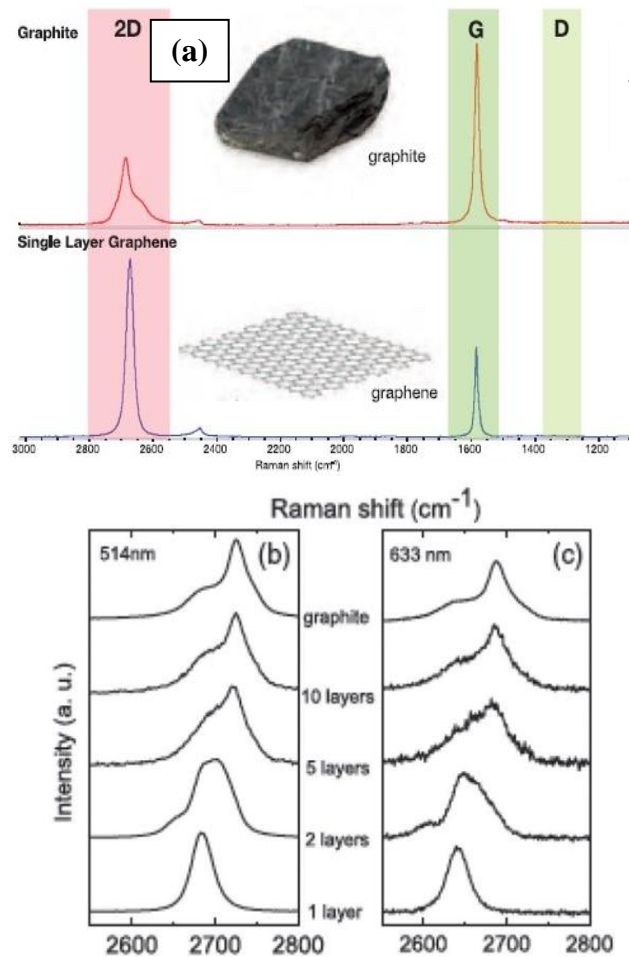


Figure 2-4 (a) Comparison of Raman spectra at 514 nm for bulk graphite and graphene. They are scaled to have similar height of the 2D peak at  $2700\text{ cm}^{-1}$ ; (b) Evolution of the spectra at 514 nm with the number of layers; (c) Evolution of the Raman spectra at 633 nm with the number of layers.

The shifting and splitting of Raman modes can be used to analyze mechanical strain in graphene. For example, Raman spectra of epitaxial graphene grown on SiC show a significant phonon ‘hardening’ (blue shift of the G and 2D peaks), mainly due to the compressive strain that occurs when the sample is cooled down after growth [J. Rohrl et al. 2008, Z.H. Ni et al. 2008]. The frequency of the G and 2D peaks can also be tuned by charge doping through electron-phonon coupling changes [J. Yan et al. 2007, S. Pisana et al. 2007]. The Raman spectral signatures of epitaxial graphene grown on SiC, especially the width of the 2D peak, have been correlated to the carrier mobility of the graphene [J.A. Robinson et al. 2009]. The intensity ratio of the D and G peak has been used as a metric of disorder in graphene, such as arising from ripples, edges, charged impurities, presence of domain boundaries, and others [A.C. Ferrari et al. 2007]. For edges, the intensity of the D peak depends on the edge structure; it is weak at the zigzag edge and strong at the armchair edge [C. Casiraghi et al. 2009, Y.M. You et al. 2008].

### 2.2.3 Thermal Properties

Since the carrier density of non-doped graphene is relatively low, the electronic contribution to thermal conductivity (Wiedemann-Franz law) is negligible. The thermal conductivity ( $\kappa$ ) of graphene is thus dominated by phonon transport, namely diffusive conduction at high temperature and ballistic conduction at sufficiently low temperature [C.H. Yu et al. 2005].

MD simulations [S. Berber et al. 2000] based on the Green-Kubo approach have shown a  $\kappa \propto 1/T$  dependence for defect-free graphene as temperature  $T$  increases beyond about 100 K. A room temperature thermal conductivity of about  $6000 \text{ Wm}^{-1}\text{K}^{-1}$  for a suspended monolayer graphene was predicted, and this value was stated to be much higher than that of graphitic carbon [S. Berber et al. 2000]. Non-equilibrium MD was used to investigate the  $\kappa$  of GNRs with different edge shapes as a function of length, width, and strain [Z. Guo et al. 2009]. It was found that  $\kappa$  follows a power law dependence on the length  $L$  of GNRs ( $\kappa \propto L^\beta$ ), where  $\beta$  varies from 0.3 to 0.5 at room temperature. It was stated that the strong length dependence of thermal conductivity on  $L$  may indicate very long phonon mean free paths in GNRs.

### 2.2.4 Mechanical properties

The basic constitution of the graphene lattice is the C-C covalent bond which is one of the strongest bond in nature. The strength of this  $sp^2$  C-C bonds gives graphene some exceptional mechanical properties, possibly better than any other material. There are several elastic parameters necessary to define the mechanical properties: e.g. the Young's modulus ( $E$ ), the Poisson's ratio and the shear modulus ( $G$ ).

Mechanical properties of free-standing monolayer graphene membranes have been measured experimentally by nano indentation in an atomic force microscope. These measurements correspond to a Young's modulus of  $E = 1.0 \pm 0.1 \text{ TPa}$  and a third-order elastic stiffness of  $D = -2.0 \pm 0.4 \text{ TPa}$ , assuming an effective graphene thickness of 0.335 nm [C.Lee et al. 2008]. The shear modulus ( $G$ ), has been reported to be 280 GPa for CVD grown graphene films [X. Liu et al. 2012]. Second and third order elastic stiffness was measured to be  $340 \text{ Nm}^{-1}$  and  $690 \text{ Nm}^{-1}$ , respectively. The fracture strength has been measured to be 125 GPa [J. Wang et al. 2012], representing the intrinsic strength of a defect free graphene sheet [C.Lee et al. 2008].

These exceptional mechanical properties of graphene make it a perfect choice for application

like transparent/flexible electrodes [S.Pang et al. 2011], reinforcement in advanced composites [J. Wang et al. 2012] and nanoelectromechanical systems (NEMS) [A.M. v. d. Zande et al. 2010].

### 2.2.5 Electrical Properties of Graphene

In most conductors, the valence and conduction bands overlap, giving excited electrons many states to occupy as they move throughout the material. Materials with this property are known as metals. Graphene, while an excellent conductor, is not a metal but rather a zero-gap semiconductor. While the valence and conduction bands do not overlap in graphene, they touch at the Fermi level [Christian Schonberger 2000]. This can be seen by visualizing the Fermi surface of a 2D graphene lattice, as in Figure 2.5. The Fermi surface for a lattice material is the energy border between the valence and conduction bands in momentum space. For this border to be defined the Fermi energy must fall inside an energy band and not in a band gap; otherwise the valence and conduction bands do not touch at all. Thus, Fermi surfaces only exist for conductors. Graphene's Fermi surface consists of six double cones with the Fermi energy at the intersection of those cones. Because the cones are linear near this intersection the effective mass of electrons in this region is zero. This leads to an entirely new transport mechanism in graphene compared to metals. The specifics of this regime rely on quantum electrodynamics and Dirac's relativistic equation of state. The results can be conceptualized by thinking of charge carriers in graphene not as individual electrons, but as interacting groups of electrons that behave as an entirely different type of particle called a Dirac fermion, these charge carriers travel ballistically over the 2D surface at relativistic speeds [K. S. Novoselov, et al. 2005]. Because of this fundamentally different transport regime, pure graphene is able to conduct electricity better than metals, with room-temperature resistivity on the order of  $10^{-6} \Omega\text{-cm}$  [A. A. K. Geim. et al. 2007].

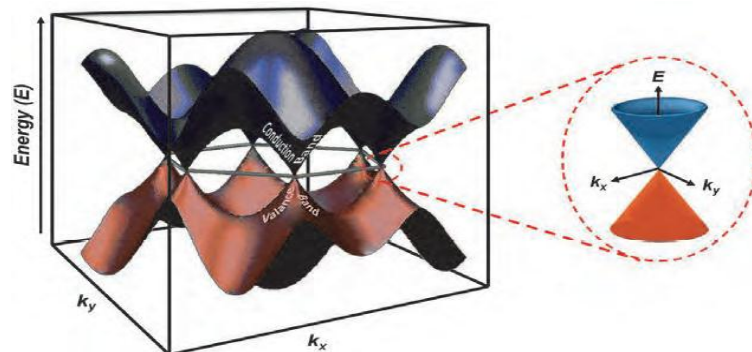


Figure 2-5 Fermi surface showing Dirac Cones and the zero-gap nature of graphene.

## 2.3 Synthesis Methods of Graphene and Resulting Material Properties

Graphene has shown many interesting properties from the mechanical, electrical, thermal and optical point of view. These properties make graphene a material of interest for many applications, for example in the fields of electronics, composites, sensors as well as energy storage and conversion. These engineering applications require availability of graphene on the mass scale and thus the development of suitable processes is necessary. Figure 2.6 has shown different routes to graphene synthesis.

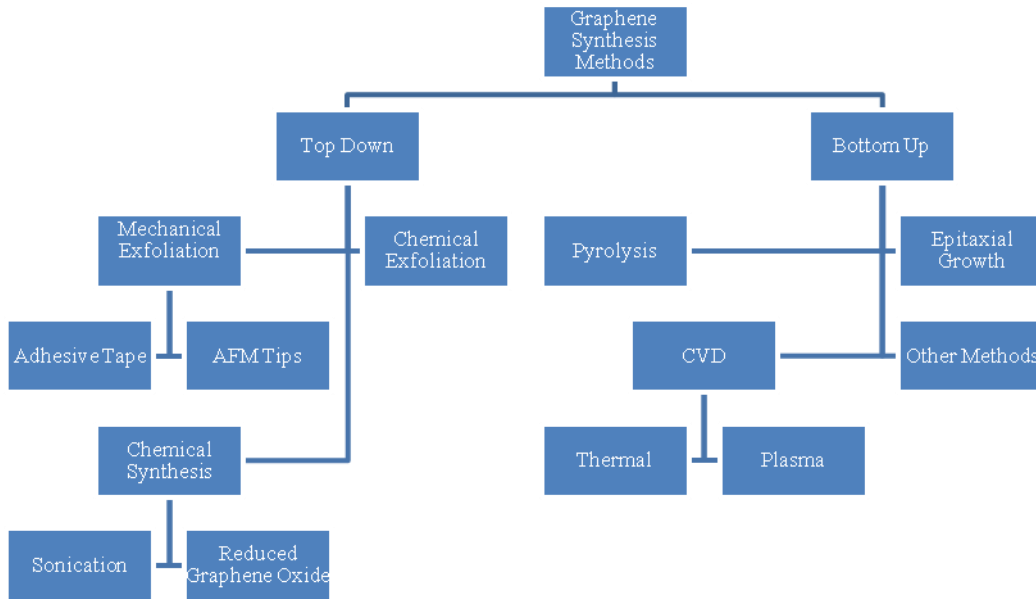


Figure 2-6 Schematic representation of the different graphene synthesis methods.

### 2.3.1 Mechanical Exfoliation

Mechanical exfoliation is the first recognized method of graphene synthesis. This is a top-down technique in nanotechnology, by which a longitudinal or transverse stress is generated on the surface of the layered structure materials using simple scotch tape or AFM tip to slice a single layer or a few layers from the material onto a substrate. Graphite is formed when mono-atomic graphene layers are stacked together by weak van der Waals forces. The interlayer distance and interlayer bond energy is  $3.34 \text{ \AA}$  and  $2\text{eV/nm}^2$ , respectively. For mechanical cleaving,  $\sim 300 \text{ nN}/\mu\text{m}^2$  external force is required to separate one mono-atomic layer from graphite (Zhang et al. 2005). As seen in Figures 2.7(a) and 2.7(b), the thin multilayered graphite was fabricated with the lowest thickness of  $\sim 200 \text{ nm}$ , which consists of 500–600 layers of monolayer graphene.



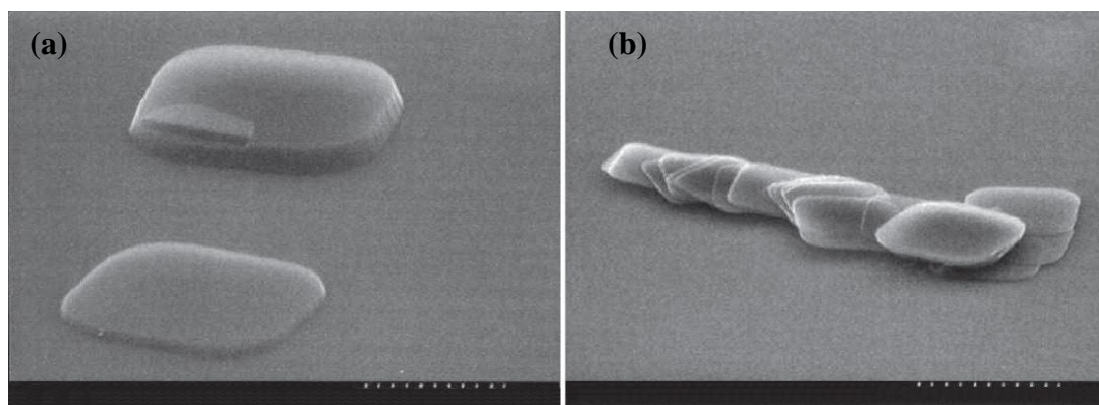


Figure 2-7 (a) and (b): Scanning electron micrographs of mechanically exfoliated thin graphite layers from highly oriented pyrolytic graphite (HOPG) by AFM tip.

The graphene produced by these mechanical exfoliation techniques was used for fabrication of FET devices, which brought a research boom in the field of carbon nanoelectronics.

### 2.3.2 Chemical Exfoliation

Like mechanical exfoliation, chemical exfoliation is one of the established methods for fabricating graphene. Chemical exfoliation is a process by which alkali metals are intercalated with the graphite structure to isolate few-layer graphene dispersed in solution. Alkali metals are the materials in the periodic table that can easily form graphite-intercalated structures with various stoichiometric ratios of graphite to alkali metals. One of the major advantages of alkali metals is their ionic radii, which are smaller than the graphite interlayer spacing; hence they fit easily in the interlayer spacing as shown in the schematic in figure 2.8(a).

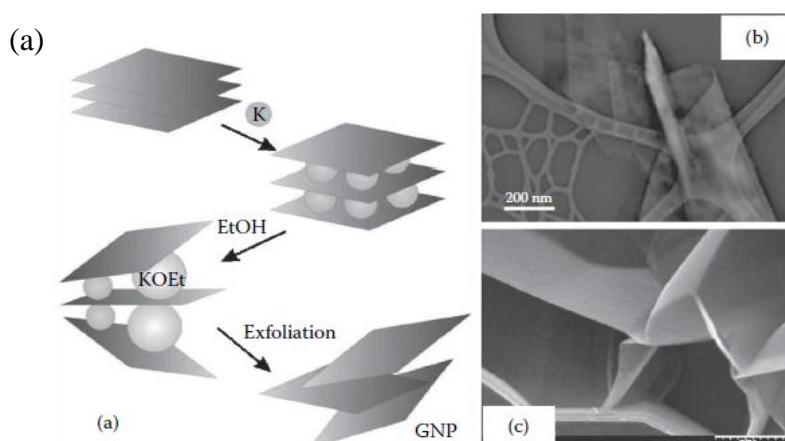


Figure 2-8 (a) Schematic illustrating the chemical exfoliation process, (b) transmission electron micrograph (TEM) of chemically exfoliated graphitic nanosheet, (c) SEM picture of thin graphite nanosheets after the exfoliation process, showing approximately a 10-nm thickness of ~30 layers of single graphite sheet.

### 2.3.3 Some Other Novel Routes of Graphene Synthesis

In addition to the synthesis methods discussed previously, mechanical exfoliation of graphene produced by high-velocity clusters impacting on a graphite surface [Sidorov et al. 2010]. The graphene nanoribbon produced by this method was ~30 nm thick. Also, Xin et al. (2010) indicated graphene exfoliated from microwave irradiation of graphite-intercalated compounds in a solution process followed by combining those exfoliated sheets with carbon nanotubes (CNTs). Plasma-assisted etching of graphite to form multilayered graphene and monolayer graphene was also demonstrated in another report [Hazra et al. 2011]. This is another top-down approach that involves the gradual thinning process of graphite to graphene using plasma in an H<sub>2</sub> and N<sub>2</sub> atmosphere.

### 2.3.4 Chemical Synthesis: Graphene from Reduced Graphene Oxide

Chemical synthesis is a top-down indirect graphene synthesis method, and is the first method that demonstrated graphene synthesis by a chemical route. The method involves the synthesis of a graphite oxide (GO) by oxidation of graphite, dispersing the flakes by sonication, and reducing it back to graphene. There are three popular methods available for GO synthesis: the Brodie method (Brodie 1860), Staudenmaier method (Staudenmaier 1898), and Hummers and Offeman method (Hummers and Offeman 1958). All three methods involve oxidation of graphite using strong acids and oxidants. GO was first prepared by Brodie (1860), by mixing graphite with potassium chlorate and nitric acid. However, the process contains several steps that are time consuming, unsafe, and hazardous. In order to overcome those problems, Hummers (Hummers and Offeman 1958) developed a method for fabricating graphite oxide by mixing graphite with sodium nitrite, sulfuric acid, and potassium permanganate, well known as Hummers method, figure 2.9.

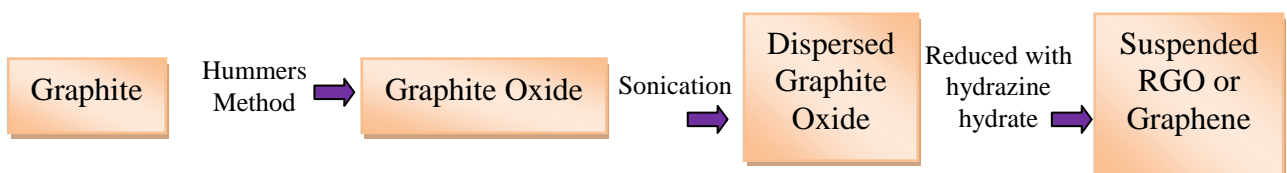


Figure 2-9 The process flow chart of graphene synthesis derived from graphite oxide.

The chemical synthesis method was brought into focus again in 2006 when Ruoff and his

coworkers produced mono-atomic graphene by a chemical synthesis process [Stankovich, Dikin, et al. 2006, Stankovich, Piner, et al. 2006]. They prepared GO by the Hummers method and chemically modified GO to produce a water-dispersible GO. GO is a stacked layer of squeezed sheets with AB stacking, which exhibits an oxygen containing functional group like hydroxyl and epoxide in their basal plane when it is highly oxidized [Jeong et al. 2008]. The attached functional groups (carbonyl and carboxyl) are hydrophilic in nature, which facilitates the exfoliation of GO upon ultrasonication in an aqueous medium. Thus, the hydrophilic functional groups accelerate the intercalation of water molecules between the GO layers. In this process, functionalized GO is used as a precursor material for graphene production, which forms graphene upon reduction with dimethylhydrazine at 80°C for 24 hr [Stankovich et al. 2006] showed that chemical functionalization of GO flakes by organic molecules leads to the homogeneous suspension of GO flakes in organic solvents. They reported that reaction of graphite oxide with isocyanate results in isocyanate-modified graphene oxide, which can be dispersed uniformly in polar aprotic solvents like dimethylformamide (DMF), N-methylpyrrolidone (NMP), dimethyl sulfoxide (DMSO), and hexamethylphosphoramide (HMPA). The proposed mechanism states that the reaction of isocyanate with hydroxyl and carboxyl groups generates the carbamate and amide functional groups, which become attached to the GO flakes (as shown in figure 2.10).

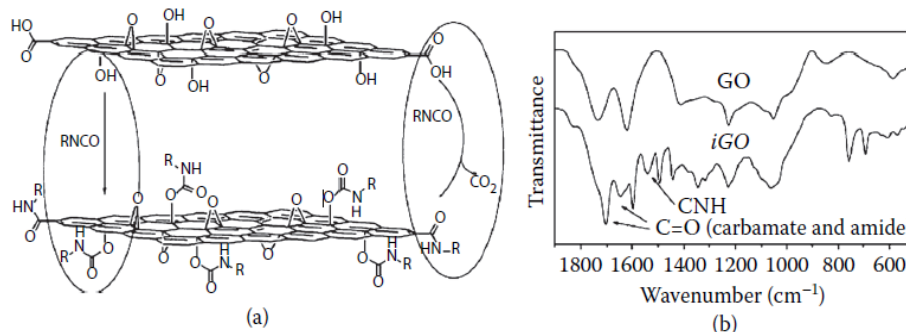


Figure 2-10 Mechanism proposed by Stankovich et al. on isocyanate-treated GO where organic isocyanates react with the hydroxyl (left oval) and carboxyl groups (right oval) of graphene oxide sheets to form carbamate and amide functionalities, respectively. (b) Representative FT-IR spectra of GO and phenyl isocyanate-functionalized GO.

### 2.3.5 Electrochemical Synthesis

Electrochemical synthesis of graphene sheets is a one step treatment [N. Liu et al. 2008] and can be classified as subcategory of graphite exfoliation. In this case, two high purity graphite rods are used as electrodes. In the electrochemical cell they are immersed in the electrolyte bath composed of ionic liquid and water. The schematic of the ECC are shown in figure 2.11

and figure 2.12, respectively.

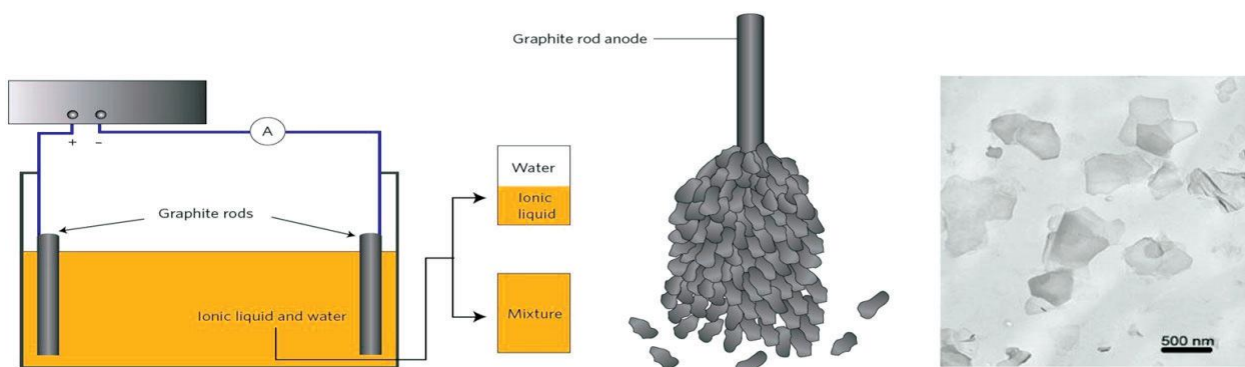


Figure 2-11 Left: experimental schematics; middle: exfoliation of chemically modified graphene sheets from the graphite anode; right: TEM image of resulting graphene material with width of 500 nm, length 700 nm and thickness of ~1nm).

Static potential is applied to the two electrodes. Under these conditions the anode is corroding and a black precipitate is gradually appearing in the reactor. After electrolysis, stable graphene dispersion is obtained. The supernatant can be directly filtered to form a graphene paper, or washed and dried to obtain bulk powders of graphene. In Figure 6 the filtered material is shown.

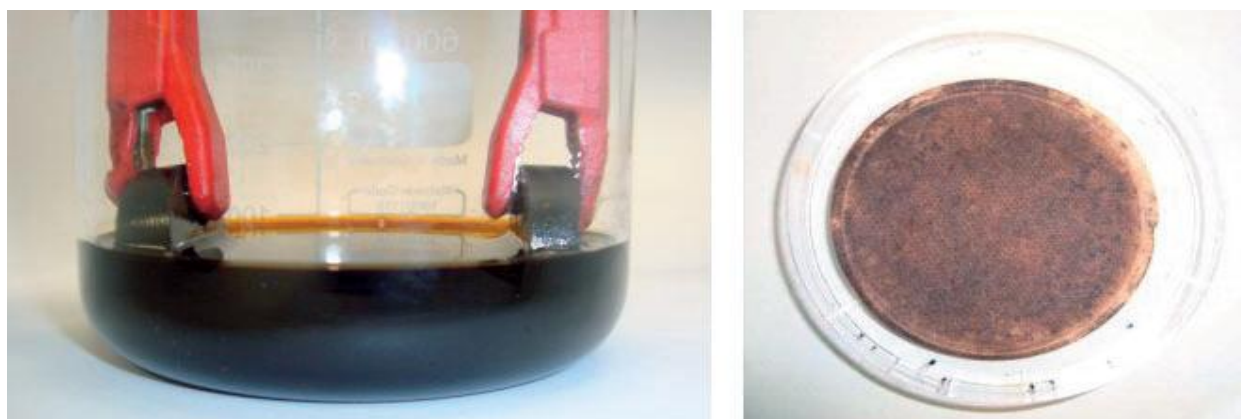


Figure 2-12 Left: Experimental setup for electrochemical production of graphene. Right: The product obtained after filtration of the electrolyte solution.

Chemical synthesis of graphene has several advantages such as a low temperature process, and therefore could be readily processed on any substrate with much more flexibility. In situ, functionalized graphene with different functional groups can be easily synthesized via this route for chemical and biological applications. Further, the process is low in cost as graphite is abundant in nature (natural graphite supplies worldwide are estimated at 800M tons). In contrast, the chemical syntheses of graphene have several disadvantages such as small yield, defective graphene, and partially reduced GO, which readily deteriorates the properties of graphene.

### ***2.3.6 Direct Chemical Synthesis: Pyrolysis of Sodium Ethoxide***

All chemical synthesis processes described above are top-down approaches as the process involves the oxidation of bulk graphite, exfoliation of GO, and then reduction back to graphene. In contrast, a bottom-up approach of chemical synthesis of graphene, called the *solvothermal method*, is introduced (Choucair, Thordarson, and Stride 2009). In this method, laboratory-grade ethanol and sodium were used as starting materials to synthesize sodium ethoxide, followed by pyrolyzation, which yields a fused array of graphene sheets that can be easily dispersed using mild sonication. The solvothermal reaction involves a reaction of 1:1 molar ratio of sodium (2 g) and ethanol (5 ml) in a sealed reactor vessel at 220°C for 72 hr, resulting in a yield of sodium ethoxide, which was used as a graphene precursor for further reaction. The resultant solid (sodium ethoxide) was rapidly pyrolyzed, vacuum filtered, and dried in a vacuum oven at 100°C for 24 hr. The process yield was 0.1 g/ml of ethanol, typically yielding ~0.5 g per reaction. The advantage of this process is a low-cost and bottom-up process that can be further extended to the more controlled fabrication of high-purity, functionalized graphene. Moreover, it is a scalable, low-temperature process, which is an added advantage of the direct bottom-up chemical synthesis methods yielding high-purity graphene.

### ***2.3.7 Unzipping of Nanotubes***

A new graphene synthesis process was proposed that involves unzipping a carbon nanotube by using a chemical and plasma-etched method. The unzipping of carbon nanotubes (CNTs) yields a thin elongated strip of graphene that exhibits straight edges, called a graphene nanoribbon (GNR). Graphene, when narrowing along the width, deliberately transforms its electronic state from semimetal to semiconductor [Chen et al. 2007]. Therefore, the electronic properties of thin strip graphene nanoribbons are presently under vigorous investigation [Jiao et al. 2010, Jiao et al. 2009]. Depending upon whether the starting nanotube is multiwalled or single walled, the final product will be multilayered graphene or single-layer graphene, respectively.

Cano-Marquez et al. (2009) demonstrated a novel chemical route of longitudinal unwrapping of multiwalled carbon nanotubes (MWNTs) by intercalation of lithium (Li) and ammonia

(NH<sub>3</sub>) followed by exfoliation. They used CVD-grown MWNTs dispersed in dry tetrahydrofuran (THF) followed by adding liquid NH<sub>3</sub> (99.95%), while maintaining the dry ice bath temperature of -77°C. Li was added with the ratio of 10:1 (Li:C) and allowed the intercalation of MWNT to occur for a few hours. Subsequently, HCl was mixed in the solution containing intercalated MWNTs, which further facilitate complete exfoliation. They proposed a mechanism for intercalation that was initiated by electrostatic attraction between the negatively charged MWNTs and NH<sub>3</sub>-solvated Li<sup>+</sup>. The exothermic reaction occurs when the HCl reacts with Li ions and simultaneous neutralization of NH<sub>3</sub> causes further unwarping of the nanotubes. Some of the unexfoliated or partially exfoliated nanotubes were also obtained, which could be further exfoliated by thermal treatments. The process yields ~60% fully exfoliated MWNTs including a very small amount (0-5%) of partially exfoliated MWNTs. The step-by-step fabrication process from nanotube to nanoribbon is shown in figure 2.13.

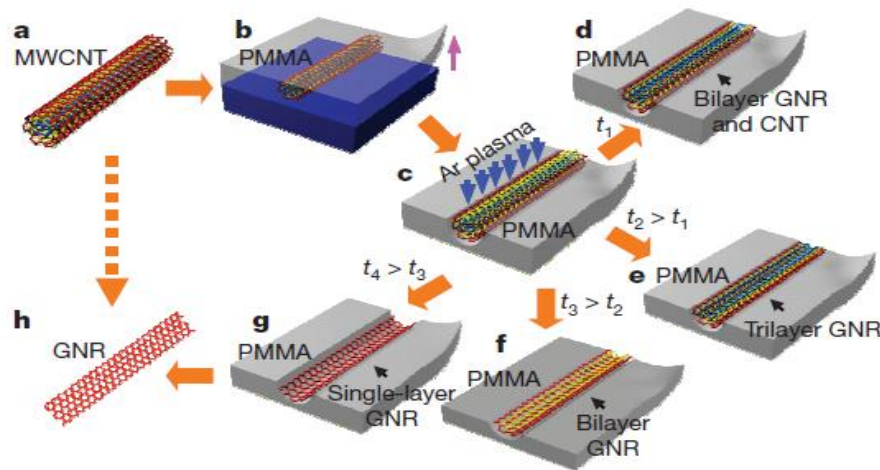


Figure 2-13 A process flow chart of graphene nanoribbon fabrication from a carbon nanotubes by the plasma etching process.

### 2.3.8 Thermal Chemical Vapor Deposition Process

Thermal chemical vapor deposition (CVD) is a chemical process by which a substrate is exposed to thermally decomposed precursors and the desired product deposited onto the substrate surface at high temperature. Because the high temperature is not desired in many cases, plasma-assisted decomposition and reaction may lower the process temperature. Figures 2.14(a) and 2.14(b) demonstrate the schematic of thermal and plasma-enhanced CVDs (PECVD), respectively.

There are numerous advantages to the thermal CVD process. The process yields high quality and high purity final products in large scale. Moreover, by controlling the CVD process

parameters, control over the morphology, crystallinity, shape, and size of the desired product is possible. On the other hand, by applying a wide range of solid, liquid, and gaseous precursor materials, a large variety of nano-materials and thin films are executable with this process.

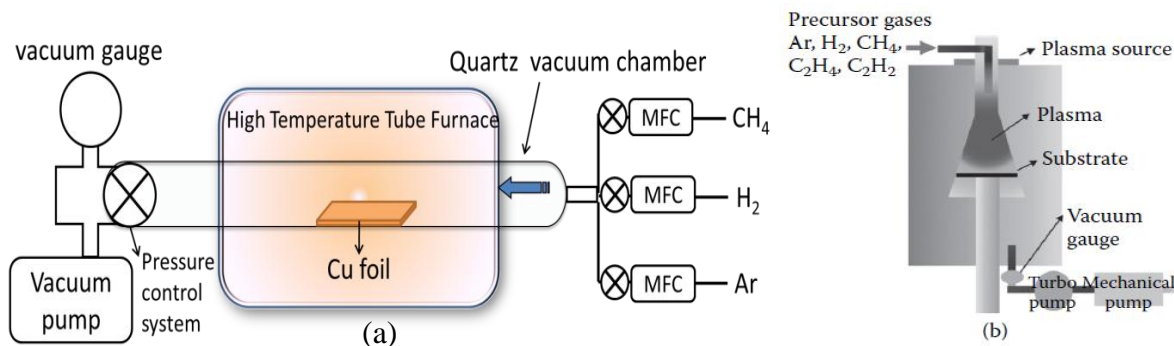


Figure 2-14 Schematic of (a) thermal CVD and (b) plasma-enhanced CVD (PECVD).

### 2.3.9 Thermal Chemical Vapor Deposition

Deposition of mono-layer graphitic materials on Pt by thermal CVD was first reported in 1975 by Lang et al. (1975). They found that the decomposition of ethylene onto platinum results in the formation of a graphitic over layer and surface rearrangements of the substrate. Since then (almost two decades), the field has not been explored further due to an inability to find possible applications of thin graphite film as a semiconductor, transparent conductor, and so on. In the early twenty-first century, discovery of graphene created a research boom because the unusual properties of thin monolayer or few layer graphite films have been explored, attracting tremendous attention from the scientific and industrial communities. Furthermore, the physics and chemistry of graphene have been carefully examined to open a new area of graphene-based electronics [Novoselov et al. 2004, Dreyer et al. 2010].

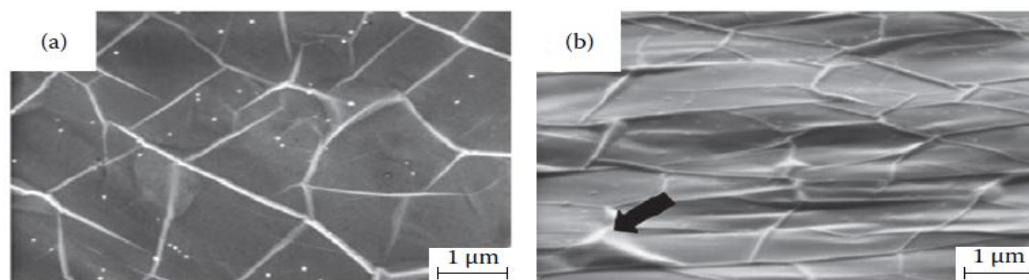


Figure 2-15 Scanning electron micrograph of graphene syntheses on Ni (111) by the DC discharge method.

In 2008, Pei et al. [Yu et al. 2008] demonstrated high-quality graphene formation on polycrystalline Ni during thermal CVD of methane. They fabricated few layer graphene at 1000°C using CH<sub>4</sub>: H<sub>2</sub>: Ar =0.15:1:2 with a total gas flow rate of 315 sccm (standard cubic centimeters per minute) under ~1 atmospheric pressure. From high-resolution TEM (HRTEM) study (Figure 2.16(a)), they confirmed the formation of 3–4 layers of graphene on Ni and suggested that the graphene formation is due to the segregation of carbon on Ni. They also reported that the cooling rates (fast ~20°C/s, medium ~10°C/s, and slow ~0.1°C/s) significantly affect the formation of different numbers of graphene layers, which was further confirmed by Raman spectroscopy (as shown in Figure 2.16(b)). However, large-scale monolayer graphene production using thermal CVD was still in demand until an interesting report in 2009 (Kim et al. 2009) regarding large-scale patterned growth of graphene films as stretchable transparent electrodes. Kim et al. (2009) demonstrated graphene growth over e-beam evaporated Ni followed by thermal CVD of CH<sub>4</sub>:H<sub>2</sub>:Ar ~550:65:200 at 1000°C.

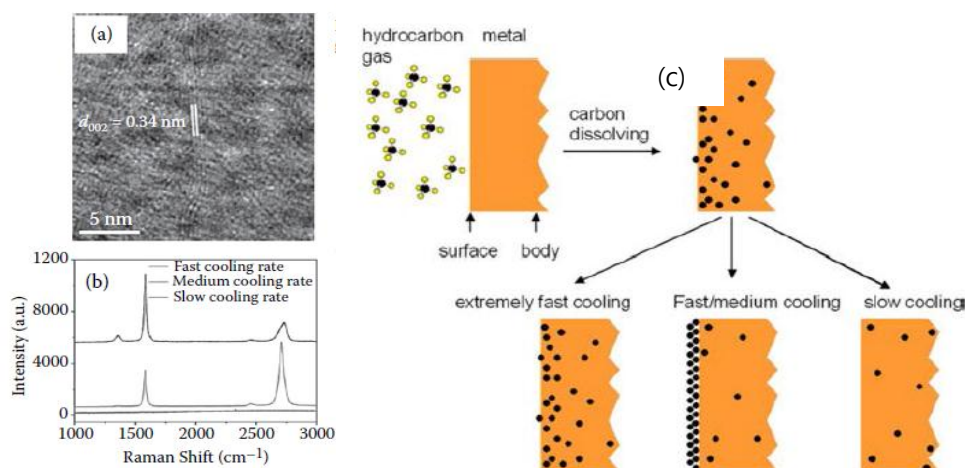


Figure 2-16 (a) HRTEM of graphene precipitated on Ni, (b) Raman spectra confirming the effect of cooling rate on graphene formation, and (c) schematic representing the mechanism of carbon segregation on Ni.

Bae et al. (2010) reported the roll-to-roll production of graphene on a flexible polymer with an area as large as 30 inches as shown in figure 2.17(a) and used as a touch screen panel. They grew graphene using thermal CVD on Cu foil and the processing steps are as follows: (1) annealing of Cu in a thermal CVD in a H<sub>2</sub> environment (under ~90 mT pressure) at 1000°C, (2) processing of graphene growth at 1000°C using the precursor gas mixture of CH<sub>4</sub> and H<sub>2</sub> (under the flow rates of 24 and 8 sccm, respectively) for 30 minutes at ~460 mT ambient pressure, and (3) cooling of the furnace at ~10°C/minutes under H<sub>2</sub> flow at 90 mT pressure. Formation of different layers of graphene was confirmed using HRTEM (as shown in figure 2.17(b)) and Raman spectroscopy, though the predominant area was found to be



covered with monolayer graphene.

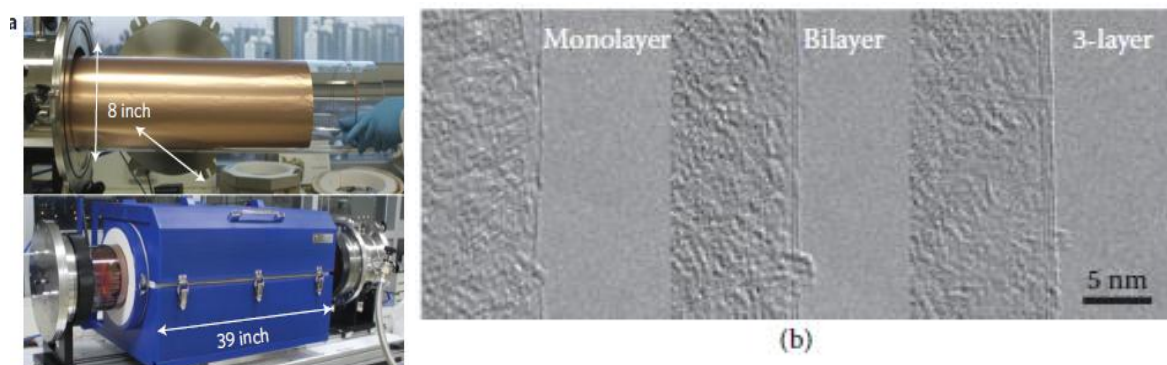


Figure 2-17 (a) Large-scale CVD of graphene on Cu foil; and (b) HRTEM images demonstrating the growth of single-layer, two-layer, and three-layer graphene on Cu.

Graphene growth directly onto any insulator substrate was first reported in 2010 [Ismach et al. 2010]. In this process, they deposited Cu thin film on dielectric substrates by e-beam evaporation and then using thermal CVD, they grew graphene at 1000°C under 100–500 mT ambient pressure. Graphene precipitation on dielectric surfaces occurs due to the surface catalyzed process of Cu and the copper films de-wetted and evaporated from the surface, which leads to direct graphene deposition on dielectric substrates as shown in figure 2.18. Further, the CVD process leads to the formation of well-crystallized graphene on the dielectric surfaces that contain low defects and exhibit thicknesses of 0.8–1 nm corresponding to 1- to 2-layer graphene.

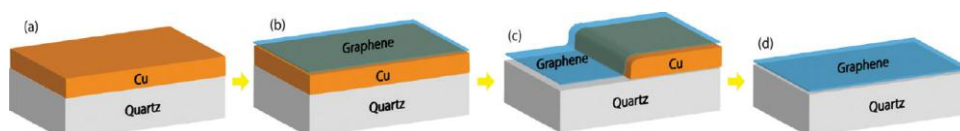


Figure 2-18 Schematic illustration of the CVD graphene formation mechanism on a direct dielectric substrate.

Therefore, direct synthesis of graphene on dielectric substrates bypasses the post synthesis graphene transfer process, hence avoiding the inclusion of defects and contamination in graphene. Furthermore, low-temperature graphene synthesis by CVD will be highly promising for easy device integration to reinstate present Si-based CMOS technology.

### 2.3.10 Plasma-Enhanced Chemical Vapor Deposition

When a thermal CVD process involves chemical reactions of the reacting gases by generating

plasma inside a vacuum chamber, which leads to the deposition of thin film on the substrate surface, the process is known as plasma-enhanced chemical vapor deposition (PECVD). By this technique, a process can be carried out at relatively low temperature compared to the other thermal CVD processes; hence, it is more feasible for industrial-scale applications. Moreover, catalyst-free graphene growth [Shang et al. 2008] can be carried out by controlling the process parameters, which normally influence the properties of the final graphene product. However, the process is costly and only gas-phase precursor materials can be used in order to obtain the final products, which limits its applications for synthesis of a wide range of industrial products.

### ***2.3.11 Epitaxial Growth of Graphene on SiC Surface***

Epitaxial thermal growth on a single crystalline silicon carbide (SiC) surface is one of the most acclaimed methods of graphene synthesis and has been explored vigorously for the last 7 to 8 years. The term *epitaxy* can be defined as a method that allows deposition of a single crystalline film on a single crystalline substrate. The deposited film is referred to as *epitaxial film* or the *epitaxial layer* over the single crystalline substrate and the process is known as *epitaxial growth*.

Epitaxial graphene growth is a process to fabricate high-crystalline graphene onto single-crystalline SiC substrates. When the film deposited on a substrate is of the same material it is known as a *homo-epitaxial layer*, and if the film and substrate are different materials it is called a *hetero-epitaxial layer*.

Investigations on the electronic properties of graphene have taken two directions. One direction is related to device fabrication based on exfoliated graphene on different substrates and the other is wafer-scale synthesis of epitaxial graphene, which is the most feasible and scalable approach to graphene-based electronics. Extensive conscientious research areas have been explored such as, (1) the electronic properties of graphene on SiC, (2) band gap formation, (3) graphene growth mechanism, and (4) graphene–SiC interfaces, focusing on pathways toward large-scale graphene based electronics.

## ***2.4 Graphene Growth Mechanism***

At present, the CVD process is one of the major graphene fabrication processes, which involves carbon deposition on the transition metal surface by decomposition of hydrocarbon gases at an elevated temperature under low or ambient pressure. In the thermal CVD process, at high temperature, hydrocarbon gases are decomposed by reacting with hydrogen, which leads to the formation of carbon atoms; when deposited on the metal surface, these carbon atoms segregate and form single- or few-layer graphitic sheets called *graphene*. In the PECVD process, the decomposition reaction occurs in the presence of plasma and carbon deposition, and segregation takes place at a comparatively low substrate temperature. Therefore, PECVD is known as a lower-temperature process than conventional thermal CVD. Further, the rate of decomposition reaction is solely dependent upon the power of the plasma source and the rate of carbon ion deposition on the substrate. However, both processes have several common parameters like time, temperature, pressure, gas flow rates, and type of catalyst, which play important roles in graphene formation. Graphene segregation on Ni is also dependent upon the post deposition cooling rate of the process as shown in figure 2.19, which tailors the morphology as well as the final properties of the graphene.

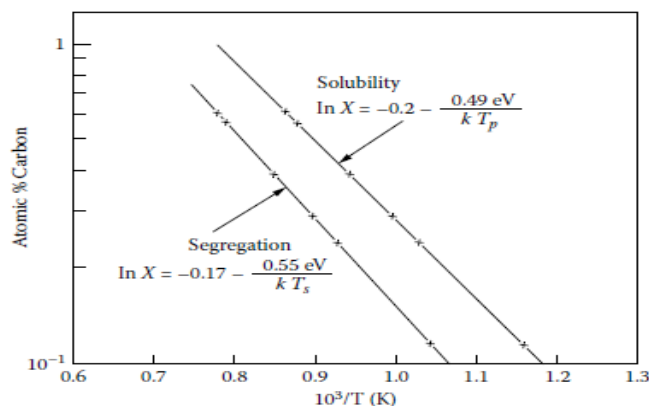


Figure 2-19 Solubility curve of C in Ni.

## 2.5 Large-Area Production of Graphene Thin Films and Transfer Methods

Many experts believe that graphene with a 2D film format, in contrast to 1D format carbon nanotubes, offers fabrication methods that are compatible with a batch micro-fabrication process, which is essential to realizing practical devices or systems. As a result, graphene is particularly suitable for unusual format electronic systems such as flexible, conformal, and stretchable electronic devices with demanding high mechanical requirements. In particular,

graphene has a molecular structure basically similar to that of organic electronic materials, and the strong interaction between graphene and organic materials could result in excellent interface contact.

### ***2.5.1 Large-Area Graphene Synthesis***

The most attractive technique for growing large-area graphene is chemical vapor deposition (CVD) on Ni or Cu substrate. In the CVD method, the hydrocarbon gas precursor is injected into a chamber at high temperature, around 1000°C. At a high temperature, hydrocarbon atoms are adsorbed on the catalyst layer and leave carbon atoms. In the cooling process, the carbon atoms get the energy to form a 2-dimensional atomic structure [Bae, S. et al. 2010, Kim, K.S. et al. 2009, Reina, A. et al. 2008, Lee, Y. et al. 2010]. Figure 2.20(a) shows a scanning electron microscope (SEM) image of few-layer graphene indicating various numbers of graphene layers grown on a Ni catalyst layer. The number of graphene layers is estimated by transmission electron microscope (TEM) in figure 2.20(b). The number of graphene layers depends on the solubility of carbon atoms in Ni catalyst grain [Kim, K.S. et al. 2009, Reina, A. et al. 2008].

The Ni grain, which has many carbon atoms, results in thick graphene film. To avoid graphite crystal, the amount of carbon source absorbed into the Ni should be reduced by controlling the thickness of Ni and the reaction time in high temperature. The distribution of graphene layers is shown in figures 2.20(c) and 2.20(d). After transferring the graphene film onto a SiO<sub>2</sub> (300 nm)/Si substrate, the optical and confocal scanning Raman microscopic images are observed. The brightest area in figure 2.20(d) corresponds to monolayer, and the darkest area represents thickness of more than ten layers of graphene. The Raman spectroscopy data (figure 2.20(e)) shows the characterization of number of graphene and their quality. All spectroscopic data show less intense D-band peaks, which indicate low defect density. The relative peak ratio in G/2D shows the number of graphene layers at the measuring point marked in figure 2.20(c).

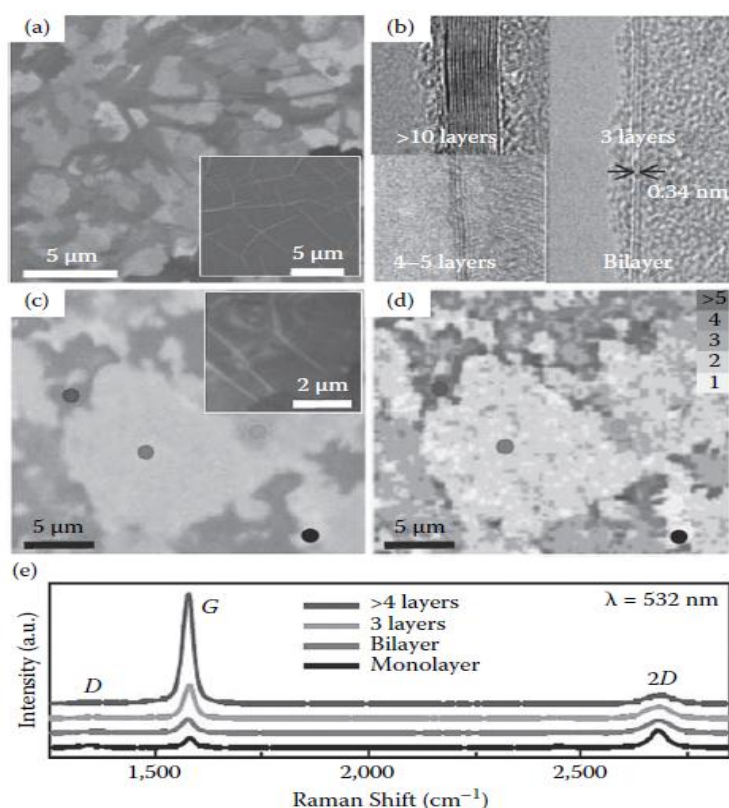


Figure 2-20 Graphene film synthesized on a nickel catalyst layer using the CVD method. (a) SEM image of graphene film grown on nickel layer. (b) Thickness and interlayer distance of graphene film estimated by HRTEM. (c) Optical microscope image of transferred graphene film on SiO<sub>2</sub> 300-nm layer. (d) Confocal scanning Raman image corresponding to (c). (e) Raman spectroscopy of each point indicating different number of layers.

### 2.5.2 Transfer Mechanisms

Two methods for transferring multilayered graphene grown on a Ni layer have been introduced in the literature.

The first method involves the application of a polydimethylsiloxane (PDMS) or polymethylmethacrylate (PMMA) supporting layer to graphene film while the catalyst layer is being etched. After stamping the graphene onto useful substrates, the supporting layer on graphene film is removed [Lee, Y. et al. 2010, Li, X. et al. 2009].

The second method is to transfer graphene film without any supporting layer during the etching and cleaning process. Through this method we can obtain a clean surface, even though the graphene film can be easily broken during the process.

The monolayer graphene film could be synthesized by using a Cu catalyst layer with a similar CVD growing procedure, mentioned previously. Because the evaporation of Cu occurs at a

relatively low temperature, thick Cu foil is used for CVD growth at 1000°C. The vacuum process results in low accumulation of amorphous carbon on the Cu surface. Figures 2.21(a) and (c) show SEM and optical microscope images of graphene film synthesized on Cu film. These images show a uniform distribution of monolayer graphene. The dark parts pointed by circles in the upside of Figure 2.21(a) and (c) represent bi-layered graphene and the arrows in the underside of Figure 2.21(a) and (c) indicate tri-layered graphene film. The surface morphology of graphene film strongly depends on the topography of the Cu surface. The Raman spectra from bottom to top in Figure 2.21(d) are from the marked places in Figure 2.21(a) and (c) the middle circle, upside circle and underside arrow, respectively. The uniformity of the graphene films are evaluated via color contrast under optical microscope and Raman spectra. An analysis of the intensity of the optical image over the whole sample and corresponding Raman spectra shows the monolayer graphene distributed more than 95% of the Cu surface [Li, X. et al. 2009, Ferrari, A.C. et al. 2006, Hass, J. et al. 2008].

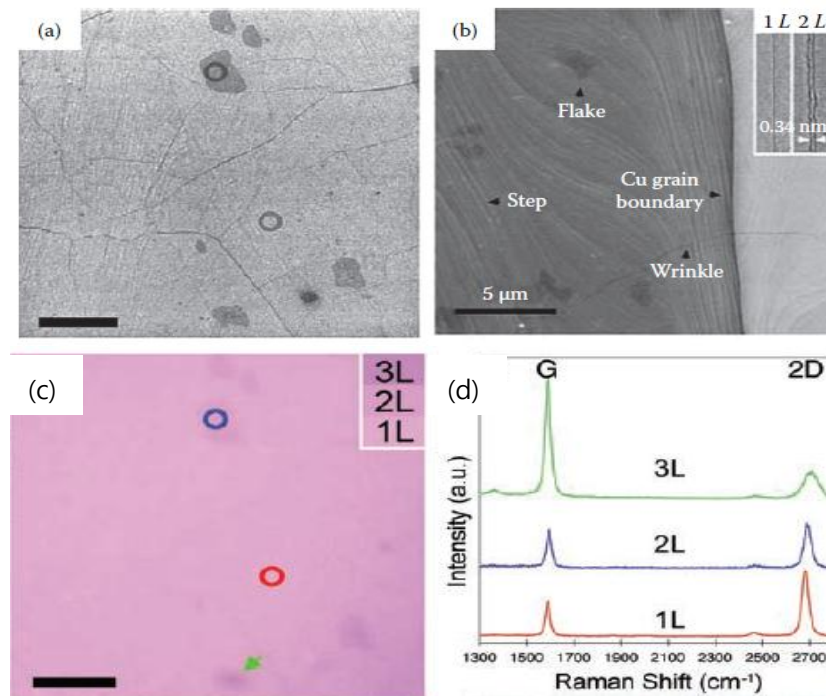


Figure 2-21 (See color insert.) Graphene film synthesized on a copper catalyst layer using the CVD method. (a) SEM image of graphene film grown on copper foil. (b) Morphological image of graphene film flowing copper surface conditions (inset denotes the monolayer and bilayer graphene estimated by TEM). (c) Optical microscope image of the graphene film transferred on SiO<sub>2</sub> layer showing different color indicating different number of layers. (d) Raman spectroscopy for each number of graphene layers on SiO<sub>2</sub> 300-nm layer.

### 2.5.3 Large-Area Graphene Transfer Methods

Large-area, high-quality graphene production has been achieved by epitaxial growth on a silicon carbide (SiC) substrate and CVD on a metal surface of Cu and Ni. However, most

applications require graphene to be located on an insulator. This means that graphene must be transferred to another appropriate substrate or processed in some other way if graphene is synthesized on a metal. The important thing is to transfer the graphene without significant deformation during the process. It is a challenge to transfer large-area graphene film to a target substrate without further degradation.

The schematic illustration of the wafer-scale graphene transfer process is presented in figure 2.22 [Lee, Y. et al. 2010]. The graphene grown on a Ni catalyst layer in wafer requires effective removal of the catalyst layer. Here, the detaching of graphene film and catalyst layer from the SiO<sub>2</sub>/Si mother substrate is introduced by using the wettability difference between the catalyst layer and SiO<sub>2</sub>. Then the catalyst layer can be removed instantaneously because a few-nm-scale catalyst layer is exposed to etchant.

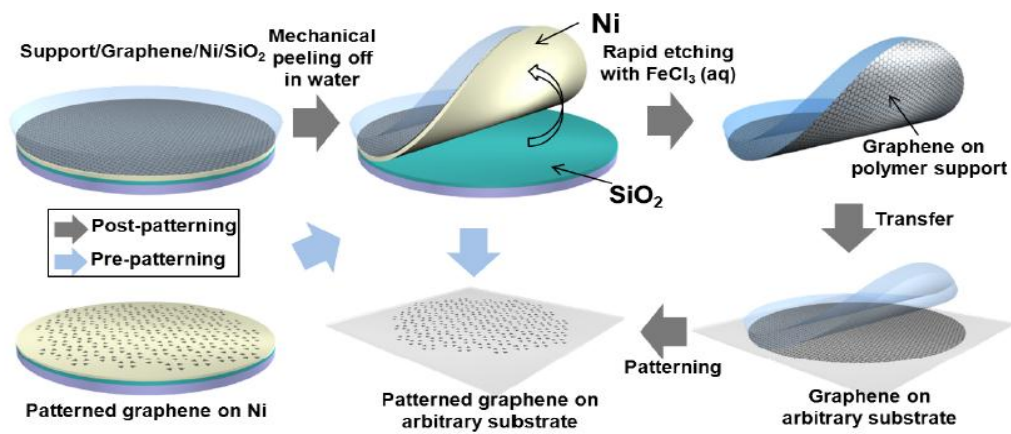


Figure 2-22 Schematic illustration of large-area graphene transfer process. Transfer process of both neat graphene film and patterned graphene film onto target substrate in a wafer scale through dry transfer printing with a polymer support layer.

The graphene attached to a polymer support is then state ready to transfer onto a useful substrate. After the graphene film is transferred onto target substrates, they can be patterned by photolithography with short oxygen plasma etching. Pre-patterned graphene film can be transferred through this method as well.

Another transfer printing method has been successfully developed using PMMA to aid the transfer of graphene grown on Cu foil to a target substrate [Reina, A. et al. 2008, Li, X. et al. 2009]. After graphene is grown on Cu foil, PMMA is spin coated on the top and baked for a short period of time. The Cu foil is then etched away and the remaining PMMA– graphene film is washed in deionized water to remove the etchant residue. At this stage, PMMA– graphene thin film is ready to transfer to an arbitrary substrate before removing the PMMA

using acetone. To minimize the density of cracks caused during the transfer process, an improved transfer process for the preparation of large area graphene films is explored [Li, X. et al. 2009], as shown in figure 2.23(a).

The procedures for transferring graphene from a SiC growth wafer to another substrate [Unarunotai, S. et al. 2010, Unarunotai, S. et al. 2009], as depicted in figure 2.23 (b), is similar to those reported for the transfer of random networks and the alignment of single-walled carbon nanotubes [Kang, S.J. et al. 2007]. In the first, the graphene–SiC sample is deposited with a layer of Au (or Pd) and polyimide. The baked polyimide thin layer serves as a strong support for the mechanical peeling process. After transfer to the target substrate, the polyimide and Au are removed by oxygen plasma reactive ion and wet chemical etching.

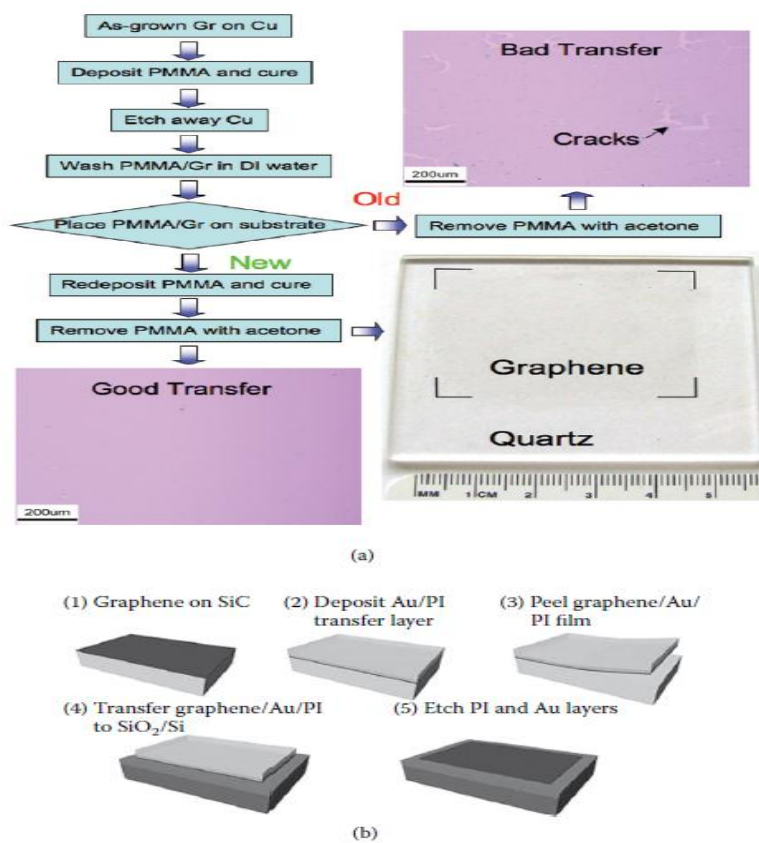


Figure 2-23 (a) Processes for transfer of graphene films. The two insets on the right are the optical micrographs of graphene transferred on SiO<sub>2</sub>/Si wafers (285-nm-thick SiO<sub>2</sub> layer) with “bad” (top) and “good” (bottom) transfer, respectively (b) Schematic illustration of the steps for transferring graphene grown on a SiC wafer to another substrate (SiO<sub>2</sub>/Si in this case).

A large-scale (30-inch) roll-to-roll transfer method has been developed recently [Bae, S. et al. 2010]. Figure 2.24 shows a schematic of the roll-based production of graphene films. This roll-to-roll method can enable the continuous production of graphene films in large scale. The first step is the adhesion of thermal release tape on graphene film grown on Cu foil using the



roll process. Next, Cu foil is etched in a bath filled with copper etchant and rinsed in deionized water to remove residual etchant. In the final step, the graphene film on the thermal release tape is roll-transferred onto a desired substrate by exposure to the release temperature of thermal release tape. Wet chemical doping, which considerably enhances the electrical properties of graphene films grown on roll-type Cu substrates by chemical vapor deposition, can be carried out using a setup similar to etching. The repetition of this process results in randomly stacked graphene.

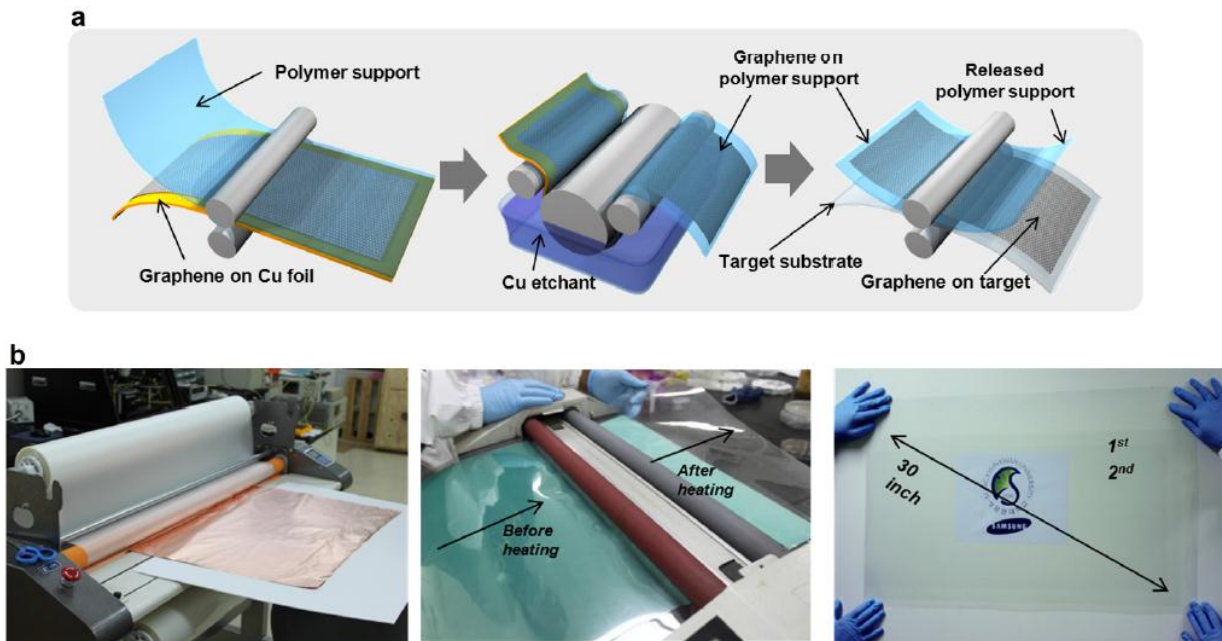


Figure 2-24 Schematic illustration of large-area graphene transfer process. Roll-to-roll transfer of graphene grown on copper foil with thermal release tape.

### 3. Electrohydrodynamic Atomization (EHDA) Deposition Technique

In electrohydrodynamic atomization deposition, the liquid is pulled out of the nozzle rather than pushed out as in the case of conventional inkjet systems. When the liquid is supplied to nozzle without applying the electric field, a hemispherical meniscus is formed at the nozzle tip due to the surface tension at the interface between the liquid and air. When the electric field is applied between the liquid and the ground plate (located under the substrate), the ions with same polarity move and accumulate at surface of the meniscus. Due to ions accumulation, the Maxwell electrical stresses are induced by the Columbic repulsion between ions. The surface of the liquid meniscus is mainly subjected to surface tension  $\sigma_s$ , hydrostatic pressure  $\sigma_h$  and electrostatic pressure  $\sigma_e$ . If the liquid is considered to be a pure conductor, then the electric field will be perpendicular to the liquid surface and no tangential stress component will be acting on the liquid surface. The liquid bulk will be neutral and the free charges will be confined in a very thin layer. This situation can be summarized in the following equations.

$$\sigma_h + \sigma_e + \sigma_s \quad (3-1)$$

Since the liquid is not a perfect conductor, the resultant electric stress on the liquid meniscus has two components, i.e. normal and tangential as shown in figure1. This repulsion force (electrostatic force) when exceeds the certain limit deforms the hemispherical meniscus to a cone. This phenomenon is known as the cone-jet transition, which refers to the shape of meniscus [Poon 2002].

#### 3.1 Electrohydrodynamic Atomization Modes

The mode of electrohydrodynamic atomization is the way the liquid is dispersed into droplets, and is characterized by two criteria [Jaworek & Krupa 1999]:

1. The geometrical form of the liquid at the outlet of the capillary (drop, spindle, jet),
2. The mechanism of the disintegration of the jet into droplets (type of instability).

The spraying modes differ significantly in their geometrical form as observed in continuous

light. These differences result from the microstructure of the jet, its formation and disintegration into droplets. Usually, each mode commences suddenly at certain voltage and flow rate, and is sustained within a certain interval of their values. Then, it abruptly changes into another mode of spraying. The spraying modes differ significantly in their geometrical form as observed in continuous light. These differences result from the microstructure of the jet, its formation and disintegration into droplets. Usually, each mode commences suddenly at certain voltage and flow rate, and is sustained within a certain interval of their values. Then, it abruptly changes into another mode of spraying.

### ***3.1.1 Dripping mode***

The dripping mode of ESD does not differ significantly from the natural dripping i.e. when no applied to the capillary and only flow rate is given. The drops are formed as regular spheres detaching from the capillary as the weight of the drop and the electric force overcome the capillary forces. The exception is that with the voltage increasing the meniscus elongates and the drop becomes smaller.

The similarity extends also to the satellite droplets for liquids of low viscosity. However, for higher voltages, the drop is, for some time, connected with the capillary by a thread, which next breaks off to a few of smaller droplets. After detachment of the drop, the meniscus contracts back forming a hemispherical-like meniscus.

### ***3.1.2 Micro-dripping mode***

In micro-dripping mode, liquid at the outlet of a capillary forms a stable meniscus, at the end of which a small, much smaller than the capillary diameter, droplet is formed. The droplet detaches from the meniscus and no further disintegration takes place. The main difference between dripping mode and micro-dripping mode is that there is no meniscus formation after droplet generation and continuous drop generation depending upon the flow rate and applied voltage. For liquids of low viscosity, this filament breaks off under the electrostatic and inertial forces into smaller droplets. With viscous liquids the broken filament contracts both into meniscus and the detached droplet with no satellite droplets' emission. The size of the droplets can range from a few micrometers up to a few hundred of micrometers in diameters and the droplet size distribution is usually monodispersed. The frequency of the emission of the droplets ranges from a few up to a few thousands of droplets per second.

### ***3.1.3 Spindle mode***

In the spindle mode, the meniscus of liquid elongates in the direction of electric field as a thick jet and detaches as a vast spindle-like fragment of liquid. Because of the shape of the jet emitted, this mode is referred to as spindle mode. The spindles, after detachment can disintegrate into numerous smaller droplets of different sizes, hence resulting in poly-dispersed spraying. After the spindle detachment, the meniscus contracts to its initial shape and a new jet start to be formed. The spindle can be sometimes connected with the capillary by a thick thread several mm long. The thread is not linear in its form, but whips irregularly. In the case of low viscosity liquids (ethanol) also a single thin thread can be ejected from the leading side of the spindle, similar to the micro-dripping mode. This thread detaches from the main drop and next disrupts into several small fragments forming siblings or fine poly-dispersed aerosol. The spindle mode differs from the dripping mode in that no regular droplet is ejected from the meniscus but only elongated irregular fragments of liquid. Main droplets are usually different in size, with diameters varying in the range of 300 to 1000  $\mu\text{m}$  while satellite droplets of  $\sim 100 \mu\text{m}$ .

### ***3.1.4 Unstable cone-jet mode***

Just between the spindle mode and stable cone-jet mode, occurs the unstable cone-jet mode. This mode occurs when the applied voltage is not good enough to overcome the surface tension forces permanently, but is enough to overcome these forces temporarily. Hence the jet is not stable and we can have many instances of meniscus recoil. The temporary jet also breaks up and hence disintegrates into many smaller droplets.

### ***3.1.5 Cone-jet mode***

In the cone-jet mode, the liquid forms a regular, axisymmetric cone with a thin jet ( $< 100 \mu\text{m}$  in diameter) at its apex. According to Cloupeau and Prunet-Foch [Cloupeau & Prunet-Foch 1994] the cone can assume three different forms: with linear sides, convex or concave. The jet flows along the capillary axis or deflects from it only on small angle. The jet at its end undergoes varicose [Cloupeau & Prunet-Foch 1989] and kink [Jaworek & Krupa 1992] instabilities.

In the case of varicose instabilities, the waves are generated on the surface of the jet, but the

jet does not change its linear position. In the nodes of the wave the liquid contracts and the jet disintegrates into equal droplets, which further flow close to the capillary axis.

In the case of kink instabilities the whole jet moves irregularly off the axis of the capillary, with high amplitude and breaks up into series of fine droplets due to electrical and inertial forces. The aerosol is spread out off the axis, but nearly uniformly in the spray cone of an apex angle of 50-60°. Monodispersed droplets of mean diameter of about 30 µm or smaller are produced within this mode.

Variants of this mode are Oscillating-jet mode and Precession mode and are discussed in [Jaworek & Krupa 1999] in detail.

### ***3.1.6 Multi-jet mode***

The reason behind the occurrence of multi-jet mode, where the meniscus becomes flat with small cones at distinct points at the circumference of the capillary, from which fine jets of liquid are ejected, is still unknown. The diameter of the jets, in this mode, is smaller than a few of tens of micrometers. The jets disintegrate due to kink instabilities, into small droplets, forming a fine mist around the capillary. Near the capillary, the aerosol does not fill the whole spray volume but only is dispersed in a few narrow streams which seem to be located uniformly around the axis. The number of the emission points increases with the voltage increasing.

Apart from dripping mode, each mode of ESD produces atomization. However, the stable cone-jet mode is used for the thin film deposition [Muhammad et al. 2011, Choi et al. 2010, Samarasinghe et al. 2008] because of its mono-dispersed droplet production, very stable atomization process and smooth deposition. A real time depiction of ESD in stable cone-jet mode, as captured by a digital camera is produced in figure 3.1 below. A very stable and smooth spray stream is visible at the end of the nozzle thereby assuring a smooth and uniform film deposition.

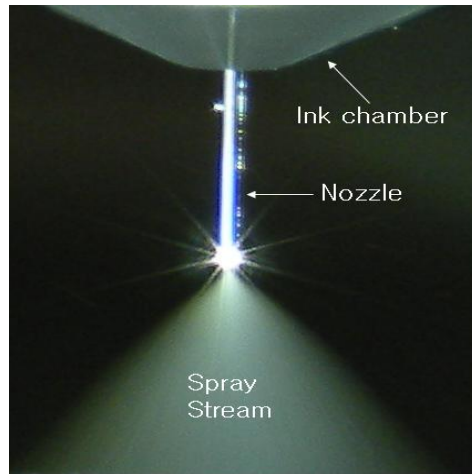


Figure 3-1 Real time photograph of the spray, emanating from the nozzle. A wide spray stream is clearly visible at the tip of the nozzle.

### ***3.2 Parameters Affecting the Cone-jet***

The parameters that influence the formation and transition of stable cone-jet mode can be divided in two groups. Operating parameters i.e. flow-rate, electric field and nozzle diameter, and liquid properties i.e. electric conductivity, viscosity and surface tension [Hartman 2006].

#### ***3.2.1 Flow-rate***

The flow-rate has a significant effect on the jet diameter and stability of the jet in cone-jet transition. It is the main parameters to control the jet diameter for the patterning process. The flow-rate also affects the applied potential requirement for development of cone-jet (operating envelop) and the resulting the shape of the cone-jet. In EHDA processing jetting, flow-rate also affect the stability of the jet, at low flow-rate the jet is stable, whereas the high flow-rate in cone-jet region destabilize the jet resulting in shorter jet length. This is due to amount of charge carrying at high flow-rate which destabilizes the jet. The typical effects of the flow-rate on stable cone-jet mode are shown in figure 3.

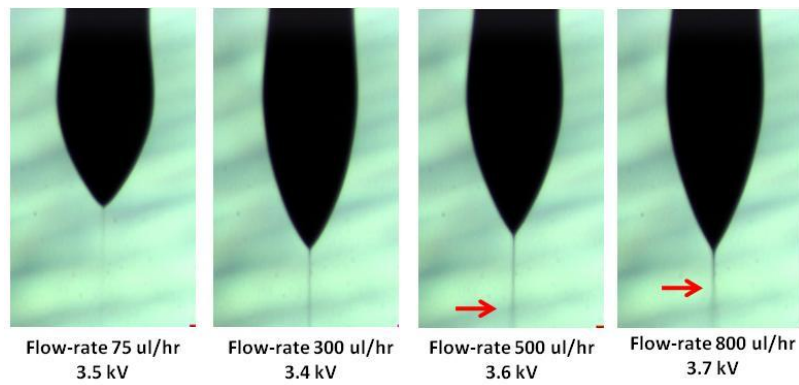


Figure 3-2 Effect of flow rate on the cone-jet transition. The jet diameter increases with increase in flow-rate. The red arrow indicates the jet break-up point.

### 3.2.2 Electric field (Applied voltage)

Electric field affects the morphology of the cone, by increasing the electric field strength in steady cone-jet mode, the cone-jet recedes towards the nozzle. However, there is less effect on the jet diameter by increasing the applied voltage. At relatively low flow-rate and high electric field, the jet disintegrated into mist of small droplets also known as electrohydrodynamic atomization, this behavior is used for the thin film deposition of functional material. The typical shape of the cone at different applied voltage is shown in figure 3.

### 3.2.3 Nozzle diameter

Nozzle diameter has significant influence on the operating envelope of the stable cone-jet region. Smaller nozzle diameters extend the lower and higher value of flow-rate limit. The voltage requirement for the cone-jet also decreases with decrease in nozzle diameter for any given liquid.

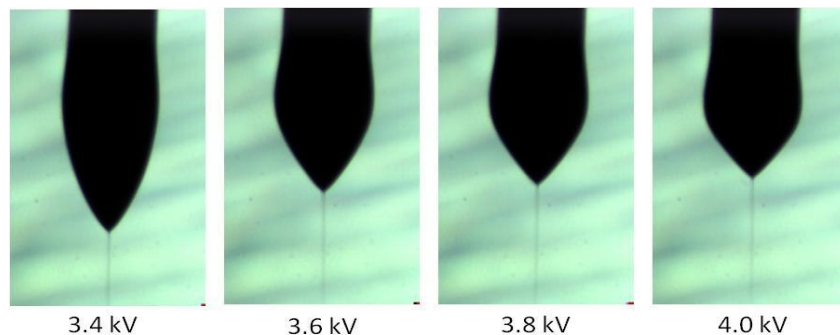


Figure 3-3 Effect of the applied voltage on shape of the cone-jet at constant flow rate (200 $\mu$ l/hr).

### ***3.2.4 Conductivity***

The liquid conductivity affects both the shape of the liquid cone and stability of the jet, due to the amount of electric charge on the liquid surface and jet produces is also very unstable because of high radial electric field. Highly conductive liquid deforms into sharp cone-jet shape. Liquid with very low conductivity do not deform into cone-jet by applying electric field, only dripping mode is observed. Liquids with intermediate conductivity range produce steady cone-jet.

### ***3.2.5 Surface Tension***

The formation of the jet occurs when the electrical forces overcome the surface tension at the apex of the meniscus. The required applied voltage will be increased with increase in surface tension of the liquid.

### ***3.2.6 Viscosity***

The role viscosity is in the stabilization of the jet and diameter of the jet produced. In high viscous liquid, the jet is stable for larger portion of the length but also produces the thicker diameter. This is due to charge mobility, which is reduced significantly in high viscosity liquid, and causes decrease in conductivity.

## ***3.3 ESD Experimental Setup***

The basic experimental setup for the deposition process consisted of following components, as described in the schematic diagram in Figure 3.4 and real time picture in Figure 3.5:

### ***3.3.1 Metallic nozzle (Harvard Apparatus)***

Responsible for spray ejection, made of high-quality stainless-steel with inner diameter of 310 $\mu$ m inner and 710  $\mu$ m outer diameter.



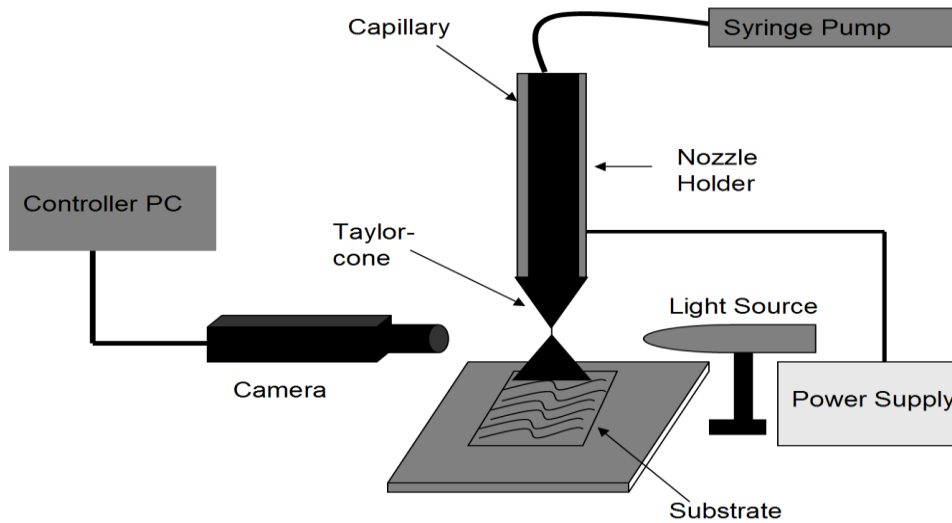


Figure 3-4 Schematic diagram of the system deposition system.

### 3.3.2 Syringe Pump (*Harvard Apparatus, PHD 2000 Infusion*)

Connected to the nozzle, the syringe pump maintains the minimum required flow rate for the spray ejection.

### 3.3.3 Power Source (*NanoNC*)

A high voltage power source connected between the capillary and copper plate ground electrode generates highly concentrated electric field at the capillary outlet and generates the largely mono-dispersed electrohydrodynamic atomization of the nano-particles.

### 3.3.4 Camera (*MotionPro X*)

A high resolution CCD camera is connected to the main computer and is responsible for the high speed, high resolution capturing of the events going on at the capillary tip i.e. dripping and Taylor- cone formation etc.

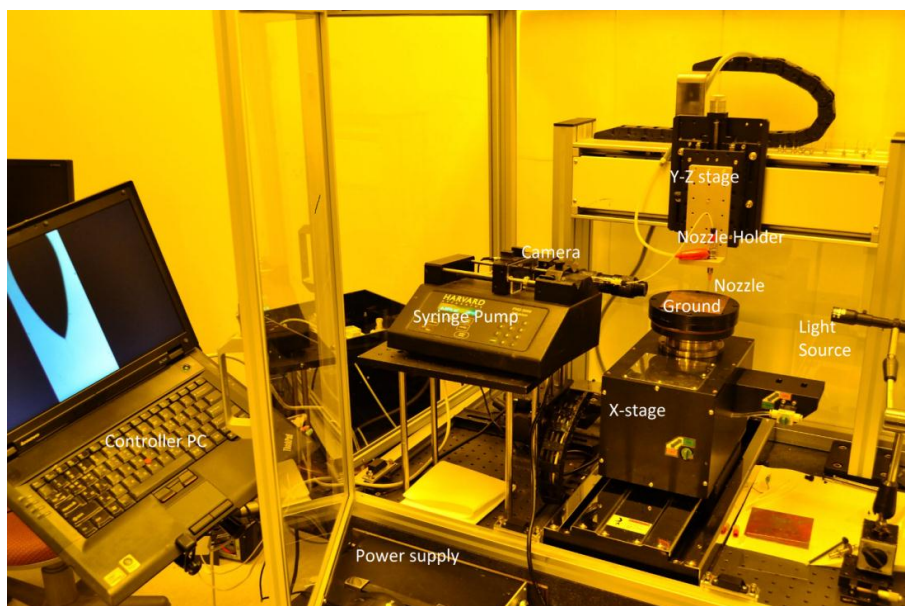


Figure 3-5 Real-time photograph of the deposition system.

### ***3.3.5 Miscellaneous Equipment***

Teflon tubing is used for the solution supply from the syringe to the nozzle. Metallic nozzle is mounted on an independent plunk capable of moving in the y and z-direction (vertical and lateral) while the copper plate electrode holding the glass substrate, is attached to the stage which is capable of moving in x direction (linear direction).

## 4. Deposition of Graphene flakes and its composites by using EHDA Technique

The novelty of graphene electronic properties has been well attributed now. Graphene suffers a problem of mass production which is common to many new materials. Several synthesis routes have been exercised to produce single layer, bi-layer and few layer graphene. As discussed in chapter 2, earlier the standard procedure used to produce graphene was micromechanical cleavage. However, the single layers so produced, form a negligible fraction amongst large quantities of thin graphite flakes. Alternatively, growth of graphene is also commonly achieved by annealing SiC substrates; however, these samples are in fact composed of a huge amount of domains, most of them sub micro-meter in scale, and they are not spatially uniform in number or size over larger length scales. Later on CVD processes were used for large area fabrication on Ni and Cu substrate using controlled environment, but this would require transfer of the sample to insulating substrates in order to make useful devices, either by mechanical transfer or through solution processing. In this chapter, direct deposition of graphene flakes thin film and composite graphene/ZnO thin film to functional substrate from dispersion by using EHDA technique is briefly discussed.

### 4.1 Graphene Flakes Deposition

To make graphene flakes deposition fast and avoid vacuum processing, electrohydrodynamic atomization (EHDA) has been employed here. This process has the potential of becoming a reliable, cost effective and robust route for graphene flakes film.

This work has been published in Journal of Materials Science: Materials in Electronics [K.H. Choi et al. 2013]. A comprehensive description of graphene flakes film fabrication is described here i.e. direct deposition of exfoliated graphene flakes from solution on to substrate by using Electrohydrodynamic Atomization (EHDA) process. For EHDA, graphene flakes dispersion is synthesized and its physical properties are measured to determine processing parameters. The graphene film deposited by using EHDA process is cured at 200°C for 1hours. After curing, randomly oriented graphene flakes film has been characterized by using FE-SEM, UV-Vis-NIR spectroscopy, X-ray diffraction (XRD), Raman Spectroscopy and 3D-Nanomap. Electrical behavior of the film is investigated by depositing

graphene as cathode onto F8BT in diode device i.e. ITO/PEDOT: PSS/F8BT/Graphene.

#### ***4.1.1 Synthesis of Graphene Dispersion***

Graphite powder and N-methyl-pyrrolidone (NMP) solvent were purchased from Sigma Aldrich. The graphite powder (0.02 g) was dispersed in NMP (8ml) solvent. The solution was then bath sonicated for 30 minutes at room temperature. After sonication, vacuum filtration was done to remove large un-exfoliated graphite flakes. For further purification, filtrate was subjected to centrifugation. It was carried out for 30 minutes at 3000 rpm. Supernatant was separated from sediment. The viscosity of the ink was measured to be 15.8 mPa by using Viscometer VM-10A system. The surface tension of the ink was measured to be 57~59 mN/m by using Surface-electro-optics (SEO)'s contact angle analyzer. The electrical conductivity of the ink was 12.2 $\mu$ S/cm, measured by using conductivity meter (Cond6+ meter).

#### ***4.1.2 Graphene Flakes Film Deposition***

A schematic diagram of the setup is shown in the figure 4.1. For processing, the ink is placed in an ink chamber (Nano NC Nozzle adapter) through a syringe pump (Hamilton, Model 1001 GASTIGHT syringe), and a constant flow rate is provided through the syringe pump. A metal nozzle of 110  $\mu$ m internal diameter [Havard 33G] is used as the anode, and it is connected to a Trek Model 610E high voltage source for the generation of the required electric field. Ground is provided by connecting the ground terminal of the power source to a moving stage that holds the substrate. A high-speed camera, along with a light source, is used in conjunction with a portable computer to capture images of the events taking place at the capillary's orifice. Before the graphene deposition, silicon substrate is cleaned with acetone for 1 minutes using ultra-sonication and then dried. The flow rate with a combination of varying potentials is used in order to observe atomization modes. The speed of moving stage is kept at 5 mm/sec. Deposition parameters for covering (2 $\times$ 2) cm<sup>2</sup> silicon wafer are given in figure 4.1.

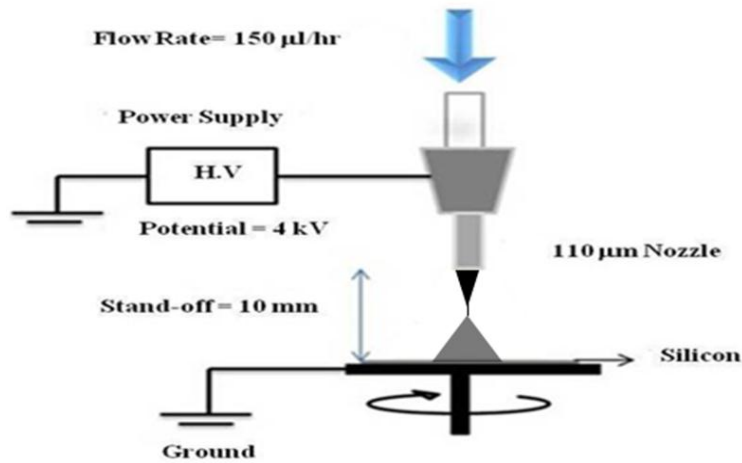


Figure 4-1 Schematic diagram of the experimental setup.

#### 4.1.3 Taylor cone and Atomization modes

Graphene flakes dispersion was remained stable during the experiments and no sedimentation was observed at any point. The EHDA experiments were initially performed with flow rates using from 50 μl/h to 1000 μl/h in order to determine the optimum spraying conditions with the stand-off distance fixed at 10 mm. At each flow rate, the strength of the electric field was increased by gradually increasing the potential difference between the anode nozzle and the grounded stage [A. Jaworek et al. 2008, K.H. Choi et al. 2012]. At each flow rate step, applying different magnitude of voltages showed different atomization modes such as the dripping to the multi-jet. Figure 4.2 represents high-resolution and high-speed images of different atomization modes captured at 150 μl/h flow rate for increase in applied voltages.

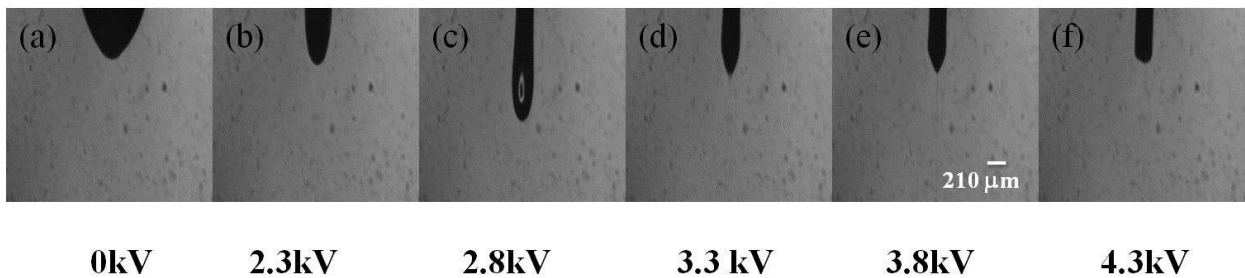


Figure 4-2 Electrohydrodynamic modes of graphene ink observed during the deposition process, a) Stable meniscus b) dripping, c) micro-dripping, d) pulsating unstable cone-jet, e) stable cone-jet, f) Multi-jet.

Figure 4.3 provides the observed operating envelop of the graphene flakes dispersion for EHDA. A stable cone-jet region is shaded in operating envelop to emphasize the possible flow rate and voltage combinations. For film deposition, a flow rate of 150 μl/hr was used throughout the experiments.

The occurrence of the classical hydrodynamic atomization requires the hydrodynamic relaxation time  $T_h$  to exceed the charge relaxation time  $T_q$  [K. Rahman et al. 2011]. The two quantities are given as:

$$T_h = LD^2/Q \quad (1)$$

$$T_q = \epsilon_0 \epsilon_r / K \quad (2)$$

Here,  $L$  denotes the axial length of the jet,  $D$  is the jet diameter,  $Q$  is the flow rate and  $K$  is the electrical conductivity. Using the following values for these quantities,

$$L \approx 800 \mu\text{m}$$

$$D \approx 10 \mu\text{m}$$

$$Q = 150 \mu\text{l/hr} = 4.1667 \times 10^{-11} \text{m}^3 \text{s}^{-1}$$

$$\epsilon_r = 2.3$$

$$\epsilon_0 = 8.85 \times 10^{-12} \text{Fm}^{-1}$$

$$K = 0.0000122 \text{Sm}^{-1}$$

It implies that  $T_h \approx 0.00192 \text{ s}$  which is much greater than  $T_q \approx 1.67 \times 10^{-6} \text{ s}$ . Thus, the required condition for classical electrohydrodynamic atomization is being fulfilled.

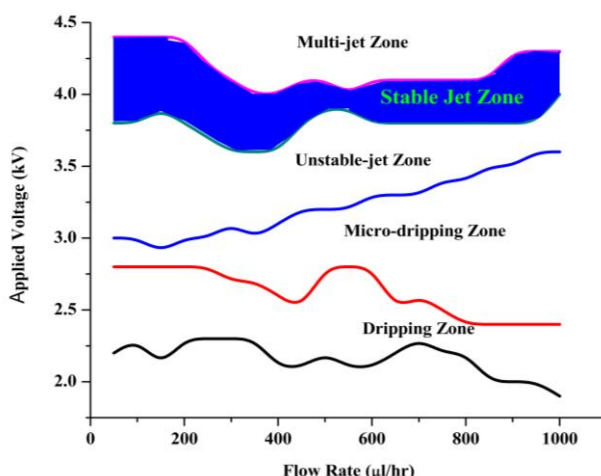


Figure 4-3 Operating envelop for different EHDA zones. The stable cone jet region is shaded to emphasize upon the possible flow rate and voltage combinations for optimized atomization conditions (stand-off= 10mm).

#### 4.1.4 Optical Microscopy

Figure 4.4 (a-b) shows optical images of graphene flakes film deposited onto silicon substrate. It is observed that by using EHDA for deposition, the graphene flakes are randomly oriented on substrate due to which surface morphology of the film is non-uniform. In next section, SEM analysis of the film has further confirmed it.

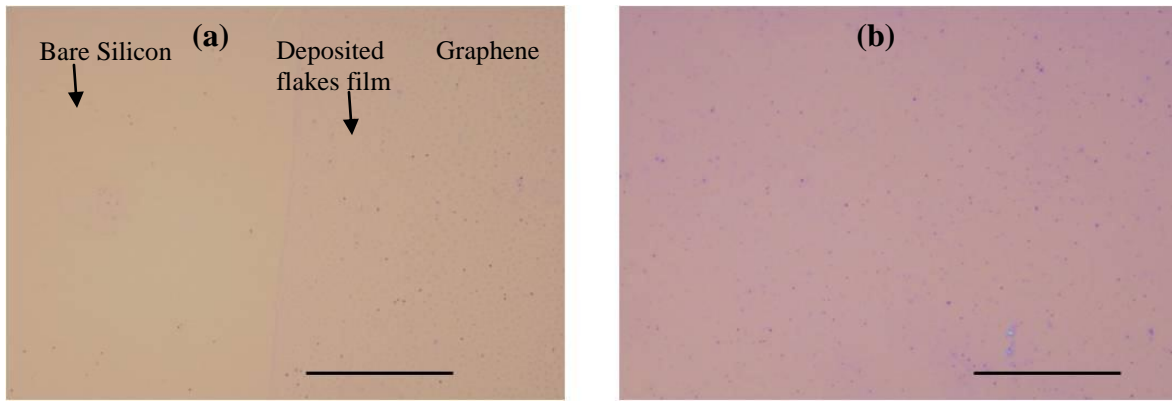


Figure 4-4 Optical Microscopic images of the deposited graphene flakes film (Scale bar is 50  $\mu\text{m}$ ).

#### 4.1.5 SEM Analysis

Figure 4.5 (a-e) shows the SEM images of the film taken at different resolutions i.e. from low to high resolutions. It is observed that the surface morphology of the deposited film is not uniform throughout. High resolution images have confirmed randomly oriented deposited graphene flakes, which has resulted in non-uniform surface morphology of the film.

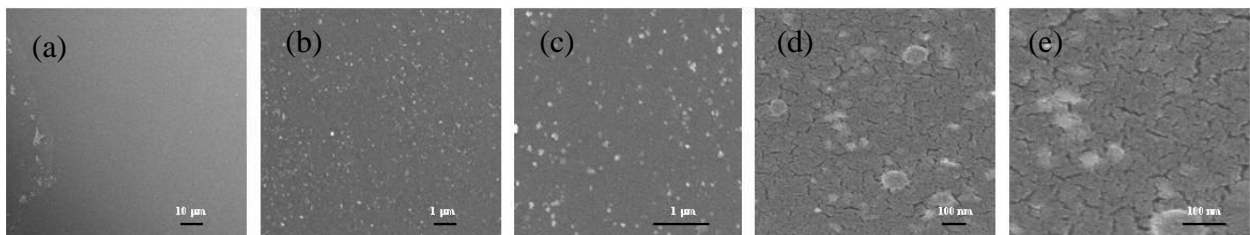


Figure 4-5 (a-c) Low magnification SEM surface view of the deposited films of graphene using deposition speed 5 mm/sec. (d-e) High magnification SEM micrographs showing surface characteristics and very high magnification showing grain size.

#### 4.1.6 3D Nanomap

The 3D surface profile, 2D surface profile and the X-profile of the graphene film deposited on Si substrates is shown in figure 4.6. It shows that its Ra value is 1.28 nm. X-profile of the film reflects that the film surface has many nano-level bumps (peak to valley), which means that graphene film deposited by using EHDA process has different number of graphene layers i.e. single layer, bilayer, few layer and multilayer morphology i.e. supports the random orientation deposited graphene flakes onto the substrate.

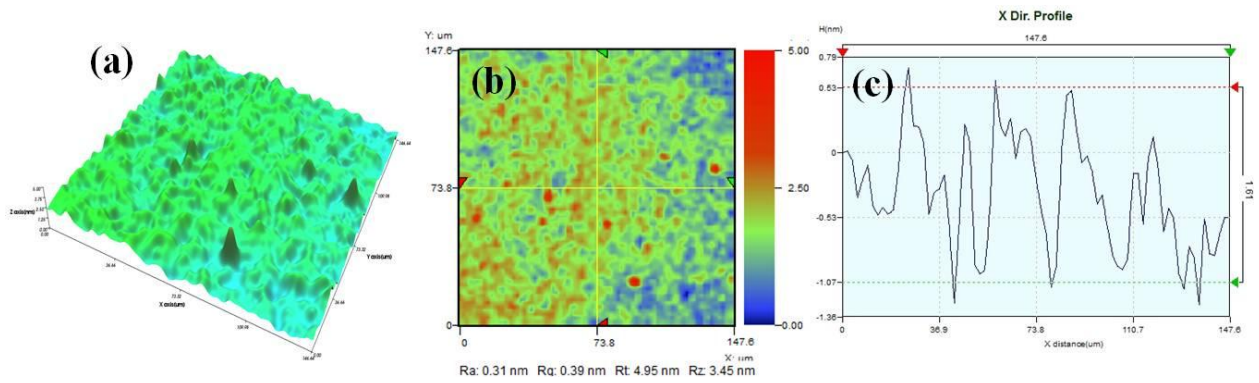


Figure 4-6 (a) 3D surface profile, (b) 2D surface profile and (c) X- profile of the graphene film deposited on Si substrate.

A depiction of randomly oriented graphene flakes before and after deposition has been shown in figure 4.7.

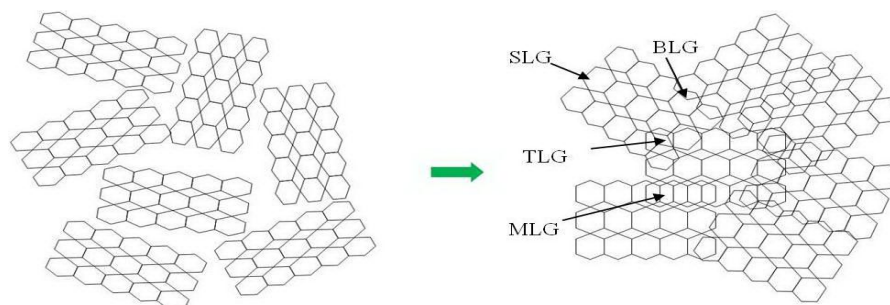


Figure 4-7 Schematic depiction of the graphene fragments in dispersed form and after deposition on substrate.

#### 4.1.7 X-ray Diffraction Analysis

The crystal structure and crystalline size of the deposited graphene flakes film is determined by Rigaku X-ray diffraction (XRD) operated at 36 kV and 36 mA with Cu K $\alpha$  radiation in the range of 10 $^\circ$ - 65 $^\circ$  with a step of 0.02 $^\circ$ . Figure 4.8 shows XRD profile of deposited graphene flakes film, two broad peaks at  $2\theta = 24.7^\circ$  and  $2\theta = 42.3^\circ$  are observed with an interlayer spacing of 37 Å and 39 Å which are assigned to graphene (002) and (100) plane, respectively. In the XRD pattern of graphene, a typical diffraction peak is broadened which indicates smaller crystalline size of graphene. The calculated d-spacing, suggesting that the distance between graphene layers is close to the theoretical value 0.34 nm [J. Liu et al. 2010]. The crystallite size of graphene is 2.1nm which is calculated by Scherer equation by using XRD radiation of wavelength  $\lambda$  (nm) and measuring full width at half maximum of peaks ( $\beta$ ) in radian located at any  $2\theta = 24.7^\circ$  in the pattern.



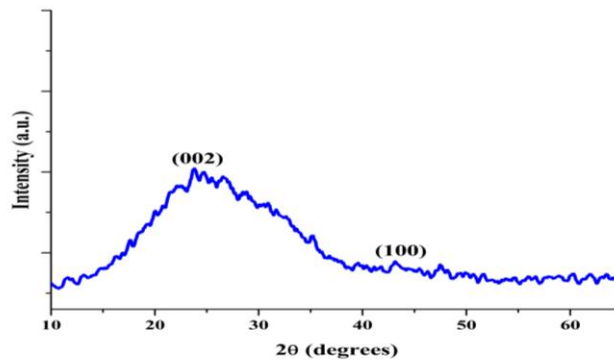


Figure 4-8 XRD patterns of the graphene flakes film.

#### 4.1.8 Raman Spectra Analysis

Raman spectroscopy of the deposited graphene flakes film is carried out by using the LabRam HR800 micro Raman spectroscope (Horiba Jobin-Yvon, France). The Raman system is operated at the 10mW laser power and an excitation wavelength of 514 nm with Ar<sup>+</sup> ion laser. Figure 4.9 shows the Raman Spectrum of the deposited graphene flakes film on silicon substrate. The major features, commonly observed in all chemically processed graphene are D band at 1354 cm<sup>-1</sup>, G band at 1580 cm<sup>-1</sup> and 2D band at 2725 cm<sup>-1</sup>. The G band at 1580 cm<sup>-1</sup> corresponds to an E<sub>2g</sub> mode which is related to the sp<sup>2</sup>-bonded carbon atoms vibration in a 2D hexagonal lattice. And the D band at 1354 cm<sup>-1</sup> arises from a breathing mode of k-point phonons of A<sub>1g</sub> symmetry. The high intensity of D band indicates the presence of sp<sup>2</sup> C with defects.

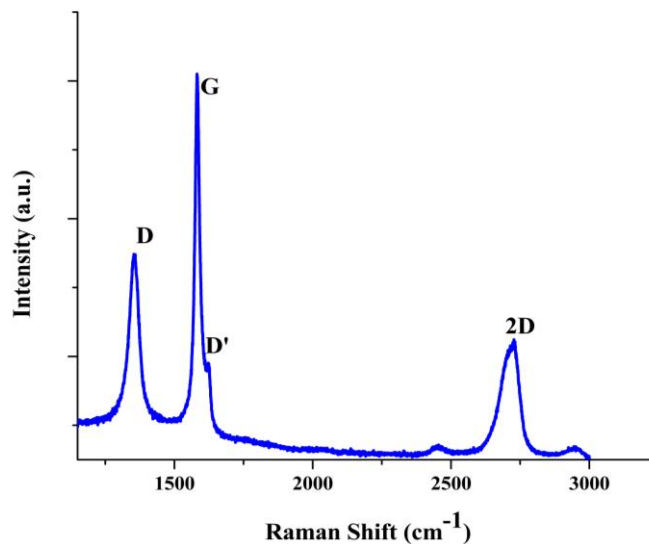


Figure 4-9 Raman spectra of the deposited graphene flakes film.

The in-plane size of the crystallites is deduced from the intensities ratio between the G and D band integrated intensities ( $I_D/I_G$ ). Using the expression given by Pimenta et al. [Pimenta MA

et al. 2007]

$$L_a \text{ (nm)} = 560 / (E_l^4 (I_D/I_G)) \quad (3)$$

where  $E_{l(\text{laser energy})} = 3.86 \text{ eV}$  and  $I_D/I_G = 0.8$ , therefore the in plane graphene crystallite is 3nm.

#### 4.1.9 UV/Vis/NIR Analysis

Figure 4.10 shows the transmittance spectra of EHDA the deposited graphene flakes film in ultra-violet (UV), visible and near-infra-red (NIR) spectrum. The transparency of the film is recorded by a UV/Vis/NIR spectrometer (Shimadzu UV-3150) with a range of 200–800 nm. Transmittance of the deposited thin film is observed 92–93 % in the visible range. This percentage transmittance is in accordance to our schematic interpretation of Raman Spectroscopy of graphene film. The transmittance spectrum reveals that the graphene film is more suitable for optoelectronic device applications. For band gap calculation, an absorbance spectrum of the film is taken. The optical band gap of graphene is estimated by fundamental relation given by equation  $\alpha h\nu = B(h\nu - E_g)^n$ , where  $\alpha$  is the absorption coefficient,  $h\nu$  is the energy of absorbed light,  $n = 1$ , for direct allowed transition and  $B$  is proportionality constant [J.Tauc (Ed.) 1974]. Energy gap ( $E_g$ ) was obtained by plotting  $(\alpha h\nu)^2$  vs.  $h\nu$  and extrapolating the linear portion of  $(\alpha h\nu)^2$  vs.  $h\nu$  to zero, as shown in figure 4-10 (b). The bandgap of graphene was estimated to be 3.95 eV by using this method.

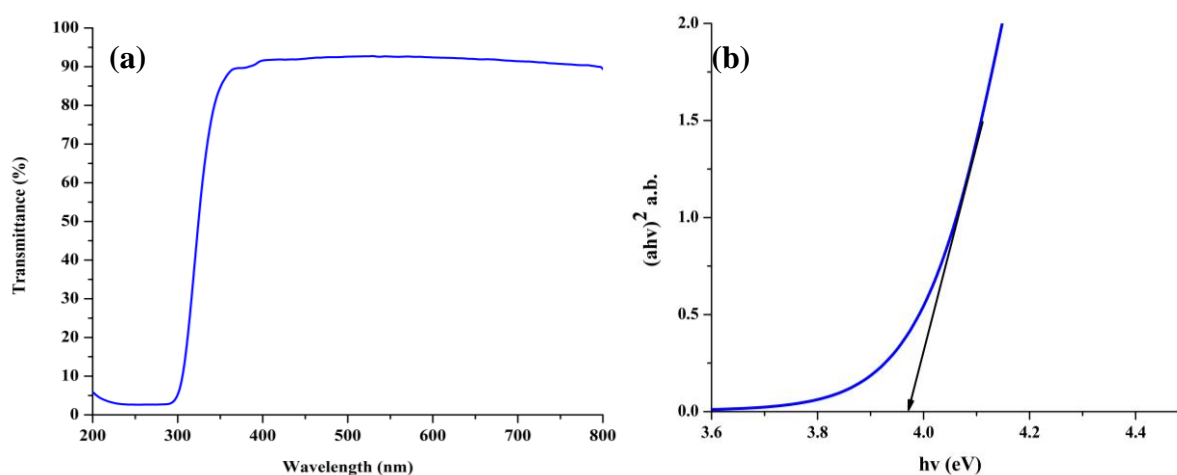


Figure 4-10(a) UV–vis spectrum of the graphene flakes film (b)  $(\alpha h\nu)^2$  vs.  $h\nu$  plot for bandgap estimation of graphene flakes film.

#### 4.1.10 Electrical Behavior Analysis

In electronic devices contact between two adjacent layers is very much important for adequate electrical behavior. Therefore, to analyze the deposited graphene flakes film electrical behavior, Agilent B1500A semiconductor device analyzer is used. The current density-voltage (J-V) curve of the organic diode device with structure ITO/PEDOT:PSS/F8BT/Graphene (schematic figure 4.11a) in linear scale recorded by semiconductor analyzer is shown in figure 4.11, in which graphene is used as cathode. The J-V plot confirms the proper contact between adjacent layers in diode device. At voltage of 0.3V, the current density in organic structure is at low value of  $2.67 \text{ A/cm}^2$  and after that as further voltage was applied, the device current increased by almost 100 times and reaches up to  $2.65 \times 10^2 \text{ A/cm}^2$  at voltage 4V which indicates an increase in charge carrier injection.

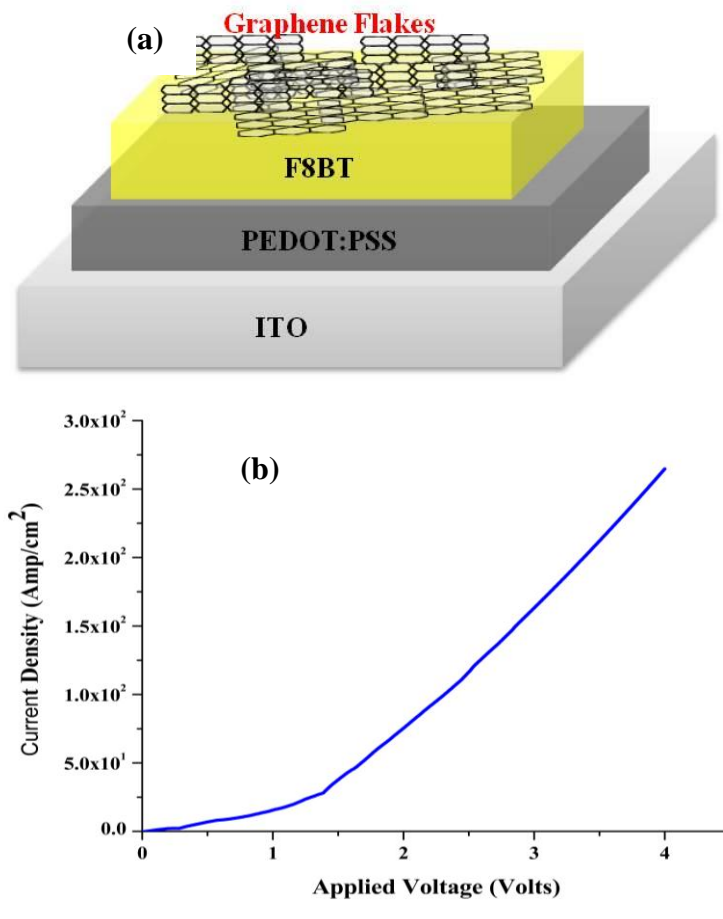


Figure 4-11 I-V characteristics of ITO/PEDOT-PSS/F8BT/Graphene diode.

For current conduction mechanism in diode device i.e. ITO/PEDOT: PSS/F8BT/ Graphene, the I-V characteristic curve of the diode in log I-log V scale is shown figure 4.12. Three major regions have been found in the figure 4.12. At low voltages (i.e. 0.01 to 0.1 V) the

current density is increased linearly with increasing the bias voltage. For voltages between 0.1 to 1V, it is observed that the current density is directly proportional to the  $V^{1.74}$ . With further increase of bias voltage, the current density shows  $V^{2.3}$  dependence. The transport in the second and third regions with slope  $\geq 2$  and this is like space-charge-limited-current (SCLC) mechanism. The first region is ohmic with slope about unity. The second region having a slope equal to 1.74 indicates space-charge-limited-current (SCLC) [S. Baranovski et al. 2006]. The third region has a slope  $\geq 2$  which can be attributed to trap charged current limited mechanism. The presence of traps might be due to impurities, various defects and randomly oriented deposited graphene flakes.

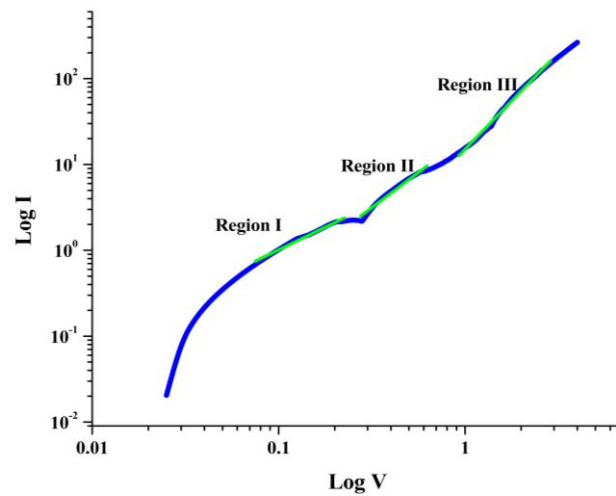


Figure 4-12 logI-logV characteristics of ITO/PEDOT-PSS/F8BT/Graphene.

## ***4.2 Graphene/Zinc Oxide Composite Deposition***

At the present time, a great attention is being pulled in research fields like electronics and biomedical by graphene–metal [Si Y et al. 2008, Muszynski R et al. 2008, Luechinger NA et al. 2008 ] and graphene–metal oxide [Williams G et al. 2008, Nethravathi C et al. 2008, Petit C et al. 2009] nano-composites due to their unique applications. These types of composites as derivatives of graphene and can be deployed in electronic devices. In metal oxides, n-type Zinc oxide (ZnO) has prompted worldwide research interest as a wide-band-gap (3.37 eV) semiconductor material [G.C. Yi et al. 2005, F. Lu et al. 2008] for its splendid potential applications in electronic and optoelectronic devices, such as photo-detectors [C.Y. Lu et al. 2006], light emitting diodes [J.H. Na et al. 2009], electroluminescence devices [W.I. Park et al. 2004], solar cells [P. Sudhagar et al. 2011], gas sensors [J. Xu et al. 2008], flat display devices [S.B. Park et al. 2011], piezoelectric nano-generators [Z.L. Wang et al. 2010], nano-lasers [M.H. Huang 2001, Y. Ito et al. 2011] and so on.

The charge transfer mechanism between graphene and metal is explained here from Pauli-exclusion interaction between metal and graphene. During the adsorption, the  $\pi$  electrons of graphene push the electron at the metal surface into the metal, decreasing the WF of the metal. On the other hand, smaller change would happen to graphene because it is energetically unfavorable to redistribute the  $\pi$  electrons, which requires hybridization with the s orbital. Thus, there is a new difference between the WFs of graphene and metal which enables electrons to transfer from metal to graphene. In the adsorption of graphene on ZnO polar surfaces, however, this phenomenon is less likely to happen since the electrons of the ZnO surfaces are more localized than those of metals, and the Pauli-exclusion would bring less influence to the WF of the ZnO surface. vdW forces between graphene and ZnO ensure a close but nondestructive contact at the interface, which allows a fast injection of the photosensitized electrons between ZnO and graphene; partial charge density analysis indicates that excited electrons with energy lower than 3 eV tend to accumulate on graphene; the intact Dirac point of graphene at the K point indicates that the superior electrical conductivity of graphene remains despite its adsorption on ZnO, reducing the possibility of electron–hole recombination.

In this section of the thesis, different possible approaches to graphene/ZnO composite thin film fabrication are discussed. From synthesis of graphene/ZnO dispersion to deposition,

each part is explicitly elaborated. The best fabrication route for composite thin film as cathode in diode device is found by using EHDA technique.

#### ***4.2.1 Decoration of Graphene Flakes with Zinc Oxide nanoparticles***

There are many synthesis routes has already established to combine ZnO and graphene thin films. Thermal decomposition [Zhu Y et al. 2006], electro-chemical route [Yin Z et al. 2010], plasma-enhanced chemical vapor deposition [Zheng WT et al. 2009], and a solvothermal process [Wu J et al. 2009] are among the synthesis routes which can be used to prepare nano-composite films. In this study electrohydrodynamic atomization(EHDA) technique as a route to fabricate graphene/ZnO thin film.

This work has been accepted for publication in Journal of Materials Science: Materials in Electronics by Adnan Ali et al. in 2013. A complete description of graphene thin film decoration with ZnO nano-particles for composite film fabrication is carried out by EHDA technique. Firstly, graphene thin film is deposited on silicon substrate and then followed by ZnO after curing by EHDA technique, respectively [Kotov, N. A. et al. 1996]. The graphene thin film is cured at 200°C for 90 minutes and then after depositing ZnO is cured at 200°C for 120 minutes. After curing, graphene/ZnO composite film has been characterized by using FE-SEM, UV-Vis-NIR spectroscopy, X-ray diffraction (XRD), Raman Spectroscopy and 3D-Nanomap. Besides this, graphene/ZnO electronic behavior as hybrid electrode is investigated by current voltage measurement of diode device. It is done by depositing graphene/ZnO as cathode on F8BT with diode structure i.e. ITO/PEDOT:PSS/F8BT/(Graphene/ZnO). It has been observed through characterizations that EHDA technique is useful for depositing a uniform graphene/ZnO thin film composite, which can be employed in electronic and optoelectronic devices.

#### ***4.2.2 Experiment for Graphene Flakes film Decoration with ZnO***

A schematic diagram of the EHDA setup has shown in the Figure 4.13. First graphene thin film was deposited and cured and then it was decorated by ZnO, using electrohydrodynamic atomization technique [Kotov, N. A. et al. 1996, X. Zhao et al. 2010]. A metallic nozzle of 310  $\mu\text{m}$  internal diameter [Havard 33G] was used as the anode, and it was connected to a Trek Model 610E high power source for the generation of the required electric field.

Graphene dispersion was subjected to electrostatic atomization at an applied flow rate of

300 $\mu$ l/h and a potential of 6.3 kV in the stable cone jet mode. The stand-off was changed from 5mm to 20mm to check for deposition area. The speed of moving substrate was changed from 1mm/sec to 5mm/sec to find optimum deposition parameters. For covering (2 $\times$ 2) cm<sup>2</sup> area on silicon substrate, optimum parameters are given in figure 4-13.

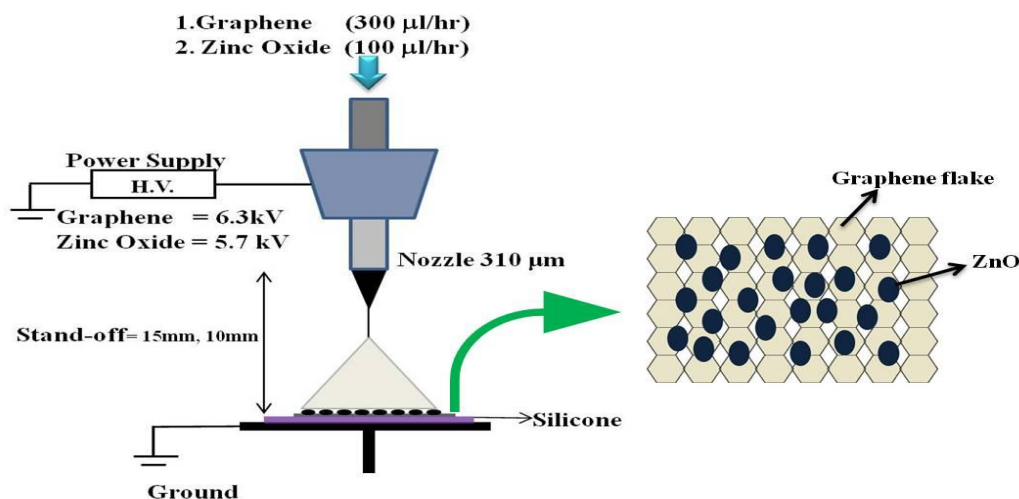


Figure 4-13 Schematic diagram of the system used for the experiment.

The EHDA experiments were initially performed with flow rates varying from 50 $\mu$ l/hr to 750 $\mu$ l/hr in order to determine the optimum spraying conditions with the stand-off distance fixed at 15 mm for graphene dispersion. Figure 4.14 represents high-resolution and high-speed images of different atomization modes captured for graphene.

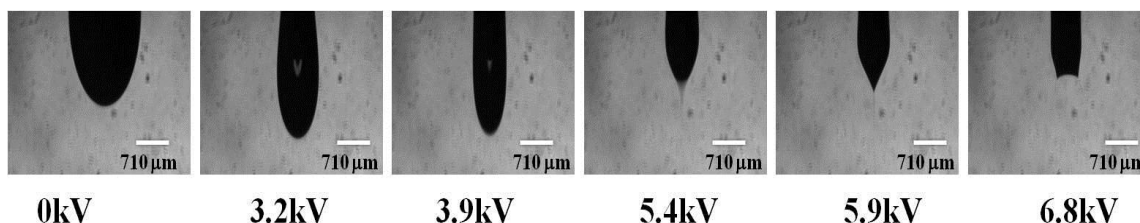


Figure 4-14 Electrohydrodynamic Atomization modes of graphene dispersion observed during the deposition process. a) Meniscus, b) dripping mode, c) micro-dripping, d) unstable cone-jet mode, e) stable cone-jet mode and f) multi-jet mode.

Figure 4.15 provides the observed operating envelopes of graphene flakes dispersion, representing different atomization zones with varying flow rates and corresponding applied voltages. A complete account of ZnO processing parameters can be found in Choi et al. [K.H. Choi et al. 2010]. A flow rate of 300 $\mu$ l/h and 100 $\mu$ l/hr were used, respectively, throughout the experiments for the deposition of graphene thin film followed by ZnO decoration. This value of flow rate was selected as the droplet size directly proportional to the cube root of flow rate.

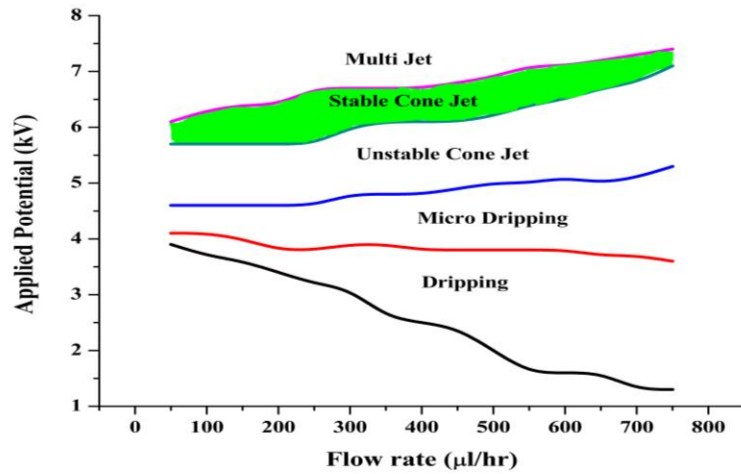


Figure 4-15 Operating envelop representation for different electro spray modes for graphene dispersion. The stable cone jet region is shaded to emphasize upon the possible flow-rate and voltage combination for optimized atomization conditions.

The occurrence of the classical hydrodynamic atomization requires the hydrodynamic relaxation time  $T_h$  to exceed the charge relaxation time  $T_q$ . Using the following values for these quantities,

$$L \approx 1200 \mu\text{m}$$

$$D \approx 30 \mu\text{m}$$

$$Q = 300 \mu\text{l/hr} = 8.33 \times 10^{-11} \text{m}^3 \text{s}^{-1}$$

$$\epsilon_r = 2.3$$

$$\epsilon_0 = 8.85 \times 10^{-12} \text{Fm}^{-1}$$

$$K = 0.0000122 \text{Sm}^{-1}$$

It implies that  $T_h \approx 0.0129 \text{ s}$  which is much greater than  $T_q \approx 1.67 \times 10^{-6} \text{ s}$ .

### 4.2.3 Morphological Analysis

Figure 4.16 (a-c low to high magnification) shows the FE-SEM image of graphene/ZnO composites. FE-SEM images of graphene/ZnO composite thin film fabricated by EHDA technique show that densely packed ZnO nano-grains are settled on top of graphene platelets. FE-SEM images also give an idea about the ZnO particles agglomeration. This agglomeration of nano-particles is due to the high surface interaction between nano-particles, which have a large specific surface area and high surface energy [S. Mohseni Meybodi et al. 2012]. Structural analysis (XRD and Raman spectroscopy) further has confirmed the FE-SEM images morphology of graphene/ZnO composite thin film.



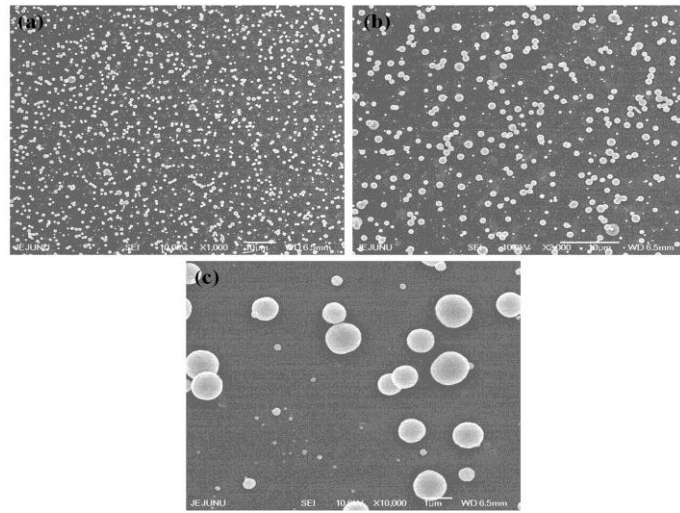


Figure 4-16 Low magnification FE-SEM surface view of the deposited films of Graphene/ZnO using deposition speed 3 mm/sec and 6mm/sec for graphene dispersion and ZnO dispersion, respectively. High magnification SEM micrographs showing graphene decorated with ZnO nano-particles and its agglomeration.

#### 4.2.4 Structural Analysis

Figure 4.17 shows the XRD patterns of graphene/ZnO composite. Both graphene and ZnO peaks are observed. This XRD pattern of graphene/ZnO is different from the one reported by other research groups [Ju H et al. 2010] because of our unique approach of film deposition. Graphene peaks are around  $23^\circ$  and  $44^\circ$  (of  $2\theta$ ). The XRD analysis further shows the excellent crystal structures of ZnO even if they are combined with graphene. While ZnO peak around  $33^\circ$ ,  $36^\circ$ ,  $46^\circ$  and  $57^\circ$  (of  $2\theta$ ) are there which correspond to (0 0 2), (1 0 1), (1 0 2) and (1 1 0) planes, indicating wurtzite crystal structure. The broadening of the ZnO diffraction peaks is attributed to the smaller particle sizes. It can be noticed that ZnO intensity is more as compared to graphene which is due to 3D crystalline structure and high values of its atomic number. The broad peaks of ZnO further confirm the decoration of graphene.

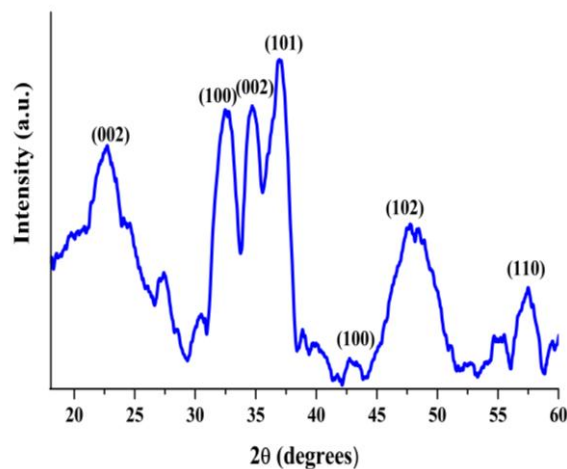


Figure 4-17 X-ray diffraction pattern of Graphene/ZnO film.

#### 4.2.5 3D Nano-mapping for surface roughness

NV-2000(Universal) non contact surface profiler with nano-level accuracy was used for surface roughness measurement in phase shifting interferometry (PSI) mode. In figure 4.18 (a and b) surface profile (3D and 2D) of graphene/ZnO has given, respectively. It shows that the roughness of film is 88.46 nm. Also variations in profile of film in the x-direction are shown in Figure 4. 6. (c), which are around -114nm to 114nm.

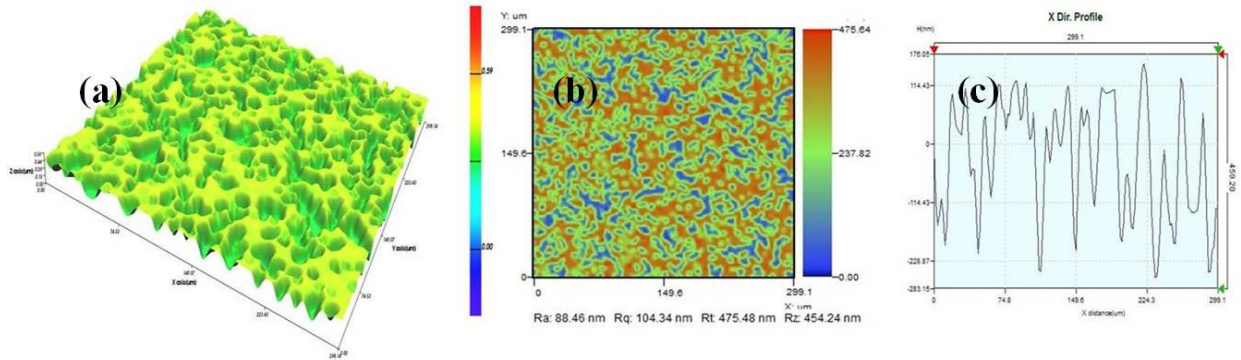


Figure 4-18 (a) 3D surface profile, (b) 2D surface profile and (c) X- profile of the graphene film decorated with ZnO, deposited on Si substrate.

#### 4.2.6 Raman Spectroscopy Analysis

Figure 4.7 presents the Raman spectra of graphene/ZnO, deposited by EHDA. Figure 4.19a, presents peaks at around 99 ( $E_2$ ), 303( $A_1$  (TO)) and 437  $\text{cm}^{-1}$  ( $E_2$  (high)) are observed in graphene/ZnO, which are the characteristic peak of the hexagonal wurtzite phase [I. Calizo et al. 2007]. Figure 4.19b shows three major peaks of D, G and 2D bands. D band is a breathing mode of  $\pi$ -point phonons of  $A_{1g}$  symmetry, which is attributed to local defects and disorders, particularly the defects located at the edges of graphene and graphite platelets. G band is generally assigned to the  $E_{2g}$  phonon of  $sp^2$  bonds of carbon atoms. The D/G intensity ratio of graphene/ZnO is 0.92, which assures the presence of graphene [ O. Akhavan et al. 2011], [ D. Graf et al. 2007] and [ I. Calizo et al. 2007].

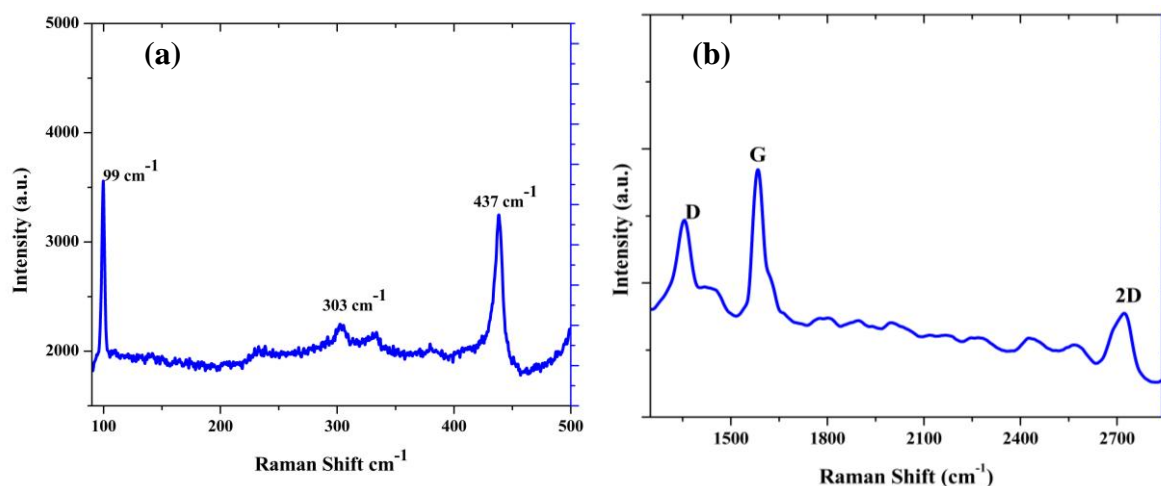


Figure 4-19 Laser Raman spectrum of graphene/ZnO composite.

According to the literatures, the 2D peak for the single-layer graphene sheet should be located at about  $2679\text{ cm}^{-1}$  [ O. Akhavan et al. 2011], [D. Graf et al. 2007] and [ I. Calizo et al. 2007], while for graphene sheets with multilayer, the 2D band normally shifts to the higher frequencies [ D. Graf et al. 2007] and [ I. Calizo et al. 2007]. In our case, the 2D band is located at about  $2724\text{ cm}^{-1}$ , which indicates the presence of few layers graphene. Moreover, Calizo et al. reported that the 2D band for the five-layer graphene sheet was located at about  $2755\text{ cm}^{-1}$  [ I. Calizo et al. 2007]. Therefore we can deduce that the number of the graphene layers in our graphene/ZnO samples would be 4-5 layers. Therefore, Raman spectra clearly confirm the presence of wurtzite-type ZnO and the presence of graphene/ZnO.

#### 4.2.7 Optical Properties

The spectrum shown in figure 4.20(a) a high peak at 286 nm corresponds to the excitation of  $\pi$ - plasmon of graphitic structure [X. Wang et al. 2008]. Another peak at 366 nm corresponds to the wurtzite hexagonal phase of ZnO. This shows that the observed absorption peak is blue shifted from that of bulk ZnO. This indicates the grain size-effect of ultrafine particles with nanometer size [X.M. Yang et al. 1994]. Figure 4.20(b) shows the transmittance spectra of graphene/ZnO, visible and near-infra-red (NIR) spectrum. Transmittance of the thin film is observed to be in the range of 85~87 % in the visible range. The transmittance spectrum reveals that the graphene/ZnO thin film deposited by EHDA technique is more suitable for optoelectronic device applications due to its good transmittance.

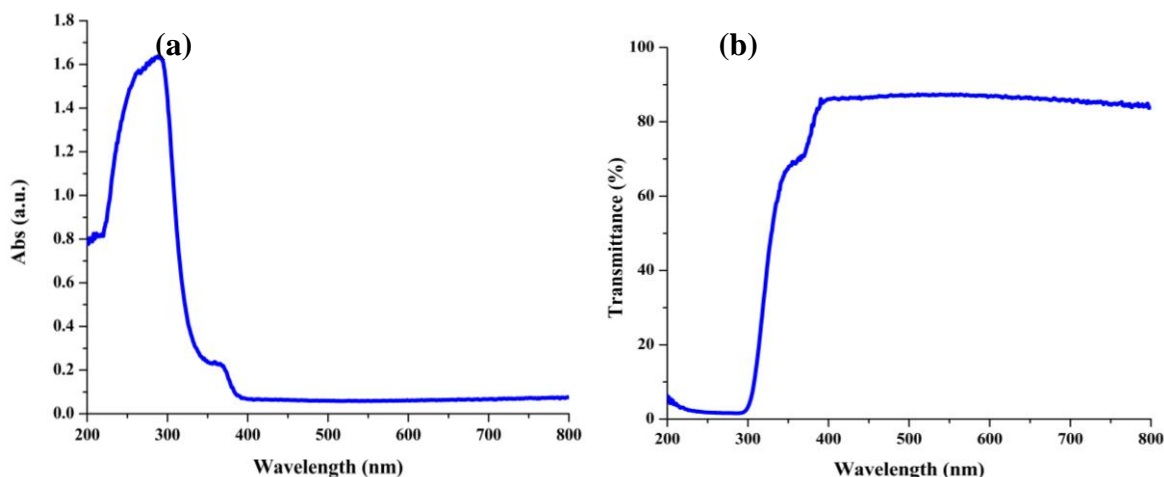
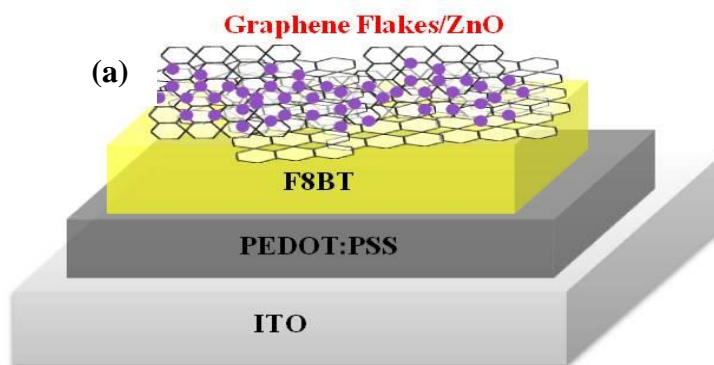


Figure 4-20 (a) & (b) Absorption and Transmittance spectra of graphene/ZnO, respectively.

#### 4.2.8 Electrical Behavior

The current density-voltage (J-V) curve of the organic diode device with structure ITO/PEDOT:PSS/F8BT/ (Graphene/ZnO) (schematic figure 4.21a) in linear scale recorded by semiconductor analyzer is shown in figure 4.21b, in which graphene decorated ZnO composited thin film is used as cathode. By the J-V plot, it is evident that there is proper contact between each adjacent layer. At voltage of 1V, the current density in organic structure is at low value of  $4.69 \times 10^{-3} \text{ A/cm}^2$  and after that as further voltage was applied, the device current density increased by the order of 200 and reaches up to  $1.034 \text{ A/cm}^2$  at voltage of 12V, indicating an increase in charge carrier injection.



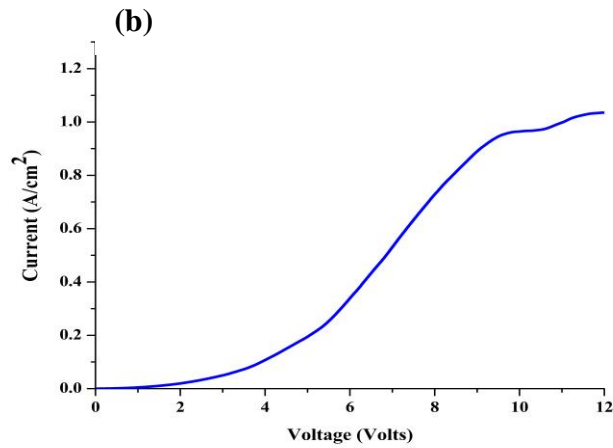


Figure 4-21 J-V characteristics of ITO/PEDOT-PSS/F8BT/(Graphene/ZnO) diode.

The I–V characteristic curve of the ITO/PEDOT: PSS/F8BT/ (Graphene/ZnO) diode in log–log scale is depicted in a log  $I$ –log  $V$  scale in f, indicate the current conduction mechanism. As it can be seen from the figure 4.22, three major regions have been found. At low voltages (i.e. 0 to 0.1 V) the current density increases linearly with increasing the bias voltage. It can also be observed that for voltage between 1.0 and 10 V the current density is directly proportional to the  $V^2$ . With further increase of bias voltage, the current density shows  $V^{2.63}$  dependence for the applied bias voltage. The transport in the second and third regions with slope  $\geq 2$  and this is like space-charge-limited-current (SCLC). The first region is ohmic with slope about unity. The second region having a slope equal to 1.95 indicates space-charge-limited-current (SCLC) with exponential distribution of deep traps in the band gap of organic semiconductor (F8BT) [J. Tauc (Ed.) 1974]. The third region has a slope  $\geq 2$  which can be attributed to trap charged current limited mechanism. The presence of traps might be due to impurities and various defects in the chemical structure of organic thin films.

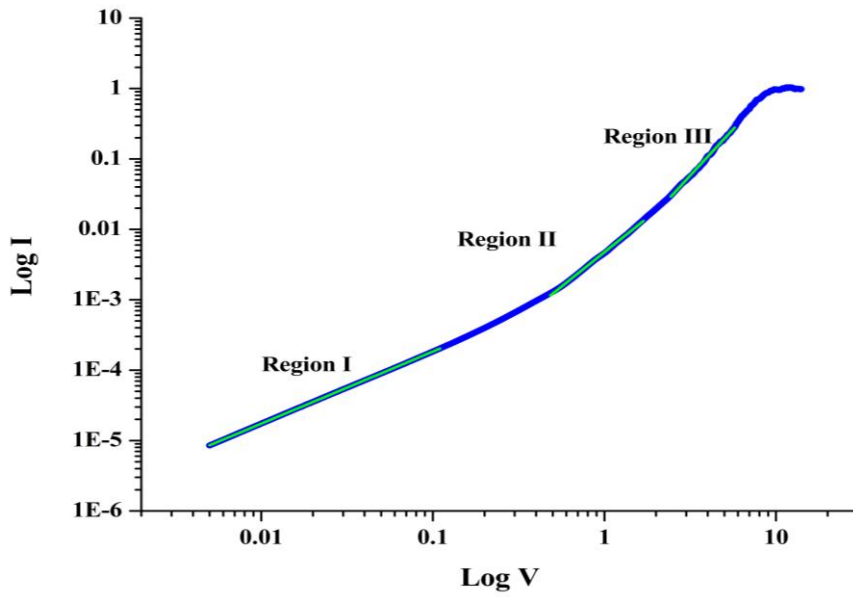


Figure 4-22 Double logarithmic current voltage characteristics (log I–log V) of ITO/PEDOT: PSS/F8BT/ (Graphene/ZnO) diode.

### **4.3 Direct Fabrication of Graphene/Zinc Oxide Composite Film**

This work has been published in Applied Physics A (Materials Science and Processing) [Adnan Ali et al. 2013]. In this work, a new mixed dispersion approach for graphene based composite has taken on. Graphene flakes (<4 layers) and a well-known semiconductor zinc oxide (ZnO) (<50nm particle size) have dispersed in N-methylpyrrolidone (NMP). Graphene/ZnO composite thin film is deposited by electrohydrodynamic atomization process on silicone substrate. It has been explored that high quality thin composite film is obtained at optimum flow rate of 300 $\mu$ l/hr at 6.3 kV applied potential after curing for 2 hours at 300°C. Graphene/ZnO thin composite film has been characterized by using Field Emission Scanning Electron Microscopy (FE-SEM), Ultra-violet Visible near Infra Red (UV-Vis-NIR) spectroscopy, X-ray diffraction (XRD), Raman Spectroscopy and 3D-Nanomap. For electrical behavior analysis, a simple diode Indium Tin Oxide (ITO)/(poly(3,4-ethylenedioxythiophene) poly(styrenesulfonate) (PEDOT:PSS)/polydiocetylfluorene-benzothiadiazole(F8BT))/(Graphene/ZnO) has fabricated. It is observed that at voltage of 0.3 V, the current in organic structure is at low value of  $1.20 \times 10^{-3}$  Amp/cm<sup>2</sup> and after that as further voltage was applied, the device current increased by the order of 110 and reaches up to  $1.32 \times 10^{-1}$  Amp/cm<sup>2</sup> at voltage 2 V.

#### **4.3.1 Materials and Synthesis of Dispersion**

The graphene flakes and ZnO nano particles were dispersed in NMP (4ml) solvent by bath sonication and centrifugation. The viscosity of mixed dispersion was measured to be 15.8 mPa by using Viscometer VM-10A system. The surface tension of was i.e. 54~57 mN/m, measured by Surface-electro-optics (SEO)'s contact angle analyzer. The electrical conductivity was 18.6  $\mu$ S/cm, measured by using conductivity meter (Cond6+ meter).

#### **4.3.2 Experiment for Deposition of Composite Thin Film**

A schematic diagram of the setup has shown in the figure 4.23. The dispersion was subjected to electrostatic atomization at an applied flow rate of 300 $\mu$ l/h and a potential of 6.3 kV in the stable cone jet mode. The stand-off was changed from 5mm to 20mm to check for optimum deposition area. The speed of moving substrate was changed from 1mm/sec to 3mm/sec to find optimum value. It was noticed that for covering (2\*2) cm<sup>2</sup> area on silicon substrate, optimum parameters of *stand-off* and velocity were 15mm and 3mm/sec, respectively. The

deposited graphene/ZnO was cured at 200°C for 2 hours.

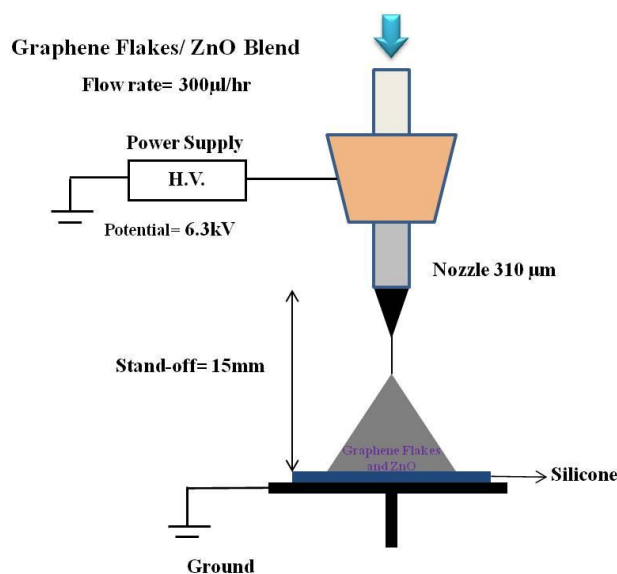


Figure 4-23 Schematic depiction of EHDA experimental setup.

The EHDA experiments were initially performed with flow rates varying from 50µl/h to 900µl/h in order to determine the optimum spraying conditions with the stand-off distance fixed at 15 mm. Figure 4.24 represents high-resolution and high-speed images of different atomization modes captured at 300 µl/h flow rate for various applied voltages.

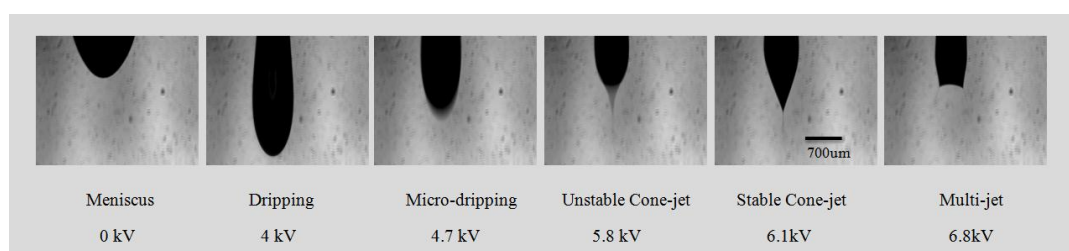


Figure 4-24 Electrohydrodynamic modes of Graphene/ZnO ink observed during the deposition process, a) Stable meniscus b) dripping, c) micro-dripping, d) pulsating unstable cone-jet, e) stable cone-jet, f) Multi-jet.

Figure 4.25 provides the observed operating envelope of graphene/ZnO dispersion representing different atomization modes with varying flow rates and corresponding applied voltages. It is evident from envelope that with increase of flow rate required applied voltage was increased from one to other mode. Reason for this increase in applied voltage for obtaining stable cone jet is to overcome the surface tension i.e. 54~57 mN/m. A stable cone-jet region is shaded in operating envelop given in figure 4.3 to emphasize the possible flow rate and voltage combinations for optimized atomization.



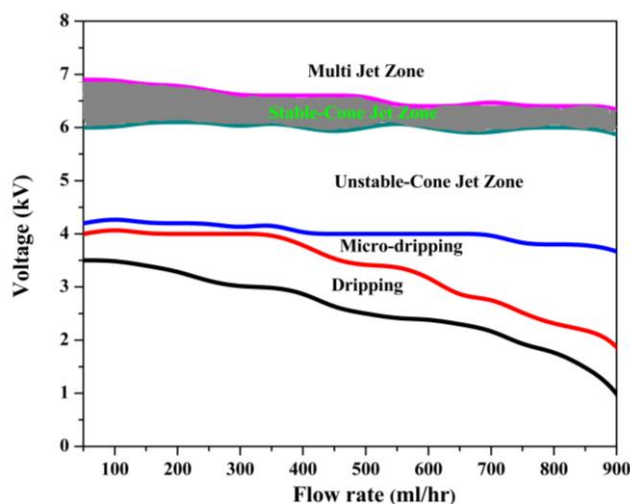


Figure 4-25 Operating envelop representation for different electro-spray regimes. The stable cone jet region is shaded to emphasize upon the possible flow rate and voltage combinations for optimized atomization conditions (stand-off $\approx$  15mm).

### 4.3.3 Morphological Analysis

Figure 4.26 (a-d low to high magnification) shows the FE-SEM image of graphene/ZnO composite thin film. Although, a mixed dispersion of graphene/ZnO is processed by EHDA but in FE-SEM images it can clearly be observed that packed ZnO nano-grains are settled on top of graphene flakes film. FE-SEM images also show that at some points ZnO particles are agglomerated. This agglomeration of nano-particles is due to the high surface interaction between nano-particles, which have a large specific surface area and high surface energy. There is high probability that ZnO nano-particles aggregation and semi-wrapping in graphene flakes have occurred during the curing process [S. Mohseni Meybodi et al. 2012]. Structural analysis has further given a confirmation of morphological effect in the thin film.

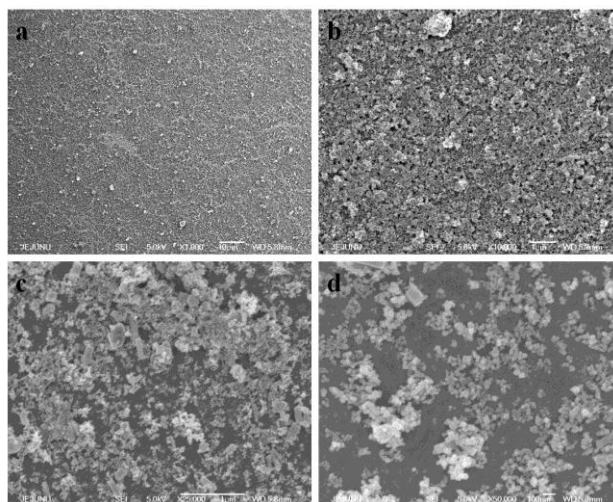


Figure 4-26 (a-d) Low magnification FE-SEM surface view of the deposited films of Graphene/ZnO using deposition speed 3 mm/sec. High magnification SEM micrographs showing ZnO nano-particles and its agglomeration on graphene flakes.

#### 4.3.4 3D Nanomapping for surface roughness

In figure 4.27. (a and b) surface profile (2D and X-direction) of graphene/ZnO are given, respectively. It shows that the roughness of film is 1.67 nm, while variations in film profile in the x-direction are mostly around 5.6 nm. In figure 4.27(c), 3D profile of graphene/ZnO film is shown. It can be elucidated that ZnO and graphene flakes deposited through EHDA technique are non-uniformly distributed and oriented in the film.

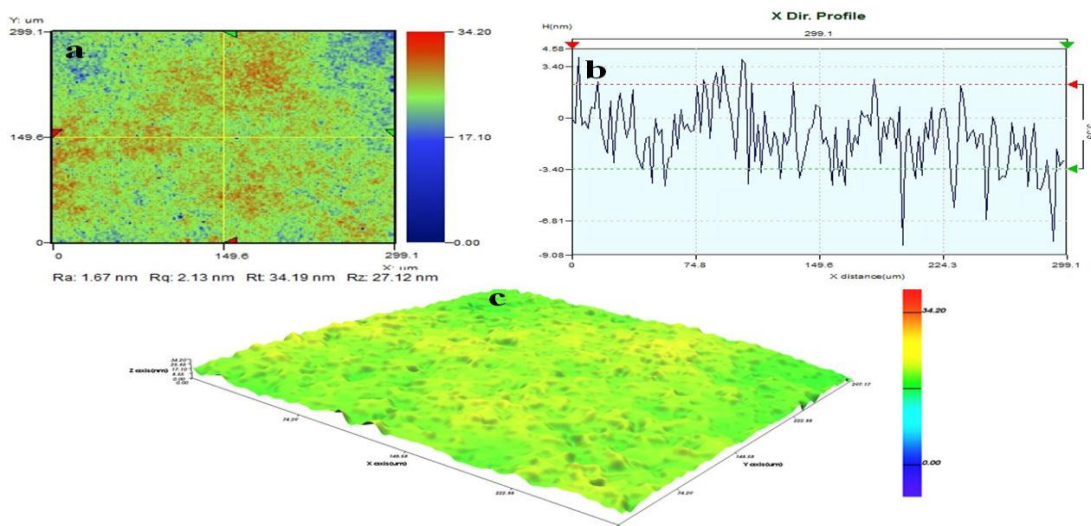


Figure 4-27 (a) 2D surface profile, (b) X- direction profile and (c) 3D surface profile of the graphene/ZnO film deposited on Si substrate.

#### 4.3.5 Raman Spectra of Graphene/ZnO

The Raman spectra of ZnO/G are presented in Figure 4.28. For ZnO/G, two bands appear at  $1350\text{ cm}^{-1}$  and  $1580\text{ cm}^{-1}$ , corresponding to the disordered (D) band and (G) band [Y. P. Zhang et al. 2009].  $I_G/I_{2D}$  ratio is 1.36 and 2D line width  $\sim 70\text{ cm}^{-1}$ , which confirms presence of few layers graphene. The peak at around  $434\text{ cm}^{-1}$  corresponds to Raman active optical phonon  $E_2$  (high) mode [W. S. Hummers et al. 1958], which is the characteristic peak of the hexagonal wurtzite phase [R. Zhang et al. 2009]. The peak at  $582\text{ cm}^{-1}$  is assigned to  $E_1$  (LO) mode associated with the structural defects in ZnO [X. Y. Ye et al. 2009, P. K. Sharma et al. 2011]. The bands located at near  $330$  and  $1130\text{ cm}^{-1}$  are due to the multiple-phonon scattering processes [J. M. Calleja et al. 1977]. The XRD and Raman spectra clearly confirm the presence of wurtzite-type ZnO and the presence of graphene/ZnO.

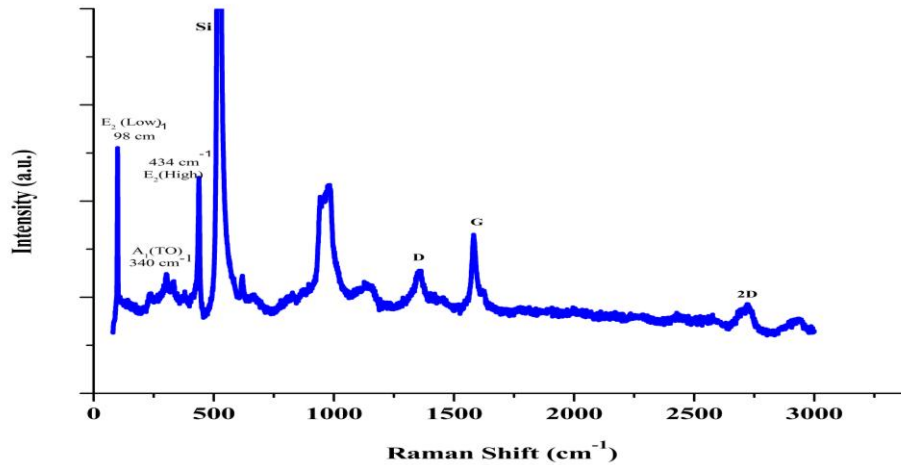


Figure 4-28 Laser Raman spectrum of graphene/ZnO film.

#### 4.3.6 Optical Properties

The band gap of graphene/ZnO is evaluated from absorbance spectra figure 4.29(a) of composite thin film coated on optically transparent glass. The optical band gap of graphene/ZnO was estimated by fundamental relation given by equation  $\alpha hv = B(hv - E_g)^n$ , where  $\alpha$  is the absorption coefficient,  $hv$  the energy of absorbed light,  $n = 2$ , for indirect allowed transition and  $B$  is proportionality constant [J. Tauc (Ed.) 1974]. Energy gap ( $E_g$ ) was obtained by plotting  $(\alpha hv)^2$  vs.  $hv$  and extrapolating the linear portion of  $(\alpha hv)^2$  vs.  $hv$  to zero, as shown in figure 4-8 (b). The band gap of graphene/ZnO was estimated to be 3.7 eV by using this method.

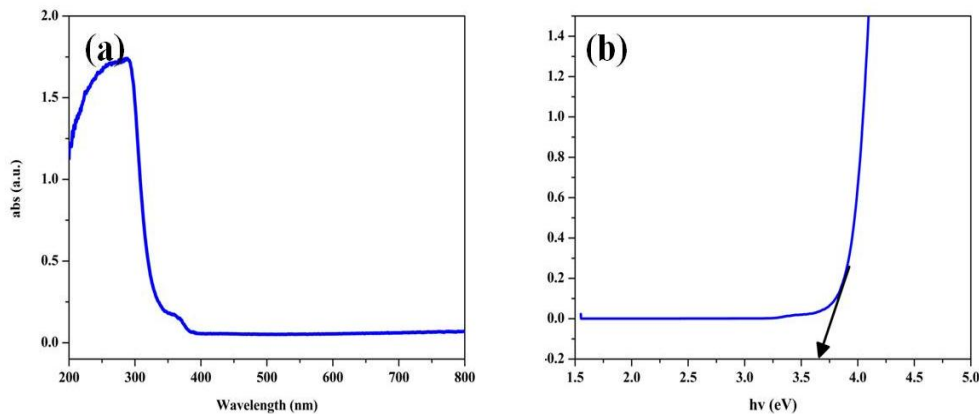


Figure 4-29 (a) UV-vis spectrum of graphene/ZnO (b)  $(\alpha hv)^2$  vs.  $hv$  plot for bandgap estimation of graphene/ZnO film.

### 4.3.7 Electrical Behavior

In Figure 4.30, JV plot, it is evident that there is appropriate contact between each adjacent layer. At voltage of 0.3 V, the current density in organic structure is at low value of  $1.20 \times 10^{-3} \text{ Amp/cm}^2$  and after that as further voltage was applied, the device current increased by the order of 110 and reaches up to  $1.32 \times 10^{-1} \text{ Amp/cm}^2$  at voltage 2 V, indicating an increase in charge carrier injection.

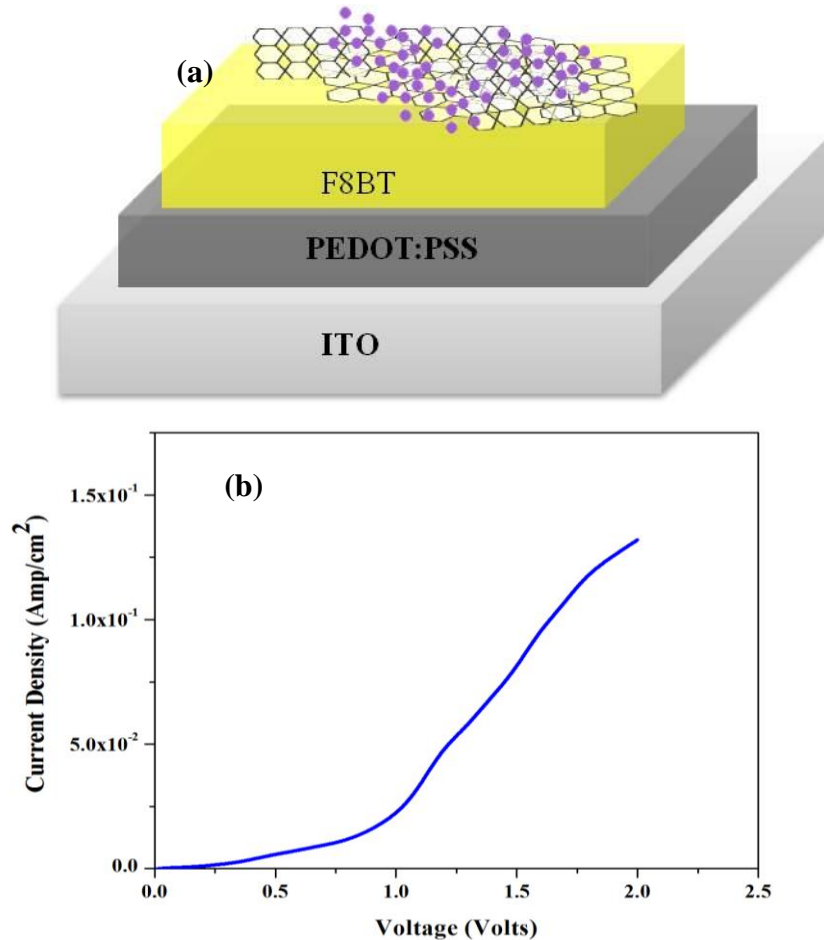


Figure 4-30 I-V characteristics of ITO/PEDOT:PSS/F8BT/(Graphene-ZnO) diode device.

In a diode, when the higher carrier densities from one electrical contact are locally injected into material, the space charge limited currents may take place and can be identified by analyzing the behavior of curve of IV in log-log scale. The plot of  $\log I$  vs  $\log V$  was made as shown in figure 4.31 and was analyzed. The dominant charge transport mechanism for the diode was determined by obtaining “m” values from the slopes of linear regions in figure 4. 10. The slopes of the region I, region II and region III are shown in figure 4. 10 was found to be 0.934 and 1.774 and 3.527 respectively, indicating the presence of space charge limited conduction [R. K Gupta et al. 2004].

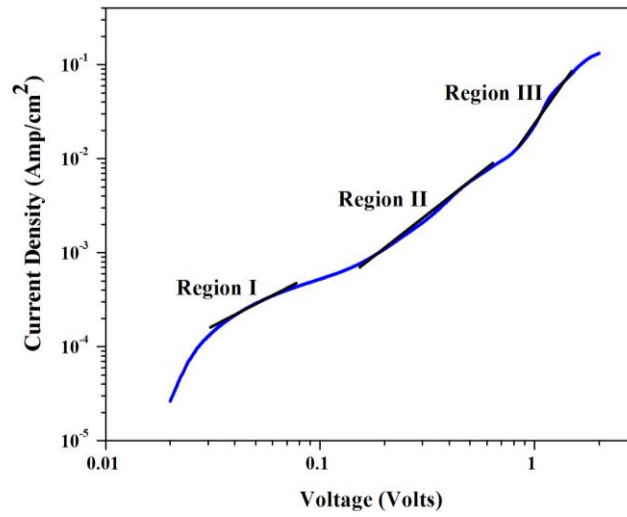


Figure 4-31 logI - logV characteristics of ITO/PEDOT-PSS/F8BT/(Graphene-ZnO) diode device.

#### 4.4 Direct Deposition of Graphene/ZnO Composite Film by Semi-blended Approach

Graphene/ZnO composite film is fabricated by a fast and easy semi-blended approach. Zinc oxide (ZnO) (<50nm particle size) dispersed in ethanol is immediately deposited on uncured pre-deposited graphene flakes (<4 layers) dispersed in N-methylpyrrolidone (NMP), using electrohydrodynamic atomization technique (EHDA). Graphene/ZnO composite film is characterized morphologically, structurally and chemically. This work has been submitted to Japanese Journal of Applied Physics by Adnan Ali et al. 2013.

##### 4.4.1 Graphene Flakes and ZnO Deposition from dispersion

Figure 4.32 shows schematic diagram of the EHDA setup for Semi-blended approach of graphene/ZnO composition thin film. First, graphene thin film was deposited and then before curing, immediately ZnO was atomized on to it, using electrohydrodynamic atomization technique [N.A. Kotov et al. 1996, X. Zhao et al. 2010].

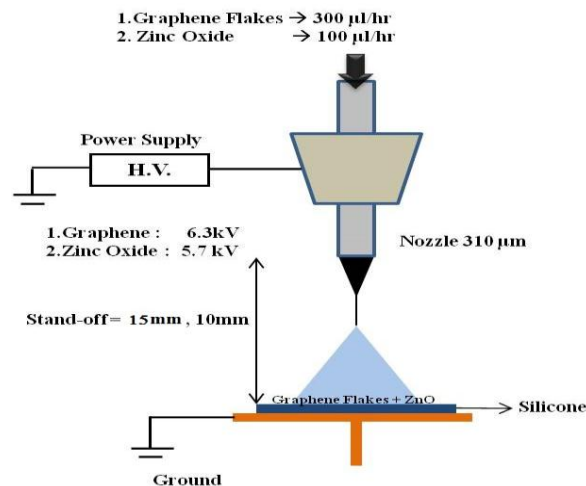


Figure 4-32 Schematic diagram of EHDA experimental setup.

##### 4.4.2 Morphological Analysis

Figure 4.33 (a-c low to high magnification) shows the FE-SEM image of graphene/ZnO composite film. FE-SEM images of graphene/ZnO composite thin film fabricated by EHDA technique show that densely packed ZnO nano-grains are settled on top of graphene flakes and FE-SEM images also give an idea about the ZnO particles agglomeration. This agglomeration of nano-particles is due to the high surface interaction between nano-particles, which have a large specific surface area and high surface energy [S. Mohseni Meybodi et al. 2012]. Also it can be observed in figure 4.4 (d, e) that some of the ZnO nano-particles are partially covered in graphene flakes.

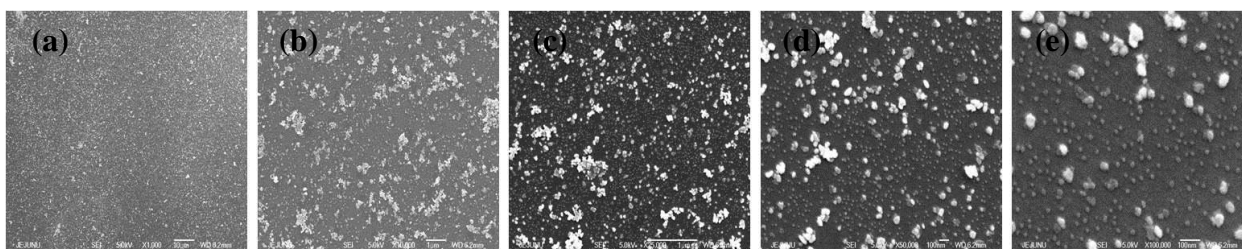


Figure 4-33 Low magnification FE-SEM surface view of the deposited films of Graphene/ZnO using deposition speed 3 mm/sec and 6mm/sec for graphene dispersion and ZnO dispersion, respectively. High magnification SEM micrographs showing graphene decorated with ZnO nano-particles and its agglomeration.

#### 4.4.3 Raman spectra

Figure 4.34 (a) shows the whole Raman spectra of graphene/ZnO composite film. A strong Si signal and several weak peaks are observed in the film deposited on Si substrates. In Raman spectrum of graphene figure 4.34 (c), three sharp peaks at 1350, 1583 and 2724  $\text{cm}^{-1}$  correspond to the D, G and 2D peaks, respectively. Several weak peaks are also observed in the G–ZnO hybrids except for the D, G and 2D peaks. The D peak is due to the presence of structural disorders in graphene sheets. The G peak is attributed to the optical  $E_{2g}$  phonons at the Brillouin zone centre, whereas the ratio of the intensity of the G-band to the D-band is related to the in-plane crystallite size [K. S. Subrahmanyam et al. 2008]. Besides, the intensity ratio of  $I_G/I_D$  is widely used to characterize the defect quantity in graphene and a low ratio indicates a great disorder arising from structural defects [M. A. Pimenta et al. 2007]. As seen in figure 4.34, the integrated intensity ratios of  $I_G/I_D$  in the graphene/ZnO composite film ( $I_G/I_D = 1.745$ ) is lower than in graphene ( $I_G/I_D = 3.14$ ). These indicate that the presence of graphene flakes network structure which is changed or damaged with ZnO nanoparticles decoration. Figure 4.34(b) shows the ZnO portion of Raman spectra ranging from 100–800  $\text{cm}^{-1}$  [A. Chavez-Valdez et al. 2013]. For ZnO, peaks at 99, 302, 436, 615  $\text{cm}^{-1}$  are obtained. Exarhos et al. reported that peaks at 101 ( $E_2$ ), 437 ( $E_2$ ), and 583  $\text{cm}^{-1}$  ( $E_1$  (LO)) corresponded to bulk ZnO [G. J. Exarhos et al. 1997]. The noteworthy peaks of the modes that occur in the graphene/ZnO composite film are the appearance of the 304 and 431  $\text{cm}^{-1}$  ( $E_2$ ) and the absence of the 106  $\text{cm}^{-1}$  ( $E_2$ ) mode [K. Mcguire et al. 2002].

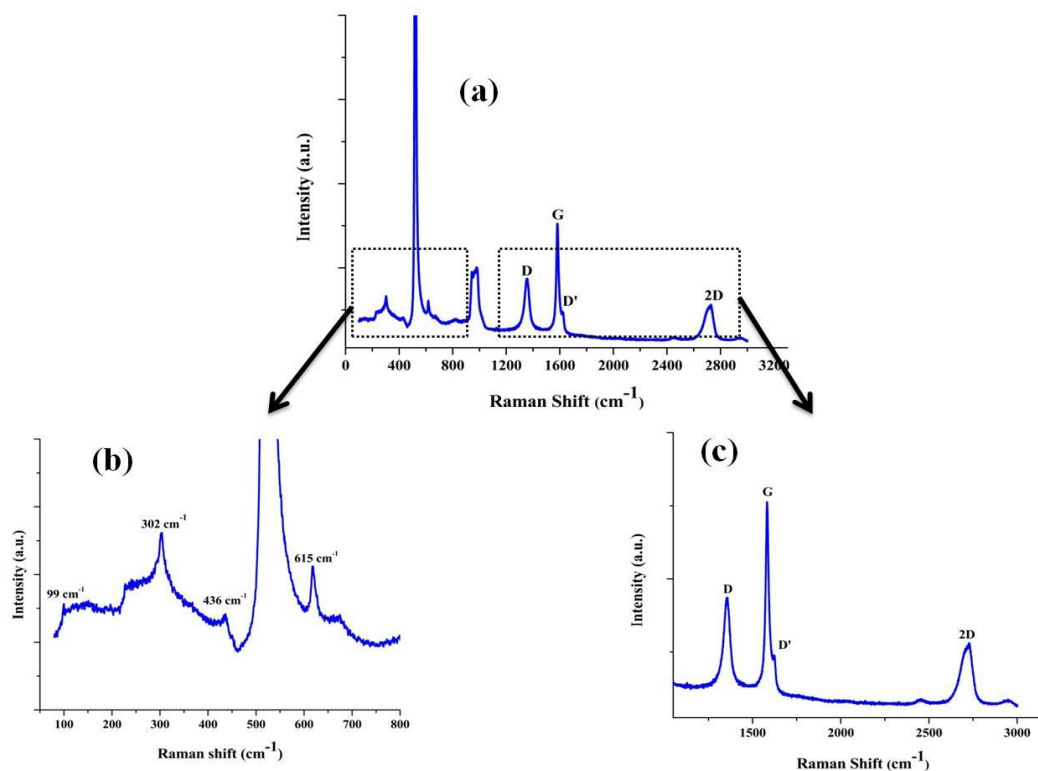


Figure 4-34 Laser Raman spectrum of graphene/ZnO composite.

#### 4.4.4 Optical Analysis

Figure 4.35(a) shows the transmittance spectra of graphene/ZnO, visible and near-infra-red (NIR) spectrum. Transmittance of the thin film is observed to be in the range of 81~83 % in the visible range. The band gab of graphene/ZnO is evaluated by depositing it on an optically transparent glass using the same approach. The optical band gap of graphene/ZnO is estimated by fundamental relation given by equation  $ahv = B(hv - E_g)^n$ , where  $a$  is the absorption coefficient,  $hv$  the energy of absorbed light,  $n = 2$ , for indirect allowed transition and  $B$  is proportionality constant [J. Tauc (Ed.) 1974]. Energy gap ( $E_g$ ) was obtained by plotting  $(ahv)^2$  vs.  $hv$  and extrapolating the linear portion of  $(ahv)^2$  vs.  $hv$  to zero, as shown in figure 4.35(b). The bandgap of graphene/ZnO was estimated to be 3.22 eV by using this method.



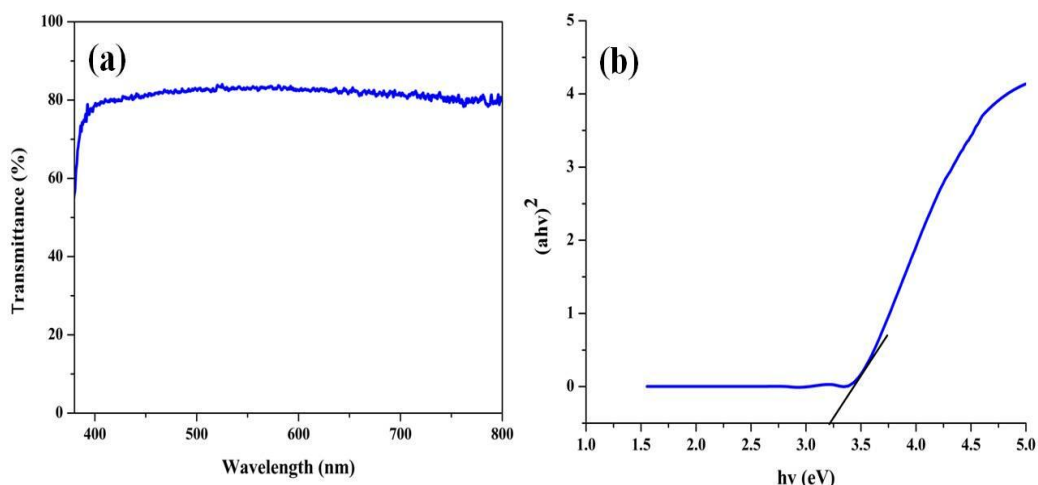


Figure 4-35 (a) Transmittance spectra of graphene/ZnO film (b)  $(ahv)^2$  vs.  $hv$  plot for bandgap estimation of graphene/ZnO film.

#### 4.4.5 Electrical Analysis

The current density-voltage (J-V) curve of the organic diode device with structure ITO/PEDOT:PSS/F8BT/ (Graphene/ZnO) in linear scale is shown in figure 4.36, in which graphene decorated ZnO is used as cathode. At voltage of 0.3V, the current density in organic structure is at low value of  $1.4 \times 10^{-5} \text{ A/cm}^2$  and after that as further voltage was applied, the device current density increased by the order of 50 and reaches up to  $6.3 \times 10^{-4} \text{ A/cm}^2$  at voltage of 2V, indicating an increase in charge carrier injection. By the J-V plot, it is evident that there is proper contact between each adjacent layer.

For current conduction mechanism, log-log scale of the I-V characteristic curve of the ITO/PEDOT: PSS/F8BT/ (Graphene/ZnO) diode device is drawn in Figure 4.37. As it can be seen from the figure 4.37, three major regions have been found. At low voltages (i.e. 0 to 0.1 V) the current density increases linearly with increasing the bias voltage. It can also be observed that for voltages between 0.1 and 1V the current density is directly proportional to the  $V^{1.6}$ . With further increase of bias voltage, the current density shows  $V^2$  dependence for the applied bias voltage. The transport in the second and third regions with slopes 1.6 and 2 indicates space-charge-limited-current (SCLC). The first region is ohmic with slope about unity. The second region having a slope equal to 1.6 indicates space-charge-limited-current (SCLC) with exponential distribution of deep traps in the band gap of organic semiconductor (F8BT) [J. M. Calleja et al. 1977]. The third region has a slope  $\sim 2$  which can be attributed to trap charged current limited mechanism. The presence of traps might be due to impurities and

various defects in the chemical structure of organic thin films.

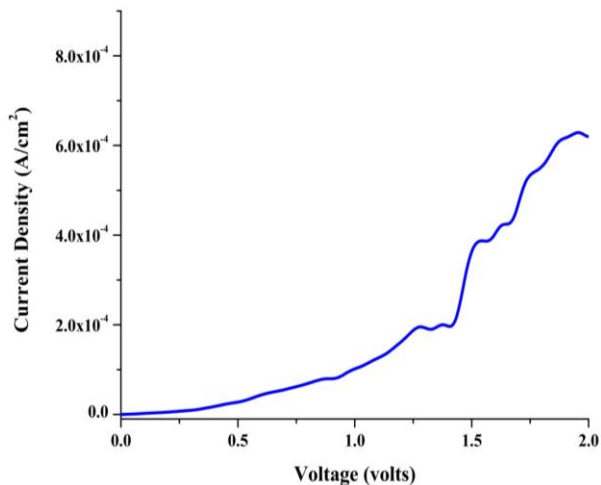


Figure 4-36 I-V characteristics of ITO/PEDOT-PSS/F8BT/(Graphene/ZnO) diode.

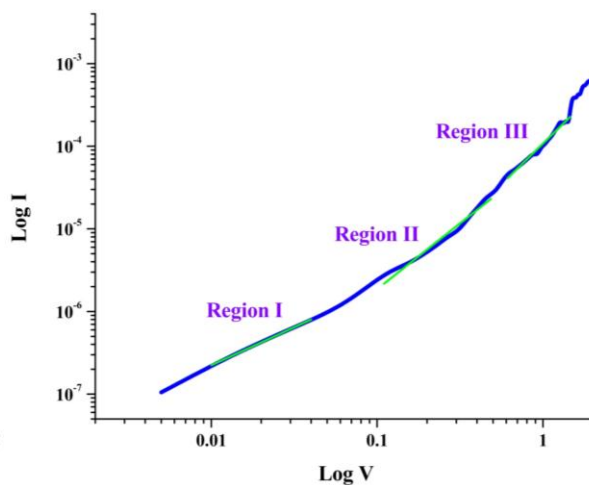


Figure 4-37 log I - log V characteristics of ITO/PEDOT-PSS/F8BT/(Graphene/ZnO) diode.

#### **4.5 Fabrication of Dielectric Poly (4-Vinylphenol) Thin Film**

Poly 4-vinylphenol has been reported most frequently because of its having performance than other members of the family of gate dielectrics [S. Lee et al. 2006, T. H. Kim et al. 2008]. Gate dielectric crosslinked poly 4-vinylphenol (C-PVP) is investigated mostly for the fabrication of OTFTs due to the easy thin-film formation and to its excellent dielectric properties [Y. Choi et al. 2009]. However, the thin film deposition of C-PVP has been regarded to require very high temperatures (higher than 175 °C), rendering C-PVP unsuitable for dielectric thin film deposition on various flexible substrates [T.H. Kim et al. 2008, Y. Choi et al. 2009]. Also, the cross-linking reaction between PVP and the crosslinker has been reported to occur at high temperatures and to enhance the mechanical, thermal and electrical properties of C-PVP. However, a high possibility exists that the processing temperature of C-PVP can be reduced to around 100 °C.

Dielectric PVP thin film is fabricated using EHDA process is discussed here in this section. Solution-processible PVP ink was synthesized and its physical properties were measured to determine EHDA processing parameters. The PVP dielectric thin films deposited by using EHDA process were cured at 110°C for 1 h. After it had been cured, the film was characterized physically as well as electrically. The film's compositional quantification was carried out using an X-ray photoelectron spectroscopy (XPS) analysis. The surface morphology was characterized through a scanning electron microscope (SEM) analysis and the thickness was measured by using a noninvasive thickness measurement system based on the principle of constructive and destructive interference in the spectrum of white light incident on the surface of a film. Besides this, the optical characterization of the film was done by using an UV/VIS/NIR spectrophotometer. For the electrical characterization of dielectric thin film, a simple metal-insulator-semiconductor (MIS) structure, i.e., ITO/PVP/PEDOT: PSS was fabricated and characterized for application in electronic devices by I-V and C-V analyses. This work has been published in Journal of the Korean Physical Society [K.H.Choi et al. 2013] and a continuation of this work is published in Journal of Electronic Materials [Adnan Ali et al. 2013].

##### **4.5.1 PVP Ink Synthesis**

PVP (Avg. Mw 25000) powder, the cross-linking agent (CLA) poly (melamine-co-formaldehyde) and propylene glycol methyl ether acetate (PGMEA) solvent were purchased

from Sigma Aldrich. The PVP powder was dissolved in PGMEA solvent; then CLA was added to it. The solution was then magnetically stirred for 24 hours at room temperature. After dissolution, for better solubility of PVP powder, the solution was ultra-sonicated for 10 minutes with 10% amplitude. Ink properties are given in table 4.1.

Table 4-1. PVP Ink Properties

PVP Ink Properties	
Viscosity (mPa)	13.2
Surface Tension (mN/m)	10.05
Dielectric Constant	4.5
Conductivity ( $\mu\text{S}/\text{cm}$ )	0.35
Contact Angle on ITO (degrees)	24.94 $^\circ$

#### 4.5.2 Film Fabrication

A schematic diagram of the setup is shown in the Figure 4-38. The deposition of C-PVP ink was carried out using an EHDA technique [A. Khan et al. 2011, K.H. Choi et al. 2012]. It was processed as graphene flakes. The deposited dielectric thin PVP film is cured at 110 $^\circ\text{C}$  for 1hour.

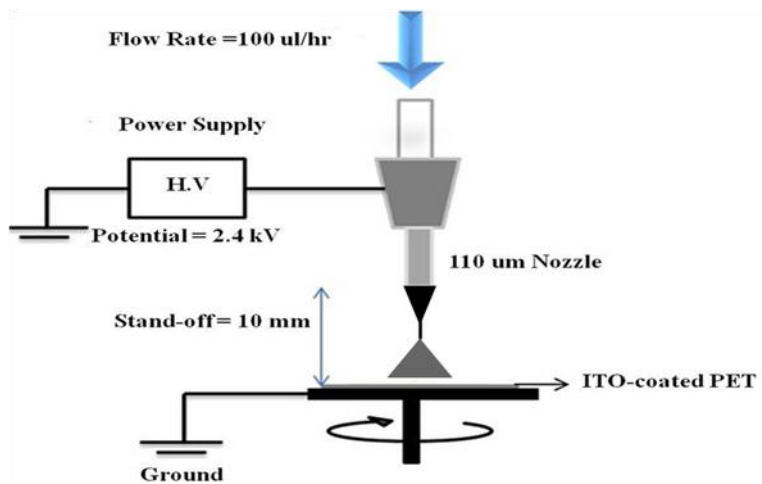


Figure 4-38 Schematic diagram of the experimental setup.

#### 4.5.3 Results and Discussions

A PVP solution-processible ink operating envelope is explored by investigating EHDA. The EHDA is first performed at various varying flow rates i.e. 100 $\mu\text{l}/\text{hr}$  to 1500 $\mu\text{l}/\text{hr}$  in order to

determine the optimum spraying envelope. Figure 4-39 shows high-resolution and high speed images of different EHDA modes.

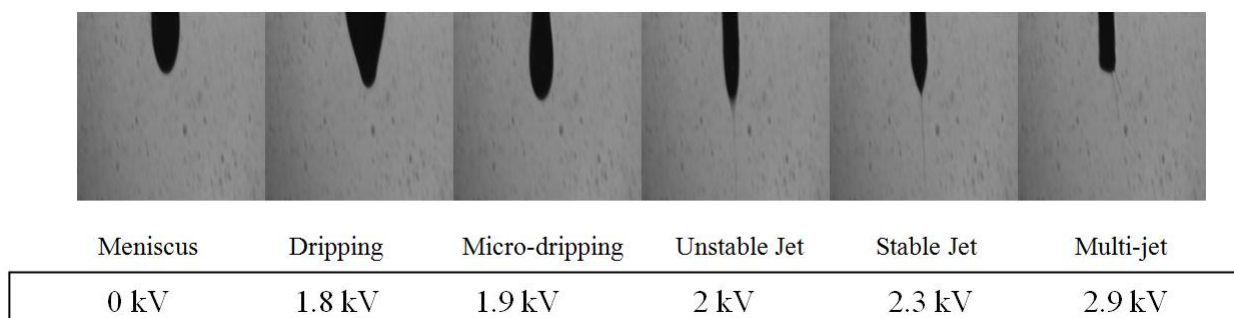


Figure 4-39 Modes of electrostatic atomization of PVP ink: dripping, microdripping, pulsating unstable cone jet, stable cone jet and multi-jet.

In Figure 4-40, the operating envelope of the PVP ink is given and shows various atomization zones with varying flow rate and their corresponding potential difference. The optimized parameters for electrostatic atomization for dielectric film deposition are given in Table 4-2.

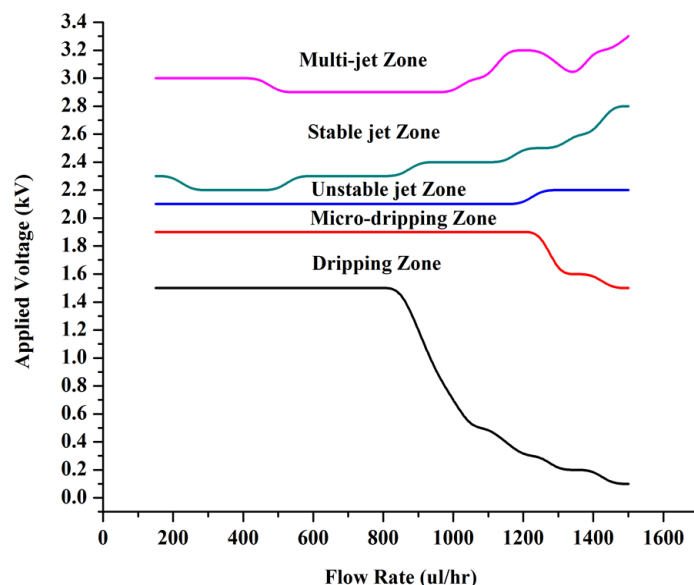


Figure 4-40 Operating envelope of PVP ink.

The surface morphology of the film is studied by using SEM analysis. Figure 4-41 shows SEM images of a deposited PVP film. The morphology of the film is uniform and pinhole-free throughout the ITO-coated PET, which means film surface compatibility, and will become considerably better with succeeding deposited layers. Also, the film thickness is measured by using ellipsometer and is found to be 100 nm.

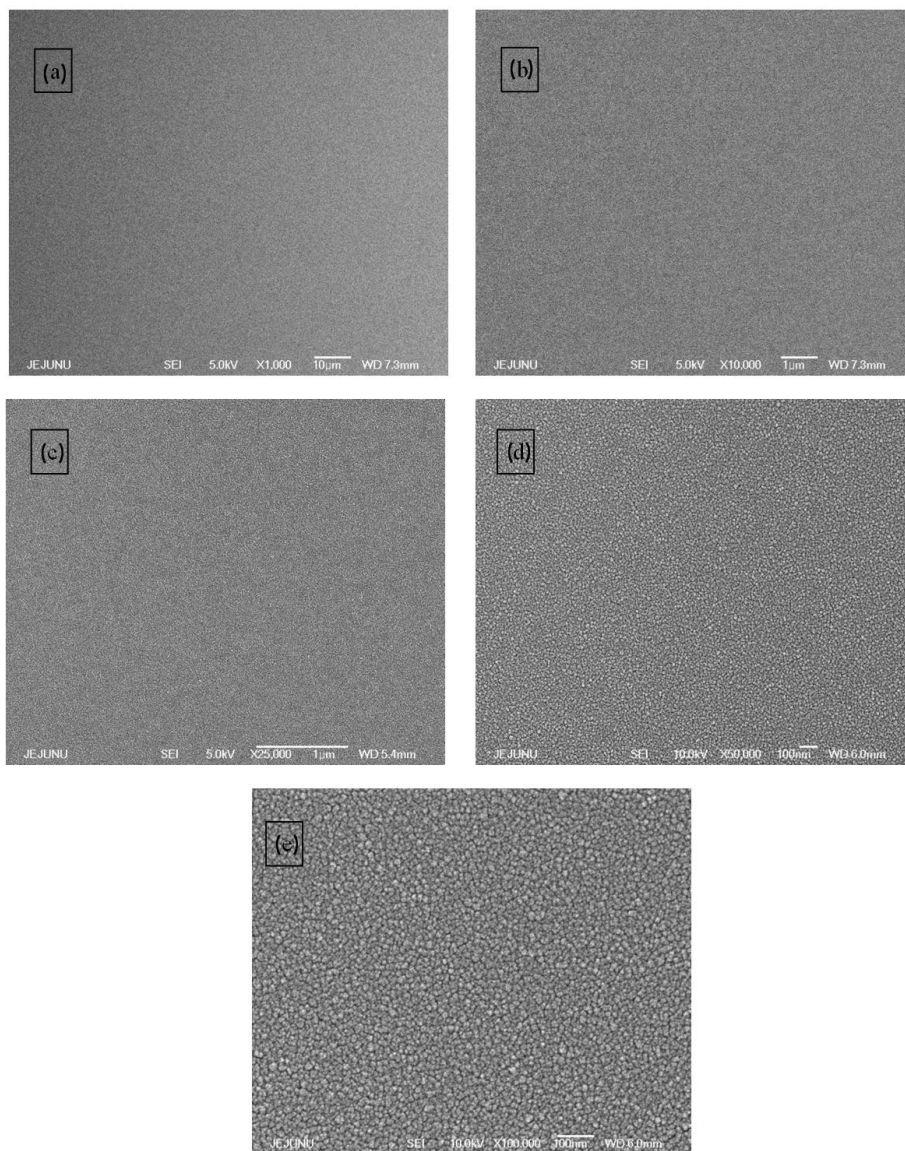


Figure 4- 41 (a) – (e) SEM surface morphology of a PVP dielectric thin film from low to high magnification.

The film purity and the absence of impurities are confirmed by using XPS measurements. Figure 4-42 the marked XPS graph for the PVP film deposited on ITO-coated PET. All of the peaks on the curve are ascribed to elemental O and C, and no identifiable peaks of other elements were observed. Therefore, we conclude that the film is purely PVP.

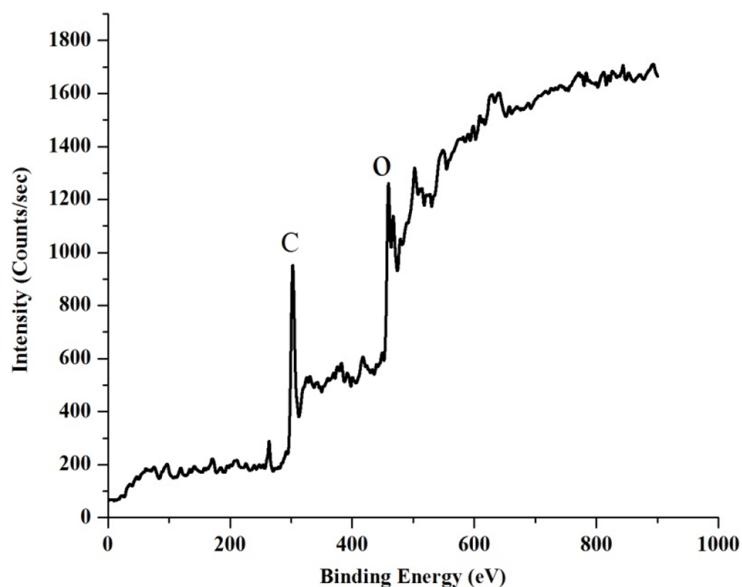


Figure 4-42 XPS analysis representation of a deposited PVP layer. C and O peaks are marked.

For the optical properties, the transparency of the film is recorded by using an UV/Vis/NIR spectrometer (Shimadzu UV-3150) in the range of 200–800 nm. Figure 4-43 shows the transmittance spectra for an EHDA deposited thin PVP film in an ultraviolet (UV), visible and near infra-red (NIR) spectrum. The transmittance of the thin film is observed to be in the range of 89 – 93% in the visible range. The absorption appears below 298 nm in the UV range. The transmittance spectrum reveals that which comes out to be 3.0525 eV. This calculated  $E_g$  value reflects the insulative and dielectric nature of the PVP film.

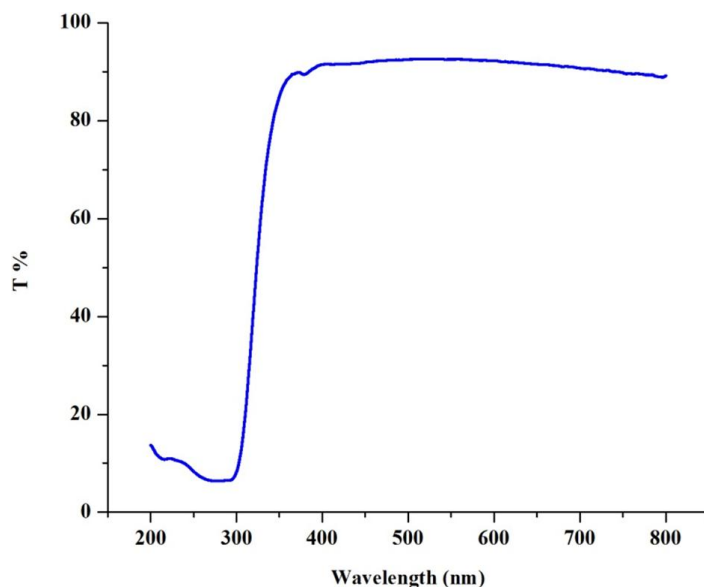


Figure 4-43 UV-vis spectra of PVP thin films showing the transmittance.

To further confirm the insulative nature of the thin PVP film, we performed an I-V analysis. In Figure 4-44, the I-V curve for the deposited PVP thin film is given. The graph shows a non-ohmic behavior, which is representative of a typical insulative film with a dielectric nature.

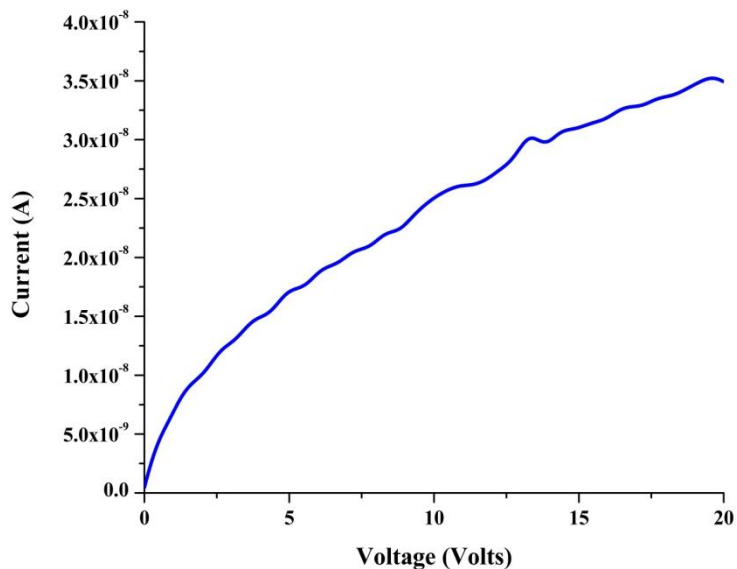


Figure 4-44 I-V curve for a PVP thin film.



## **4.6 Different Approaches to Fabricate PVP/Graphene composite film using Electrohydrodynamic Atomization Technique**

Graphene/PVP composite film is fabricated by two different approaches for use in electronic devices. One is blended approach and other is layer-by-layer (LBL) approach while using Electrohydrodynamic atomization (EHDA) technique. Graphene/PVP composite thin film fabricated by blended and LBL approaches are characterized by field emission scanning electron microscope for surface uniformity checking, UV-visible spectroscopy is used for optical analysis which has shown nearly 88.5% of transparency in the visible region. For electrical analysis Graphene/PVP composite thin film has employed as dielectric layer in capacitor having ITO and PEDOT: PSS as bottom and top electrodes, respectively. Graphene/PVP composite thin film fabricated by blended and LBL approaches are compared with PVP in capacitor. It is observed that maximum capacitance  $1.21 \times 10^{-5}$  F/cm<sup>2</sup> at 1 kHz in the voltage range  $-1.3 \times 10^{-1}$  to 1.78 V is achieved for LBL approach fabrication of graphene/PVP composite thin film. Also its behavior at high frequencies was measured and it has noticed that with increase in frequency capacitance has been decreased but its behavior remained stable.

### **4.6.1 Graphene/PVP Ink Synthesis for Blended fabrication Approach**

Graphene platelets from Cheap Tubes (<4 layers and surface area >750m<sup>2</sup>/g), N-methylpyrrolidone (NMP) solvent and Poly 4-vinylphenol (PVP) from Sigma Aldrich were purchased. The graphene platelets and Poly 4-vinylphenol (PVP) were dispersed in NMP (4ml) solvent by bath sonication for 30 minutes and centrifugation was carried out for 5 minutes at 10% amplitude.

### **4.6.2 Film Fabrication**

The deposition of graphene/PVP was carried out using an EHDA technique [Zhao, X. et al. 2010]. A metal nozzle of 310 μm internal diameter [Havard 33G] was used as the anode. Ground was provided by connecting the ground terminal of the power source to a moving stage that holds the substrate. Graphene/PVP ink operating envelop was explored by changing flow rate and applied voltages, as shown in figure 4.45. It was noticed that for covering (2×2) cm<sup>2</sup> area on silicon substrate, optimum parameters of stand-off and velocity were 15mm and 3mm/sec, respectively. The deposited graphene/PVP was cured at 200°C for 2 hours.

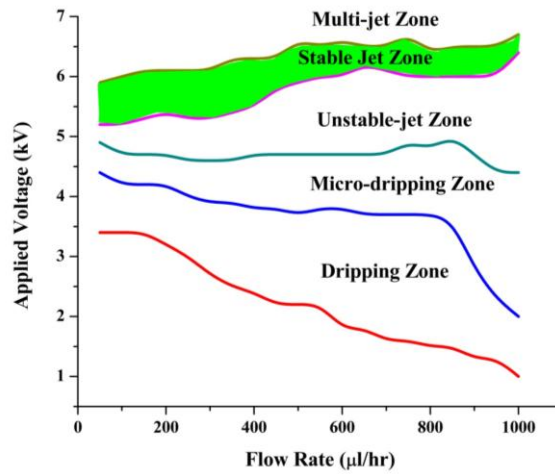


Figure 4-45 Graphene/PVP ink operating envelop.

### 4.6.3 Characterizations and Discussion

Figure 4.46 (a-d low to high magnification) shows the FE-SEM images of graphene/PVP composite thin film. It is obvious from SEM images that composite film is uniform throughout. From its capacitance behavior as dielectric film, it is extracted that at low frequency and low voltage values, its performance is satisfactory but at high frequencies its performance is not stable. This might be the graphene flakes folding in PVP powder which minimize its exposed area at high voltages.

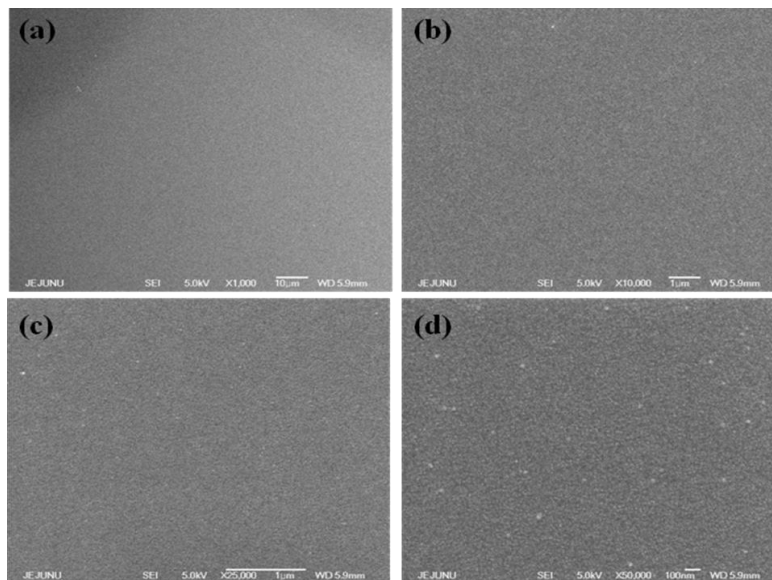


Figure 4-46 (a-d low to high magnification) shows the FE-SEM images of graphene/PVP composite thin film.

In figure 4-47 (a & b) surface profile (2D and X-direction) of graphene/ZnO are given, respectively. It shows that the roughness of film is 7.43 nm, while variations in film profile in the x-direction are mostly around 7 nm on average. In figure 4-47 (c), 3D profile of

graphene/ZnO film is shown. It can be elucidated that PVP and graphene flakes deposited through EHDA technique are distributed and oriented randomly on the substrate.

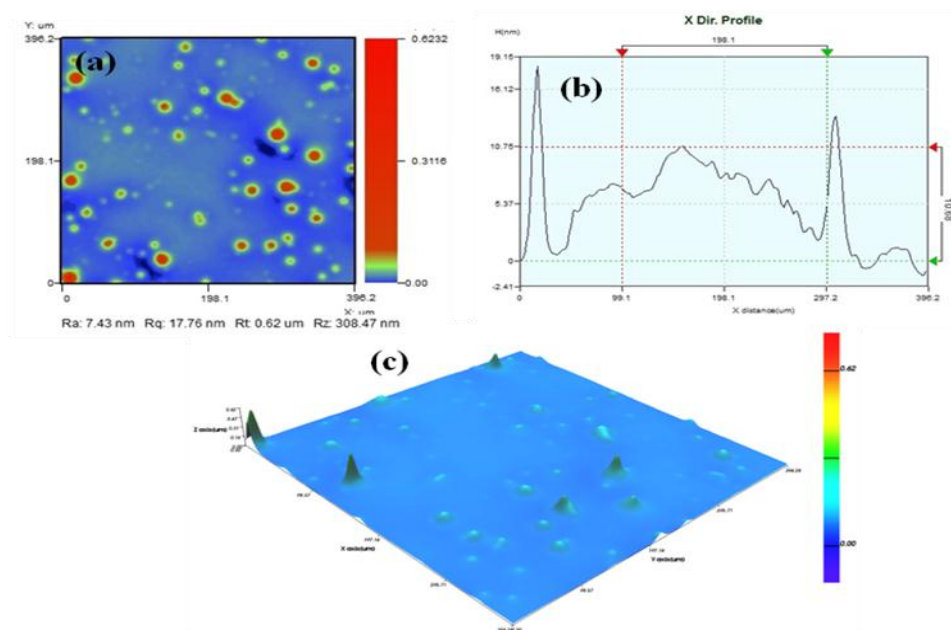


Figure 4-47 3D-Nano Mapping of Graphene/PVP composite film.

Figure 4-48 shows the transmittance spectrum of graphene/PVP composite thin film in the ultraviolet (UV), visible, and near-infrared (NIR) spectral ranges. The transmittance of the thin film was observed to be in the range of 85~ 88% in the visible range. Absorption appears below 298 nm in the UV range. The transmittance spectrum reveals that the dielectric graphene/PVP composite thin film is more suitable for optoelectronic device applications due to its good transmittance. Based on the data, we calculated the energy bandgap ( $E_g$ ), which was found to be 3.35 eV.

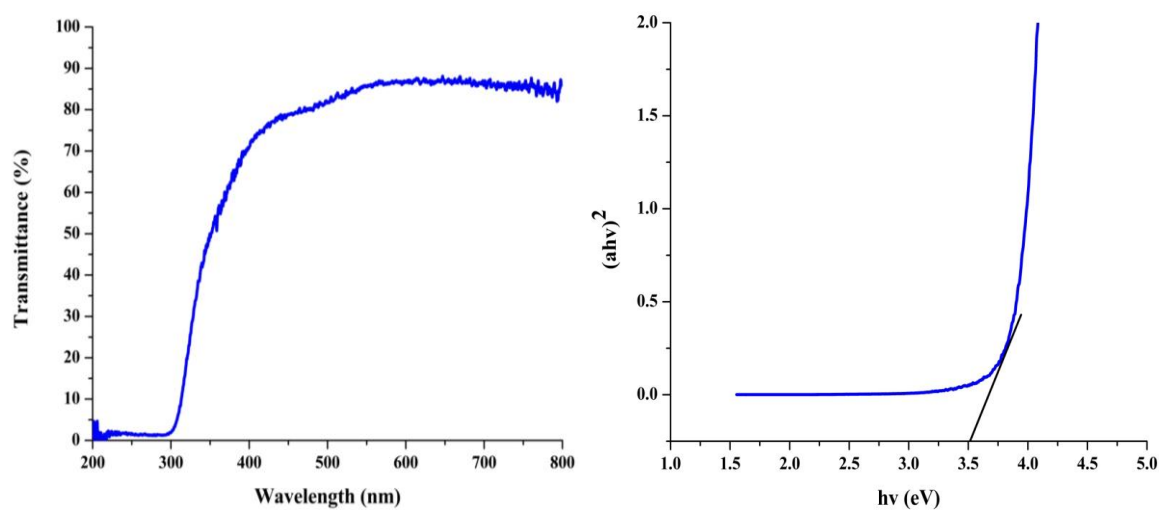


Figure 4-48 (a) Transmittance spectra of graphene/PVP film (b)  $(ahv)^2$  vs.  $hv$  plot for bandgap estimation of graphene/PVP film.

A similar approach mentioned in section 4.2 for graphene/ZnO composite thin film fabrication is used for graphene/PVP composite thin film. Graphene/PVP composite film is then employed as dielectric layer while using ITO and PEDOT:PSS bottom and top electrode respectively.

In order to investigate the charge storage mechanism of the fabricated device, capacitance–voltage (C–V) curve is plotted for the device with different ac frequency. Figure 4-49(a-b-c) shows the C–V analysis for thin films for PVP, graphene/PVP (blended approach) and graphene/PVP (LBL approach) as dielectric layers with input frequency of about 1 kHz, respectively. It has been observed that graphene/PVP composite thin film shows better capacitive behavior with maximum capacitance  $1.22 \times 10^{-5} \text{ F/cm}^2$  in the voltage range to 0.1 to 1.80 V.

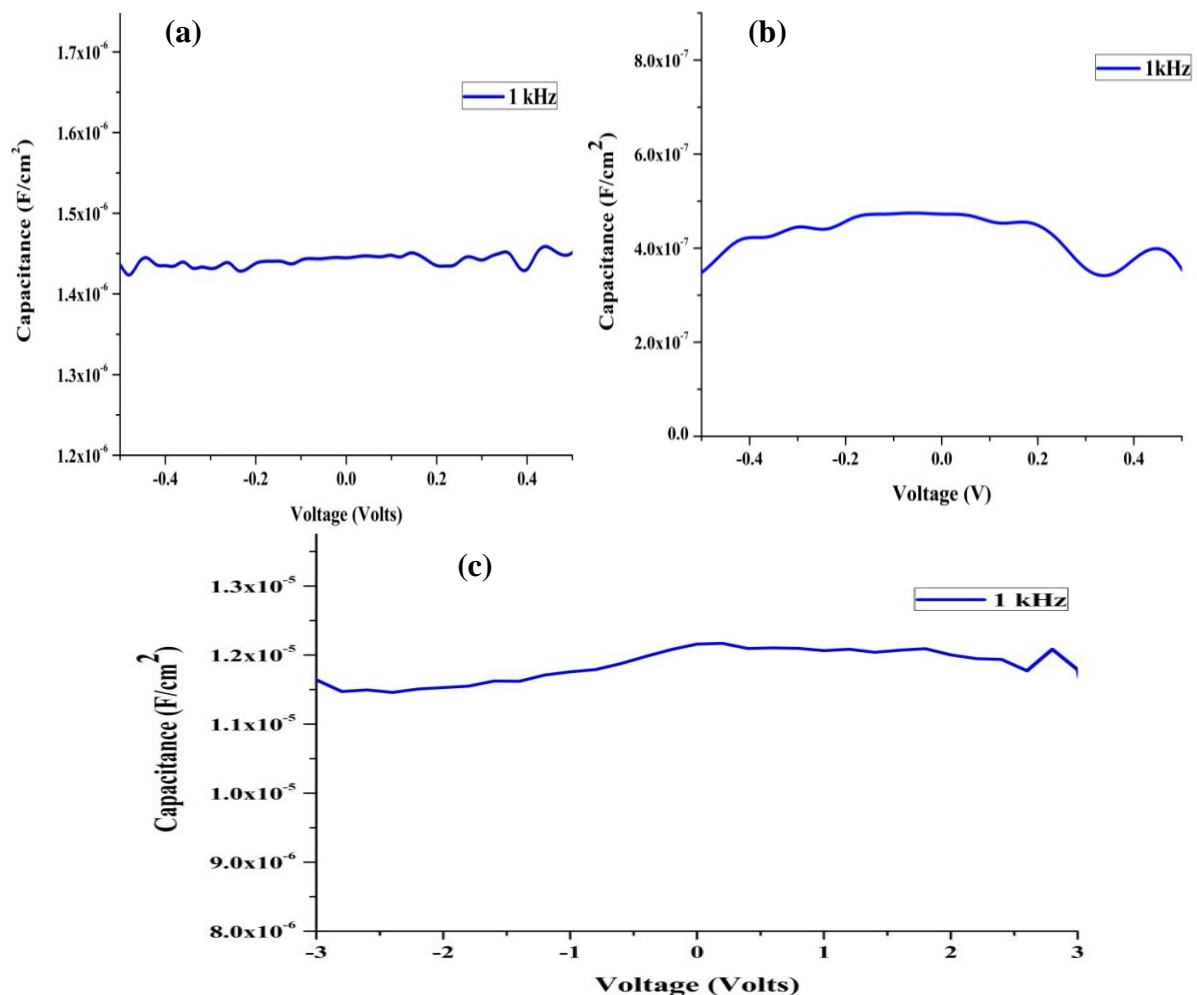


Figure 4-49 Capacitance–voltage analysis of capacitor at 1 kHz when dielectric thin film is (a) PVP, (b) Graphene/PVP (Blended Approach) and (c) Graphene/PVP (LBL approach), respectively. Whereas, the capacitance of the device with different frequency shown in figure 4-50(a-b-c). It revealed that the capacitance of the device has been decreased with increase the *ac*

frequency for each dielectric thin film. Figure 4-50(b) shows that the performance of blended fabricated graphene/PVP composite thin film is the worst as compared to PVP and graphene/PVP (LBL) dielectric thin film at higher frequencies. Figure 4-50(c) shows that that graphene/PVP dielectric thin film based capacitor has given the most stable C-V behavior even at higher frequencies like up to 100 kHz and high voltages as compared to PVP and graphene/PVP (blended approach) dielectric thin films. The characteristics confirm that the as fabricated multi-layer printed device shows good charge storage mechanism for graphene/PVP composite thin film fabricated by layer -by-layer approach.

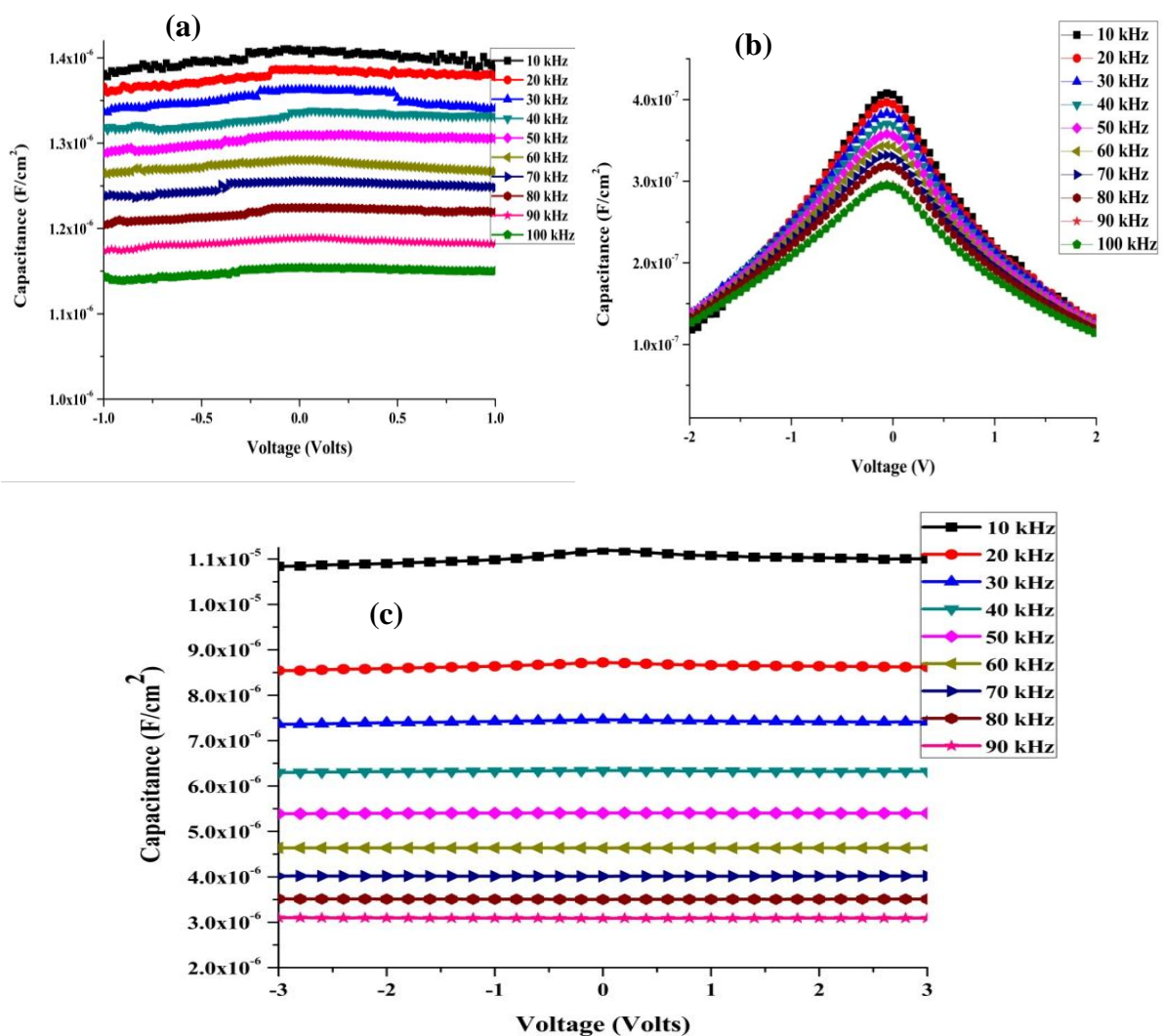


Figure 4-50 Capacitance–voltage analysis of capacitor at higher frequencies when dielectric thin film is (a) PVP, (b) Graphene/PVP (Blended Approach) and (c) Graphene/PVP (LBL approach), respectively.

## 5. Conclusions and Future Outlook

### 5.1 Conclusions

In this work mainly graphene flakes thin film, graphene/ZnO and graphene/PVP composite thin films are studied. Graphene flakes dispersion synthesis, its processing using EHDA technique and then its employment in diode device is taken on. Then graphene flakes are blended with ZnO and PVP for composite thin film fabrication. Then these composite thin films are employed in diode and capacitor, directly without using any cumbersome transferring mechanism.

Firstly, the graphene flakes were synthesized by exfoliation and dispersed in aqueous solutions by the assistance of bath sonication and ultrasonication. This aqueous graphene dispersion was found to be stable even after 2 months. A simple diode device was fabricated to and graphene flakes film was deposited as cathode electrode by using EHDA technique. Almost 100 times current density increased was observed when voltage was increased from 0.3V to 4V in diode device.

Secondly, composite thin films were fabricated using graphene flakes in combination with ZnO nano-particles and PVP polymer, respectively. Graphene flakes and ZnO were combined in different ways like layer-by-layer, blended and semi-blended approaches. Each time graphene/ZnO composite film was employed as cathode electrode to diode device. For layer-by-layer approach, 200 times current density increased was observed. While, 110 times current density increased was observed for blended approach of graphene/ZnO composite thin film and 50 times current density increased for semi-blended approach was noticed.

Graphene/PVP composite thin film was employed as dielectric layer in capacitor. It was observed that at 1 KHz the capacitance capability was much better than simply PVP dielectric thin film. Also, it was observed at high frequencies that graphene/PVP composite thin film stabilized the capacitor performance as compared to PVP dielectric thin film based capacitor.

## 5.2 Future Outlook

With the entire modern and well acceptable boom in graphene research, many important issues are still to be determined before bringing out the all-graphene electronics into the market. In our work, I think there is enough room for further research and improvement. As in our case the graphene flakes concentration is not very high because of the re-bundling of graphene flakes. So by finding new ways graphene flakes concentration can be increased and process can be more speeded-up. Regarding, graphene based composite thin films; it can be tried with other materials to find best combinations for better performance of electronic devices.

2-Dimensional (2D) atomic crystals are stable materials, which carry many properties which cannot be found in their 3D counterparts. This class of materials has started with graphene - a monolayer of carbon atoms arranged into a hexagonal lattice. Recently, new 2D materials are synthesized like graphane, h-BN, NbSe<sub>2</sub>, MoS<sub>2</sub> etc. These materials can be investigated for best utilizations and mutual combinations of these materials can open up a new door for researchers, with unique electronic, chemical, optical and mechanical properties. Many of these various materials are structurally similar, but have very different electronic properties, ranging from semiconducting to metallic depending on their exact composition and thickness.

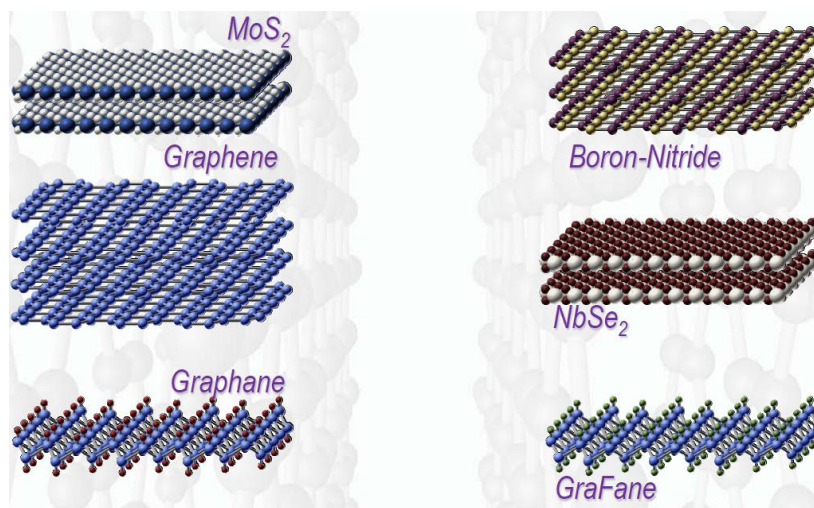


Figure 5-1 2D Crystals Based Heterostructures.

## References

- A. A. K. Geim. The rise of graphene. *Nature materials*, 183-191 6 (2007).
- A. C. Ferrari , J. C. Meyer , V. Scardaci , C. Casiraghi , M. Lazzeri , F. Mauri , S. Piscanec , D. Jiang , K. S. Novoselov , S. Roth , A. K. Geim , *Phys. Rev. Lett.* 187401 97 (2006)
- A. C. Ferrari , *Solid State Commun.* 143 47 (2007).
- A. Chavez-Valdez, M. S. P. Shaffer and A. R. Boccaccini: *J. Phys. Chem. B* 1502 117 (2013).
- A. Deshpande , W. Bao , F. Miao , C. N. Lau , B. J. LeRoy , *Phys. Rev. B* 205411 79 (2009).
- A. Fasolino , J. H. Los , M. I. Katsnelson , *Nat. Mater.* 6858 (2007).
- A. Hashimoto , K. Suenaga , A. Gloter , K. Urita , S. Iijima , *Nature* 870 430 (2004).
- A. Jaworek, A. Krupa, A. T. Sobczyk, M. Lackowski, T. Czech, S. Ramakrishna, S. Sundarrajan and D. Pliszka, *Solid State Phenom.* 127 140 (2008).
- A. K. Geim, *Science*, 1530 324 (2009).
- A. Khan, K. Rahman, D.S. Kim, K.H. Choi, *J. Mater. Process. Technol.* 700 212 (2011).
- A. Khan, K. Rahman, M.T. Hyun, D.S. Kim, K.H. Choi, *Appl. Phys. A, Mater. Sci. Process.* 1113 104 (2011).
- Adnan Ali, Yun Woo Lee, Kyung Hyun Choi and Jeongdai Jo, *J. Electron. Mater.*, 3512-3518 42 (2013)
- Adnan Ali, Jeongdai Jo, Young Jin Yang, Kyung Hyun Choi, *Appl. Phys. A*, DOI 10.1007/s00339-013-8136-y (2013)
- C. A. Di, D. C. Wei, G. Yu, Y. Q. Liu, Y. L. Guo, D. B. Zhu, *Adv. Mater.* 3289 20 (2008).
- C. Casiraghi , A. Hartschuh , H. Qian , S. Piscanec , C. Georgi , A. Fasoli , K. S. Novoselov , D. M. Basko , A. C. Ferrari , *Nano Lett.* 1433 9 (2009).
- C. D. Reddy , S. Rajendran , K. M. Liew , *Nanotechnology* 864 17 (2006).
- C. Gomez-Navarro , M. Burghard , K. Kern , *Nano Lett.* 82045 (2008).
- C. H. Chen and J. Schoonman, *J. Ind. Eng. Chem.* 1114 10 (2004).
- C. H. Yu , L. Shi , Z. Yao , D. Y. Li , A. Majumdar , *Nano Lett.* 51842 (2005).
- C. Lee, X. Wei, J. W. Kysar, and J. Hone, *Science*, 385-388 321 (2008).
- C. M. Weber, D. M. Eisele, J. P. Rabe, Y. Liang, X. Feng, L. Zhi, K. Muellen, J. L. Lyon, R. Williams, D. A. V. Bout, K. J. Stevenson, *Small.* 184 6 (2010).
- C. O. Girit , J. C. Meyer , R. Erni , M. D. Rossell , C. Kisielowski , L. Yang , C. H. Park , M.



- F. Crommie , M. L. Cohen , S. G. Louie , A. Zettl , Science 1705 323 (2009).
- C. Toke , J. K. Jain , Phys. Rev. B 45440 752 (2007).
- C.Y. Lu, S.J. Chang, S.P. Chang, C.T. Lee, C.F. Kuo, H.M. Chang, H.Z. Chiou, C.L. Hsu, I.C. Chen Appl. Phys. Lett. 153101-153103 89 (2006).
- Choe, M., Lee, B. H., Jo, G., Park, J., Park, W., Lee, S., Hong, W.-K., Seong, M.-J., Kahng, Y. H., Lee, K., and Lee, T. Organic Electronics 1864–1869 11 (2010).
- Christian Schonemberger. Bandstructure of Graphene and Carbon Nanotubes: An Exercise in Condensed Matter Physics.
- Cloupeau and Prunet-Foch, J. Aerosol Sci. 1021 24 (1994).
- Cloupeau and Prunet-Foch, J. Electrostatics. 135 22 (1989).
- D. Graf, F. Molitor, K. Ensslin, C. Stampfer, A. Jungen, C. Hierold, L. Wirtz, Nano Letters 238–242 7 (2007).
- D. I. Son, T. W. Kim, J. H. Shim, J. H. Jung, D. U. Lee, J. M. Lee, W. Il Park, W. K. Choi, Nano Lett., 2441 10 (2010).
- D. L. Miller , K. D. Kubista , G. M. Rutter , M. Ruan , W. A. de Heer , P. N. First , J. A. Stroscio , Science 324 924 (2009).
- D. L. Nika , E. P. Pokatilov , A. S. Askerov , A. A. Balandin , Phys. Rev. B 155413 79 (2009).
- E. Stolyarova , K. T. Rim , S. M. Ryu , J. Maultzsch , P. Kim , L. E. Brus , T. F. Heinz , M. S. Hybertsen , G. W. Flynn , Proc. Nat. Acad. Sci. USA 9209 104 (2007).
- Eda, G., Lin, Y.-Y., Miller, S., Chen, C.-W., Su, W.-F., and Chhowalla, M.. Applied Physics Letters 233305 92 (2008).
- F. Lu, W. Cai, Y. Zhang Adv. Funct. Mater. 1047-1056 18 (2008).
- F. Rana , P. A. George , J. H. Strait , J. Dawlaty , S. Shivaraman , M. Chandrashekar , M. G. Spencer , Phys. Rev. B 115447 79 (2009).
- F. Wang , Y. B. Zhang , C. S. Tian , C. Girit , A. Zettl , M. Crommie , Y. R. Shen , Science 320 206 (2008).
- F. Xia , T. Mueller , Y.-m. Lin , A. Valdes-Garcia , P. Avouris , Nat. Nanotechnol. 839 4 (2009).
- Ferrari, A. C., Meyer, J. C., Scardaci, V., Casiraghi, C., Lazzeri, M., Mauri, F., Piscanec, S., Jiang, D., Novoselov, K. S., Roth, S., and Geim, A. K. Physical Review Letters 187401 97 (2006).
- G. J. Exarhos, A. Rose and C. F. Windisch: Thin Solid Films 308–309 56 (1997).

- G. T. Carlson and B. L. Illman, *Am. J. Phys.* 1122 70 (2002).
- G. Van Lier , C. Van Alsenoy , V. Van Doren , P. Geerlings , *Chem. Phys. Lett.* 181 326 (2000).
- G. Wang et al. *Carbon* 3242-3246 47 (2009)
- G.C. Yi, C. Wang, W.I. Park *Semicond. Sci. Technol.* S22-S34 20 (2005).
- Gomez De Arco, L., Zhang, Y., Schlenker, C. W., Ryu, K., Thompson, M. E., and Zhou, C. *ACS Nano* 2865–2873 4 (2010).
- H. Chen , M. B. Muller , K. J. Gilmore , G. G. Wallace , D. Li , *Adv. Mater.* 3557 20 (2008).
- Hass, J., Varchon, F., Millan-Otoya, J. E., Sprinkle, M., Sharma, N., de Heer, W. A., Berger, C., First, P. N., Magaud, L., and Conrad, E. H.. *Physical Review Letters* 125504 100 (2008).
- I. Calizo, A.A. Balandin, W. Bao, F. Miao, C.N. Lau, *Nano Letters* 2645–2649 7 (2007).
- I. W. Frank , D. M. Tanenbaum , A. M. Van Der Zande , P. L. McEuen , *J. Vac. Sci. Technol. B* 2558 25 (2007).
- J. A. Robinson , M. Wetherington , J. L. Tedesco , P. M. Campbell , X. Weng , J. Stitt , M. A. Fanton , E. Frantz , D. Snyder , B. L. VanMil , G. G. Jernigan , R. L. Myers-Ward , C. R. Eddy , D. K. Gaskill , *Nano Lett.* 2873 9 (2009).
- J. C. Meyer , A. K. Geim , M. I. Katsnelson , K. S. Novoselov , T. J. Booth , S. Roth , *Nature* 446 60 (2007).
- J. C. Meyer , C. Kisielowski , R. Erni , M. D. Rossell , M. F. Crommie , A. Zettl , *Nano Lett.* 3582 8 (2008).
- J. C. Meyer , C. O. Girit , M. F. Crommie , A. Zettl , *Nature* 319 454 (2008).
- J. Liu, H. Bai, Y. Wang, Z. Liu, X. Zhang, D.D. Sun, *Adv. Funct. Mater.* 4175-4181 20 (2010).
- J. M. Calleja and M. Cardona, *Phys Rev B* 3753 16 (1977).
- J. Rohrl , M. Hundhausen , K. V. Emtsev , T. Seyller , R. Graupner , L. Ley , *Appl. Phys. Lett.* 201918 92 (2008).
- J. Wang et al. / *Journal of Solid State Chemistry* 1421–1427 184 (2011)
- J. Wang, Z. Li, G. Fan, H. Pan, Z. Chen, and D. Zhang, *Scripta Materialia*, 594-597 66 (2012).
- J. Xu, J. Han, Y. Zhang, Ya. Sun, B. Xie *Sens. Actuators, B: Chem.* 334-339 132 (2008).
- J. Yan , Y. B. Zhang , P. Kim , A. Pinczuk , *Phys. Rev. Lett.* 166802 98 (2007).
- J.H. Na, M. Kitamura, M. Arita, Y. Arakawa *Appl. Phys. Lett.* 253303- 253305 95 (2009)
- J. Tauc (Ed.), *Amorphous and Liquid Semiconductors*, Plenum, New York, 173 (1974).

- Jaworek and Krupa, *J. Aerosol Sci.* 873 30 (1999).
- Jaworek and Krupa, *Trans. Inst. Fluid Flow Mach.* 155 94 (1992).
- Ju H, Choi S, Huh SHJ. *Korean Phys. Soc.* 1649–1652 57 (2010).
- K. F. Mak , M. Y. Sfeir , Y. Wu , C. H. Lui , J. A. Misewich , T. F. Heinz , *Phys. Rev. Lett.* 196405 101 (2008).
- K. H. Choi, Adnan Ali, A. Rahman, N. Malik Mohammad, K. Rahman, A. Khan, S. Khan and D. Kim: *J Micromech Microeng.* 075033 20 (2010).
- K. H. Choi, M. Mustafa, K. Rahman, B. K. Jeong and Y. H. Doh, *Appl. Phys. A* 165 106 (2012).
- K. I. Bolotin , F. Ghahari , M. D. Shulman , H. L. Stormer , P. Kim , *Nature* 196 462 (2009).
- K. McGuire, Z. W. Pan, Z. L. Wang, D. Milkie, J. Mene´ndez and A. M. Rao: *J. Nanosci. Nanotechnol.* 2 (2002).
- K. N. Kudin , G. E. Scuseria , B. I. Yakobson , *Phys. Rev. B* 235406 64 (2001).
- K. Rahman, A. Khan, N. M. Nam, K. H. Choi and D. S. Kim, *INT J PRECIS ENG MAN journal* 663 4 (2011).
- K. Rahman, J.B. Ko, S. Khan, D.S. Kim and K.H. Choi: *J MECH SCI TECHNOL* 24 1 307 (2010).
- K. S. Novoselov, A. K. Geim, S. V. Morozov, D. Jiang, M. I. Katsnelson, I. V. Grigorieva, S. V. Dubonos, and A. A. Firsov. *Nature.* 197 438 (2005)
- K. S. Novoselov, A. K. Geim, S. V. Morozov, D. Jiang, Y. Zhang, S. V. Dubonos, I. V. Grigorieva, A. A. Firsov, *Science* 666 306 (2004).
- K. S. Subrahmanyam, S. R. C. Vivekchand, A. Govindaraj and C. N. R. Rao: *J. Mater. Chem.* 1517 18 (2008).
- K. Xu , P. Cao , J. R. Heath , *Nano Lett.* 4446 9 (2009).
- K.H. Choi, M. Mustafa, K. Rahman, B.K. Jeong, Y.H. Doh, *Appl. Phys. A* 165 106 (2012).
- K.H. Choi, S. Khan, H.W. Dang, Y.H. Doh, S.J. Hong, *Jpn. J. Appl. Phys.* 05EC08 49 (2010).
- Kang, S. J., Kocabas, C., Kim, H.-S., Cao, Q., Meitl, M. A., Khang, D.-Y., and Rogers, J. A. *Nano Letters* 3343–3348 7 (2007).
- Kim, K. S., Zhao, Y., Jang, H., Lee, S. Y., Kim, J. M., Kim, K. S., Ahn, J.-H., Kim, P., Choi, J.-Y., and Hong, B. H.. *Nature* 706–710 457 (2009).

Kotov, N. A.; Dékány, M.; Fendler, J. H. *Adv. Mater.* 637– 641 8 (1996).

Kyung Hyun Choi and Adnan Ali, *J. Korean Phys. Soc.*, 269-274 62 (2013)

Kyung Hyun Choi, Adnan Ali, Jeongdai Jo, *J Mater Sci: Mater Electron*, DOI 10.1007/s10854-013-1494-6 (2013)

L. G. De Arco, Y. Zhang, C. W. Schlenker, K. Ryu, M. E. Thompson, C. W. Zhou, *ACS Nano.* 42865 (2010).

L. Jiang, J. Zhang, D. Gamota and C. G. Takoudis, *Org. Electron.* 959 11 (2010).

L. M. Malard , M. A. Pimenta , G. Dresselhaus , M. S. Dresselhaus , *Phys. Rep.* 473 51 (2009).

Lee, C., Wei, X., Kysar, J. W., and Hone, J. *Science* 385–388 321 (2008).

Lee, Y., Bae, S., Jang, H., Jang, S., Zhu, S.-E., Sim, S. H., Song, Y. I., Hong, B. H., and Ahn, J.-H. *Nano Letters* 490–493 10 (2010).

Li, X., Cai, W., An, J., Kim, S., Nah, J., Yang, D., Piner, R., Velamakanni, A., Jung, I., Tutuc, E., Banerjee, S. K., Colombo, L., and Ruoff, R. S. *Science* 1312–1314 324 (2009).

Li, X., Zhu, Y., Cai, W., Borysiak, M., Han, B., Chen, D., Piner, R. D., Colombo, L., and Ruoff, R. S. *Nano Letters* 4359–4363 9 (2009).

Luechinger NA, Athanassiou EK, Stark WJ *Nanotechnology.* 445201–445206 19 (2008).

M. A. Pimenta, G. Dresselhaus, M. S. Dresselhaus, L. G. Cancado, A. Jorio and R. Saito: *Phys. Chem. Chem. Phys.* 1276 9 (2007).

M. I. Katsnelson , *Eur. Phys. J. B.* 157 51 (2006).

M. L. Teague , A. P. Lai , J. Velasco , C. R. Hughes , A. D. Beyer , M. W. Bockrath , C. N. Lau , N. C. Yeh , *Nano Lett.* 2542 9 ( 2009).

M. Poot , H. S. J. Van Der Zant , *Appl. Phys. Lett.* 92 (2008).

M.H. Huang, S. Mao, H. Feick, H. Yan, Y. Wu, H. Kind, E. Webber, R. Russo, P. Yang *Science.* 1897-1899 292 (2001).

Mäkelä, *Functional Materials Scientific*, Espoo, Finland (2010).

Muszynski R, Seger B, Kamat PV *J Phys Chem C.* 5263–5266 112 (2008).

N. Liu et al., *Adv. Funct. Mater.* 1518-1525 18 (2008)

N. M. Muhammad, A. M. Naeem, N. Duraisamy, D. S. Kim, K. H. Choi, *Thin Solid Films* 1751 520 (2012).

N. M. Muhammad, S. Sundharam, H. W. Dang, A. Lee, B. H. Ryu and K. H. Choi, *Curr. Appl. Phys.* S68 11 (2011).

N. M. R. Peres , F. Guinea , A. H. C. Neto , Physical Review B 125411 73 (2006).

N. M. R. Peres , J. Phy. Condens. Matter 21(2009).

N. Stander , B. Huard , D. Goldhaber-Gordon , Phys. Rev. Lett. 026807 102 (2009).

Nethravathi C, Viswanath B, Shivakumara C, Mahadevaiah N, Rajamathi M Carbon. 1773–1781 46 (2008).

Novoselov, K. S., Geim, A. K., Morozov, S. V., Jiang, D., Zhang, Y., Dubonos, S. V., Grigorieva, I. V., and Firsov, A. A. Science 666–669 306 (2004).

O. Akhavan, Carbon 11–18 49 (2011).

P. A. George , J. Strait , J. Dawlaty , S. Shivaraman , M. Chandrashekar , F. Rana , M. G. Spencer , Nano Lett. 4248 8 (2008).

P. Blake, P. D. Brimicombe, R. R. Nair, T. J. Booth, D. Jiang, F. Schedin, L. A. Ponomarenko, S. V. Morozov, H. F. Gleeson, E. W. Hill, A. K. Geim, K. S. Novoselov, Nano Lett. 1704 8 (2008).

P. Guo , H. H. Song , X. H. Chen , Electrochem. Commun. 1320 11 (2009).

P. K. Sharma, M. Kumar, and A. C. Pandey, J. Nanopart. Res. 1629 13 (2011).

P. Sudhagar, R.S. Kumar, J.H. Jung, W. Cho, R. Sathyamoorthy, J. Won, Y.S. Kang Mater. Res. Bull. 1473-1479 46 (2011).

Petit C, Badosz TJ J Phys Chem C 3800–3809 113 (2009).

Pimenta MA, Dresselhaus G, Dresselhaus MS, Cançado LG, Jorio A, Saito R: Phys Chem Chem Phys. 1276 9 (2007).

Poon, Electrohydrodynamic Printing. PhD thesis, Princeton University (2002).

R. K Gupta, R. A. Singh, Schottky diode based on composite organic semiconductors, MAT SCI SEMICON PROC. 83 7 (2004).

R. R. Nair , P. Blake , A. N. Grigorenko , K. S. Novoselov , T. J. Booth , T. Stauber , N. M. R. Peres , A. K. Geim , Science 1308 320 (2008).

R. Zhang et al. Solid State Sciences 865–869 11 (2009)

Reina, A., Jia, X., Ho, J., Nezich, D., Son, H., Bulovic, V., Dresselhaus, M. S., and Kong, J. Nano Letters, 30–35 9 (2008).

S. Bae, H. Kim, Y. Lee, X. F. Xu, J. S. Park, Y. Zheng, J. Balakrishnan, T. Lei, H. R. Kim, Y. I. Song, Y. J. Kim, K. S. Kim, B. Ozyilmaz, J. H. Ahn, B. H. Hong, S. Iijima, Nat. Nanotechnol. 574 5 (2010).

S. Baranovski, Charge Transport in Disordered Solids with Applications in Electronics (John

Wiley & sons, Chichester, West Sussex, UK, 2006).

S. Berber , Y. K. Kwon , D. Tomanek , Phys. Rev. Lett. 4613 84 (2000).

S. Lee, B. Koo, J. Shin, E. Lee, H. Park and H. Kim, Appl. Phys. Lett. 162109 88 (2006).

S. Mohseni Meybodi, S.A. Hosseini, M. Rezaee, S.K. Sadrnezhad, D. Mohammadyani Ultrason. Sonochem. 841-845 19 (2012).

S. P. Pang, H. N. Tsao, X. L. Feng, K. Mullen, Adv. Mater. 3488 21 (2009).

S. Pang, Y. Hernandez, X. Feng, and K. Müllen, Advanced Materials, 2779-2795 23 (2011).

S. Park , D. A. Dikin , S. T. Nguyen , R. S. Ruoff , J. Phys. Chem. C 15801 113 (2009).

S. Park , K. S. Lee , G. Bozoklu , W. Cai , S. T. Nguyen , R. S. Ruoff , ACS Nano 572 2 (2008).

S. Pisana , M. Lazzeri , C. Casiraghi , K. S. Novoselov , A. K. Geim , A. C. Ferrari , F. Mauri , Nat. Mater. 198 6 (2007).

S. Piscanec , M. Lazzeri , F. Mauri , A. C. Ferrari , Eur. Phys. J. Special Topics 159 148 (2007).

S. R. Samarasinghe, I. Pastoriza-Santos, M. J. Edirisinghe and L. M. Liz-Marzan, Appl. Phys. A 141 91 (2008).

S. V. Morozov , K. S. Novoselov , M. I. Katsnelson , F. Schedin , L. A. Ponomarenko , D. Jiang , A. K. Geim , Phys. Rev. Lett. 016801 97 (2006).

S.B. Park, B.G. Kim, J.Y. Kim, T.H. Jung, D.G. Lim, J.H. Park, J.G. Park Appl. Phys. A. 169-172 102 (2011).

Si Y, Samulski ET Chem Mater. 6792–6797 20 (2008).

Sun, T., Wang, Z. L., Shi, Z. J., Ran, G. Z., Xu, W. J., Wang, Z. Y., Li, Y. Z., Dai, L., and Qin, G. G. Applied Physics Letters 133301-3 96 (2009).

T. H. Kim, C. G. Han and C. K. Song, Thin Solid Films 1232 516 (2008).

T. O. Wehling, K. S. Novoselov, S. V. Morozov, E. E. Vdovin, M. I. Katsnelson, A. K. Geim, A. I. Lichtenstein, Nano Lett. 173 8 (2008).

Unarunotai, S., Koepke, J. C., Tsai, C.-L., Du, F., Chialvo, C. E., Murata, Y., Haasch, R., Petrov, I., Mason, N., Shim, M., Lyding, J., and Rogers, J. A.. ACS Nano. 5591–5598 4 (2010).

Unarunotai, S., Murata, Y., Chialvo, C. E., Kim, H.-s., MacLaren, S., Mason, N., Petrov, I., and Rogers, J. A. Applied Physics Letters 202101-3 95 (2009).

V. C. Tung, M. J. Allen, Y. Yang, R. B. Kaner, Nat. Nanotechnol. 25 4 (2009).

V. M. Apalkov , T. Chakraborty , Phys. Rev. Lett 126801 97 (2006).

V. P. Gusynin , S. G. Sharapov , J. P. Carbotte , Phys. Rev. Lett. 256802 96 (2006).

W. Bao , F. Miao , Z. Chen , H. Zhang , W. Jang , C. Dames , C. N. Lau , Nat. Nanotechnol. 562 4 (2009).

W. Liu, B. L. Jackson, J. Zhu, C. Q. Miao, C. H. Chung, Y. J. Park, K. Sun, J. Woo, Y. H. Xie, ACS Nano. 3927 4 (2010).

W. S. Hummers and R. E. Offeman, J. Am. Chem. Soc. 1339 80 (1958).

W.I. Park, G.C. Yi Adv. Mater. 87-90 16 (2004).

Wang, X., Zhi, L., and Mullen, K. Nano Letters 323–327 8 (2007).

Wang, Y., Chen, X., Zhong, Y., Zhu, F., and Loh, K. P. Applied Physics Letters 063302-3 95 (2009).

Williams G, Seger B, Kamat PV ACS Nano. 1487–1491 2 (2008).

Wu J, Shen X, Jiang L, Wang K, Chen K Appl Surf Sci. 2826–2830 256 (2010).

Wu, J., Agrawal, M., Becerril, H. A., Bao, Z., Liu, Z., Chen, Y., and Peumans, P. ACS Nano. 43–48 4 (2009).

Wu, J., Becerril, H. A., Bao, Z., Liu, Z., Chen, Y., and Peumans, P. Applied Physics Letters 263302-3 92 (2008).

X. Du , I. Skachko , F. Duerr , A. Luican , E. Y. Andrei , Nature 462 192 (2009).

X. Liu, T. H. Metcalf, J. T. Robinson, B. H. Houston, and F. Scarpa, Nano Letters. 1013-1017 12 (2012).

X. T. Jia , M. Hofmann , V. Meunier , B. G. Sumpter , J. Campos-Delgado , J. M. Romo-Herrera , H. B. Son , Y. P. Hsieh , A. Reina , J. Kong , M. Terrones , M. S. Dresselhaus , Science 1701 323 (2009).

X. Wang, L.J. Zhi, N. Tsao, J.L. Tomovic, K. Mullen, Angew. Chem., Int. Ed. 2990-2992 47 (2008).

X. Y. Ye, Y. M. Zhou, Y. Q. Sun, J. Chen, and Z. Q. Wang, J. Nanopart. Res. 1159 11 (2009).

X. Zhao, Q. Zhang, Y. Hao, Y. Li, Y. Fang, D. Chen, Macromolecules. 9411– 9416 43 (2010).

X.M. Yang, Z.Z. Gu, Z.H. Lu, Y. Wei Appl. Phys. A 115-117 59 (1994).

Y. B. Zhang , V. W. Brar , C. Girit , A. Zettl , M. F. Crommie , Nat. Phys. 722 5 (2009).

Y. Cao, Z. M. Wei, S. Liu, L. Gan, X. F. Guo, W. Xu, M. L. Steigerwald, Z. F. Liu, D. B. Zhu, Angew. Chem. Int. Ed.6319 49 (2010).

Y. Choi, H. Kim, K. Sim, K. C. Park, C. Im and S. Pyo, *Org. Electron.* 1209 10 (2009).

Y. Ito, M. Nyce, R. Plivelich, M. Klein, D. Steingart, S. Banerjee *J. Power Sources.* 2340-2345 196 (2011).

Y. M. You , Z. H. Ni , T. Yu , Z. X. Shen , *Appl. Phys. Lett.* 163112 93 (2008).

Y. P. Zhang, H. B. Li, L. K. Pan, T. Lu, and Z. Sun, *J. Electroanal. Chem.* 634, 68 (2009).

Y. Y. Wang , Z. H. Ni , T. Yu , Z. X. Shen , H. M. Wang , Y. H. Wu , W. Chen , A. T. S. Wee , *J. Phys. Chem. C* 10637 112 (2008).

Yin Z, Wu S, Zhou X, Huang X, Zhang Q, Boey F, Zhang H *Small* 307–312 6, (2010).

Z. Guo , D. Zhang , X.-G. Gong , *Appl. Phys. Lett.* 95 163103 (2009).

Z. H. Ni , W. Chen , X. F. Fan , J. L. Kuo , T. Yu , A. T. S. Wee , Z. X. Shen , *Phys. Rev. B* 115416 77 (2008).

Z. Lee , K. J. Jeon , A. Dato , R. Erni , T. J. Richardson , M. Frenklach , V. Radmilovic , *Nano Lett.* 3365 9 (2009).

Z. Ni , Y. Wang , T. Yu , Z. Shen , *Nano Research* 273 1 (2008).

Z.L. Wang, R. Yang, J. Zhou, Y. Qin, C. Xu, Y. Hu, S. Xu *Mater. Sci. Eng., R.* 320-329 70 (2010).

Zhao, X.; Zhang, Q.; Hao, Y.; Li, Y.; Fang, Y.; Chen, D. *Macromolecules.* 9411 43 (2010).

Zheng WT, Ho YM, Tian HW, Wen M, Qi JL, Li YA *J Phys Chem C.* 9164–9168 113 (2009).

Zhu Y, Elim HI, Foo YL, Yu T, Liu Y, Ji W, Lee JY, Shen Z, Wee AT, Thong JT, Sow CH *Adv Mater.* 587–592 18 (2006).